



*Università degli Studi di Firenze*

Facoltà di Ingegneria  
Dipartimento di Energetica “Sergio Stecco”

---

PHD SCHOOL: *Energetica e Tecnologie Industriali Innovative*

SCIENTIFIC AREA: ING-IND/08 - *Macchine a Fluido*

# EXPERIMENTAL ANALYSIS OF GAS TURBINE AIRFOIL LEADING EDGE COOLING SYSTEMS

**PhD Candidate:** ING. FRANCESCO MAIUOLO  
**Tutor:** PROF. ING. BRUNO FACCHINI  
**CoTutor:** DR. ING. STEFANO ZECCHI  
**PhD School Coordinator:** PROF. ING. MAURIZIO DE LUCIA

---

PHD SCHOOL CYCLE: XXV (2010-2012)



*The research leading to these results  
has received funding from the  
European Union Seventh Framework Programme  
(FP7/2007-2013) under grant agreement  
n. 233799 (ERICKA)*

*I gratefully acknowledge the consortium  
for the opportunity to participate  
in such a challenging work*



# Acknowledgements

*I wish to express my sincere appreciation to those who have contributed to this work and supported me in one way or the other during this unforgettable experience.*

*First of all, I am extremely grateful to my PhD tutor, Professor Bruno Facchini, for the opportunity to participate and learn in this research activity, for his helpfulness and deep knowledge not only in engineering (excellent culinary and tour guide during the meetings!).*

*I would also like to take this opportunity to thank Dr. Stefano Zecchi from AVIO for his valuable suggestions and the advices he gave me during these three years and for the preparation of the present work.*

*The good advice, support and friendship of Dr. Lorenzo Tarchi (the "guru" of the experimental activity) starting from my master thesis training, has been invaluable on both an academic and a personal level, for which I am extremely grateful.*

*I am indebted to my colleagues for providing a stimulating and fun environment in which to learn and grow. In particular a special mention need to be done for the experimental team at the "Laboratorio Colonne" of the University of Florence, Gianluca Caciolli (my PhD-mate and the "real" marathon runner!), Alessio Picchi (highly knowledgeable and great trail runner!), Marco Pievaroli ("Marchino", the newcomer in the lab), and the ex-colleagues Francesco Simonetti and Leonardo Bonanni that are often mentioned and reminded! From the numerical team I would like to acknowledge Alessio B., Andrea, Antonio, Cosimo, Lorenzo M., Lorenzo W., Luca A., Luca I., Mirko, Riccardo D. S. and Riccardo F.. No less important is the great Carlo "Carlino" Carcasci, with his funny moments and very useful suggestions!*

*Finally, I want to express a special thank to my family and my girlfriend Chantal for their continuous support, encouragement and in several cases patience given during this period.*

*Thanks to everyone!!!*

# Abstract

This PhD research project and the findings of its intensive experimental analysis regard various internal leading edge cooling systems designed both for aircraft engines and heavy duty gas turbines.

In the last decades, research in the area of such power systems has mainly focused on the improvement of the overall efficiency and power output, making sure the strict legislative requirements which regulate pollutant emissions (particularly  $\text{NO}_x$ ) are observed. These aspects are related to turbine inlet temperatures (TIT) which, in recent years, have reached values far above the acceptable material temperatures of the components directly exposed to hot gases. One of the most thermally loaded regions is represented by the leading edge of the turbine blades in which more complex cooling schemes are required to keep the metal temperature at levels consistent with the design life.

The present work regards an experimental survey on different scaled up leading edge cooling schemes aimed at measuring the heat transfer coefficient (HTC) inside the leading edge cavity of high pressure gas turbine blades. Several experimental models were designed in order to meet the requirements of the industrial partners, in fact a modular approach has been used to test four different *external* leading edge profiles with different *internal* impingement geometries. The complete leading edge cooling scheme has been replicated which is, in particular, composed of "cold bridge" systems with different jet arrangements (number of jets, shape, jet-to-jet pitches) and coolant extraction from the cavity, with different extraction hole arrays, in order to underline the influence of the coolant extraction on the internal heat transfer distribution. Detailed two-dimensional heat transfer coefficient

maps have been obtained by means of a transient technique, using a TLC (Thermo-chromic Liquid Crystals) thermography in a narrow band formulation. The experiments have been performed in an engine similitude in terms of impingement jet Reynolds number, which is the main driving parameter in these internal cooling systems.

The study has been carried out within the European Research Project ERICKA (Engine Representative Internal Cooling and Knowledge Applications), part of the European Union Framework Programme 7, whose overall objective is to provide a means for improving the existing turbine blade cooling technology, thus reducing the turbine blade cooling mass-flow. In this scientific framework, the University of Florence is involved in Work Package 2 which focuses on the stationary experiments in leading edge impingement cooling systems, together with its industrial partners AVIO and ALSTOM Switzerland.



# Contents

<b>Nomenclature</b>	<b>XIII</b>
<b>1 Introduction</b>	<b>1</b>
1.1 Background of Present Research . . . . .	1
1.2 ERICKA European Project . . . . .	6
1.3 Objectives of Present Research . . . . .	8
<b>2 Overview of Gas Turbine Cooling Systems</b>	<b>9</b>
2.1 Internal Gas Turbine Cooling . . . . .	10
2.1.1 Radial and Multi-pass Ducts . . . . .	10
2.1.2 Rib Turbulated Cooling . . . . .	12
2.1.3 Pin Fins . . . . .	13
2.1.4 Dimple Cooling . . . . .	14
2.1.5 Double Wall Cooling . . . . .	14
2.1.6 Impingement Cooling . . . . .	15
2.2 Leading Edge Impingement Cooling . . . . .	18
<b>3 Heat Transfer Coefficient Measurement</b>	<b>23</b>
3.1 Convective Heat Transfer between Wall and Fluid . . . . .	23
3.2 Measurement Techniques . . . . .	26
3.2.1 Heat Transfer Steady State Techniques . . . . .	27
3.2.2 Heat Transfer Transient Techniques . . . . .	31
<b>4 Experimental Apparatus and Data Post-processing</b>	<b>45</b>
4.1 Test Rig Layout . . . . .	45
4.1.1 Mesh Heater . . . . .	47

---

4.1.2	Extraction Plenum . . . . .	49
4.2	Tested Geometries . . . . .	50
4.2.1	AVIO Geometries . . . . .	51
4.2.2	ALSTOM Geometries . . . . .	54
4.3	Measuring Devices . . . . .	56
4.3.1	Mass Flow Rate Measurements . . . . .	56
4.3.2	Static Pressure Measurements . . . . .	57
4.3.3	Flow Temperature Measurement . . . . .	58
4.4	Thermo-chromic Liquid Crystals . . . . .	59
4.5	Video Acquisition . . . . .	61
4.6	Post-processing Procedure . . . . .	61
4.7	Measurement Uncertainty . . . . .	68
<b>5</b>	<b>Baseline Geometries</b>	<b>73</b>
5.1	Heat Transfer Results on AVIO Geometries . . . . .	73
5.1.1	B2 Results . . . . .	73
5.1.2	B3 Results . . . . .	79
5.1.3	C3 Results . . . . .	86
5.2	Heat Transfer Results on ALSTOM Geometries . . . . .	93
5.2.1	Effect of the LE Opening Angle . . . . .	93
5.2.2	Effect of the SH Extraction . . . . .	101
5.2.3	Effect of the Tangential Pitch . . . . .	103
5.2.4	Effect of the Radial Pitch . . . . .	106
5.2.5	Comparisons Between the Tested Geometries . . . . .	108
<b>6</b>	<b>Optimized Geometries</b>	<b>111</b>
6.1	Heat Transfer Results on AVIO Optimized . . . . .	111
6.1.1	REF Results . . . . .	112
6.1.2	Hole Shift Results . . . . .	115
6.1.3	Fins Shift Results . . . . .	119
6.2	Heat Transfer Results on ALSTOM Optimized . . . . .	122
6.2.1	Opt7 and Opt9 Results . . . . .	123
	<b>Conclusions</b>	<b>131</b>

<i>Contents</i>	III
-----------------	-----

---

<b>Annex A</b>	<b>137</b>
<b>Bibliography</b>	<b>140</b>



# List of Figures

1.1	John Barber's patent . . . . .	1
1.2	First invented jet-engines . . . . .	2
1.3	Pressure ratio trends for commercial transport engines [1] . . .	3
1.4	Trends in turbine inlet temperature [2] . . . . .	4
1.5	Rolls-Royce Trent 1000 . . . . .	4
1.6	Gas turbine material development (source <i>www.aviogroup.com</i> )	5
1.7	Variation of TIT over recent years [3] . . . . .	6
1.8	ERICKA work breakdown overview . . . . .	7
2.1	High pressure nozzle guide vane cooling scheme [4] . . . . .	10
2.2	Radial and multi-pass cooling channels [4] . . . . .	11
2.3	Section of a cooled blade . . . . .	11
2.4	Rib effects on mainstream flow and secondary flow behaviour [5] . . . . .	12
2.5	Cross-sectional view of a modern internally cooled turbine blade	13
2.6	A typical test model for dimple cooling studies with a concep- tual view of dimple induced secondary flow [6] . . . . .	14
2.7	A sectional view of a turbine blade with double wall cooling [7]	15
2.8	Schematic diagram of flow regions in an impingement jet [8] .	16
2.9	Test section of Bunker's studies [9] . . . . .	19
2.10	Test section of Taslim's studies [10] . . . . .	20
2.11	Test section and some results of Wright's studies [11, 12, 13] .	21
3.1	Approaches for heat transfer measurements . . . . .	27
3.2	Diagram of heated element technique . . . . .	28

3.3	Cooling passages model using heated copper elements for heat transfer investigations [14, 15, 16] . . . . .	29
3.4	Diagram of the heating foil technique . . . . .	30
3.5	Thin foil technique with TLC for heat transfer measurements of an ACC system [17] . . . . .	31
3.6	Diagram for lumped capacitance method to determine the averaged heat transfer coefficient on a rib . . . . .	34
3.7	Transient conduction problem for curved walls of finite wall thickness . . . . .	38
3.8	Effect of wall thickness . . . . .	39
3.9	Effect of surface curvature . . . . .	40
3.10	Finite-difference formulation of transient conduction problems	42
3.11	Diagram of the explicit finite difference formulation of the convection condition at the left boundary of the solid . . . . .	44
4.1	Test rig layout . . . . .	46
4.2	Picture of the mesh heater . . . . .	47
4.3	Main flow temperature variation ( $\dot{m} = 0.170$ kg/s) . . . . .	48
4.4	AVIO plenum characterization . . . . .	49
4.5	ALSTOM plenum characterization . . . . .	50
4.6	AVIO external leading edge models . . . . .	51
4.7	AVIO internal leading edge models . . . . .	53
4.8	AVIO crossflow condition schematic diagram . . . . .	53
4.9	ALSTOM leading edges . . . . .	54
4.10	ALSTOM internal impingement geometries . . . . .	55
4.11	Orifice plate mass flow measurement . . . . .	57
4.12	Scanivalve DSA pressure scanner . . . . .	58
4.13	Calibration setup . . . . .	60
4.14	Camera used for video acquisition . . . . .	61
4.15	Event time matrices of geometry AVIO B2 . . . . .	62
4.16	Fast-approach curve for finite-difference method . . . . .	64
4.17	HTC result from HTCvalue of AVIO B2 geometry . . . . .	64
4.18	HTC result from EPROM.m of ALSTOM G9 geometry . . . . .	65
4.19	Measurement post-processing procedure . . . . .	67

---

4.20	Uncertainty maps for AVIO C3 measurements . . . . .	69
5.1	Details of geometry AVIO B2 . . . . .	74
5.2	AVIO B2 $Nu/Nu_0$ contours . . . . .	75
5.3	AVIO B2 $Nu/Nu_0$ contours: detailed results . . . . .	76
5.4	AVIO B2 $Nu/Nu_0$ radial averaged values . . . . .	77
5.5	AVIO B2 $Nu/Nu_0$ tangential averaged values . . . . .	77
5.6	AVIO B2 $Nu/Nu_0$ spatially averaged values . . . . .	78
5.7	AVIO B2 holes discharge coefficient . . . . .	78
5.8	Details of geometry AVIO B3 . . . . .	80
5.9	AVIO B3 $Nu/Nu_0$ contours, lower $Re_j$ . . . . .	81
5.10	AVIO B3 $Nu/Nu_0$ contours, higher $Re_j$ . . . . .	82
5.11	AVIO B3 $Nu/Nu_0$ radial averaged values at % Cr = 40 . . . . .	83
5.12	AVIO B3 $Nu/Nu_0$ tangential averaged values at % Cr = 40 . . . . .	83
5.13	AVIO B3 $Nu/Nu_0$ averaged values: effect of % Cr . . . . .	84
5.14	AVIO B3 $Nu/Nu_0$ spatially averaged values . . . . .	84
5.15	AVIO B3 hole discharge coefficient . . . . .	85
5.16	Details of geometry AVIO C3 . . . . .	86
5.17	AVIO C3 $Nu/Nu_0$ contours, lower $Re_j$ . . . . .	87
5.18	AVIO C3 $Nu/Nu_0$ contours, higher $Re_j$ . . . . .	88
5.19	Central module, % Cr = 40: velocity streamlines . . . . .	89
5.20	Central module, % Cr = 40: coolant jet impinging zones . . . . .	90
5.21	AVIO C3 $Nu/Nu_0$ radial averaged values at % Cr = 40 . . . . .	91
5.22	AVIO C3 $Nu/Nu_0$ tangential averaged values at % Cr = 40 . . . . .	91
5.23	AVIO C3 $Nu/Nu_0$ averaged values: effect of % Cr . . . . .	92
5.24	AVIO C3 $Nu/Nu_0$ spatially averaged values . . . . .	93
5.25	Effect of the LE opening angle: <b>G1</b> vs <b>G4</b> contour plots . . . . .	94
5.26	Effect of the LE opening angle: <b>G1</b> vs <b>G4</b> radial averaged values . . . . .	95
5.27	Effect of the LE opening angle: <b>G1</b> vs <b>G4</b> tangential averaged values . . . . .	95
5.28	Effect of the LE opening angle: <b>G2</b> vs <b>G11</b> contour plots . . . . .	96
5.29	Effect of the LE opening angle: <b>G2</b> vs <b>G11</b> radial averaged values . . . . .	97

5.30	Effect of the LE opening angle: <b>G2</b> vs <b>G11</b> tangential averaged values . . . . .	98
5.31	Effect of the LE opening angle: <b>G3</b> vs <b>G12</b> contour plots . . .	99
5.32	Effect of the LE opening angle: <b>G3</b> vs <b>G12</b> radial averaged values . . . . .	100
5.33	Effect of the LE opening angle: <b>G3</b> vs <b>G12</b> tangential averaged values . . . . .	100
5.34	ALSTOM contour plots. Effect of the SH extraction . . . . .	101
5.35	Effect of the SH extraction in radial direction: <b>G5</b> vs <b>G11</b> . .	102
5.36	Effect of the SH extraction in tangential direction: <b>G5</b> vs <b>G11</b>	102
5.37	ALSTOM contour plots. Effect of the tangential pitch . . . . .	104
5.38	Effect of the tangential pitch in radial direction: <b>G6</b> vs <b>G11</b> vs <b>G7</b> vs <b>G8</b> . . . . .	105
5.39	Effect of the tangential pitch in tangential direction: <b>G6</b> vs <b>G11</b> vs <b>G7</b> vs <b>G8</b> . . . . .	105
5.40	ALSTOM contour plots. Effect of the radial pitch . . . . .	106
5.41	Effect of the radial pitch in radial direction: <b>G9</b> vs <b>G11</b> vs <b>G10</b>	107
5.42	Effect of the radial pitch in tangential direction: <b>G9</b> vs <b>G11</b> vs <b>G10</b> . . . . .	107
5.43	Comparisons between the tested geometries . . . . .	109
6.1	Geometry AVIO reference "REF" test . . . . .	112
6.2	AVIO "REF" vs C3 maps . . . . .	113
6.3	C3 vs "REF" test averaged values: radial direction . . . . .	114
6.4	C3 vs "REF" test averaged values: tangential direction . . . . .	114
6.5	AVIO optimized Holes Shift geometry . . . . .	116
6.6	AVIO FS vs HS vs C3 maps . . . . .	117
6.7	C3 vs HS averaged values: radial direction . . . . .	118
6.8	C3 vs HS averaged values: tangential direction . . . . .	118
6.9	AVIO optimized Fins Shift geometry . . . . .	119
6.10	C3 vs FS averaged values: radial direction . . . . .	120
6.11	C3 vs FS averaged values: tangential direction . . . . .	120
6.12	AVIO optimized vs C3 spatially averaged values . . . . .	121
6.13	ALSTOM optimized geometries . . . . .	123



---

6.14	ALSTOM Opt7 contour plots . . . . .	124
6.15	ALSTOM Opt9 contour plots . . . . .	125
6.16	ALSTOM Opt9 detailed view . . . . .	126
6.17	Averaged Nusselt number for Opt7 and Opt9: radial direction	127
6.18	Averaged Nusselt number for Opt7 and Opt9: tangential di- rection . . . . .	127
6.19	Spatially averaged Nusselt number for Opt7, Opt9 and G8 . .	128



# List of Tables

- 4.1 AVIO tested geometries . . . . . 52
- 4.2 ALSTOM tested geometries . . . . . 56
- 6.1 ALSTOM Opt main characteristics . . . . . 124



# Nomenclature

## Letters

$A$	Jet cross-section area	$[mm^2]$
$Bi$	Biot number	$[-]$
$Cd$	Discharge coefficient	$[-]$
$c_p$	Flow specific heat	$W/(kgK)$
$Cr$	Crossflow conditions	$[-]$
$d$	Impingement jet hydraulic diameter	$[mm]$
$D$	Leading edge curvature	$[mm]$
$h, HTC$	Heat transfer coefficient	$[W/(m^2K)]$
$i$	Time steps in finite-difference method	$[-]$
$I$	Electrical current	$[A]$
$k$	Thermal conductivity	$[W/(mK)]$
$l$	Hole length	$[mm]$
$L$	Reference length	$[mm]$
$\dot{m}$	Mass flow rate	$[kg/s]$
$Ma$	Mach number	$[-]$
$n$	Number of impingement jets	$[-]$
$Nu$	Nusselt number	$[-]$
$p$	Pressure	$[Pa]$
$P$	Wetted perimeter	$[mm]$
$\dot{q}$	Area Specific Heat flux	$[W/mm^2]$
$\dot{Q}$	Heat flux	$[W]$
$R$	Electrical resistance	$[\Omega]$
$Re$	Reynolds number	$[-]$

---

$s$	Impingement plate thickness	[ $mm$ ]
$S_x$	Tangential pitch	[ $mm$ ]
$S_y$	Stream-wise pitch	[ $mm$ ]
$t$	Time	[ $s$ ]
$T$	Temperature	[ $^{\circ}C, K$ ]
$v$	Velocity	[ $m/s$ ]
$V$	Volume	[ $m^3$ ]
$x$	Tangential direction	[ $mm$ ]
$y$	Stream (radial) direction	[ $mm$ ]
$z$	Vertical direction	[ $mm$ ]
$Z$	Hole-to-target spacing	[ $mm$ ]

### Greeks

$\alpha$	Thermal diffusivity	[ $m^2/s$ ]
$\beta$	Pressure ratio	[ $-$ ]
$\varepsilon$	Relative measurement error	[ $-$ ]
$\eta$	Efficiency	[ $-$ ]
$\Theta$	Dimensionless temperature	[ $-$ ]
$\vartheta$	LE opening angle	[ $deg$ ]
$\mu$	Dynamic viscosity	[ $N\ s/m^2$ ]
$\nu$	Kinematic viscosity	[ $m^2/s$ ]
$\rho$	Density	[ $kg/m^3$ ]
$\omega$	Angular velocity	[ $rad/s$ ]

### Subscripts

$avg$	Averaged values
$cr$	Crossflow in the feeding channel
$f, \infty$	Fluid
$g$	Grid
$h$	Hydraulic
$i$	Initial conditions

<i>in</i>	Inlet
<i>j</i>	Impingement jet
<i>out</i>	Out, loss
<i>pl</i>	Plenum
<i>ref</i>	Reference value
<i>s</i>	Solid
<i>st</i>	Storage
<i>w</i>	Wall

## Acronyms

<i>FC</i>	Film Cooling
<i>FS</i>	Full Scale, Fin shift
<i>HS</i>	Hole shift
<i>IR</i>	Infrared Thermography
<i>LE</i>	Leading Edge
<i>PMMA</i>	Poly-Methyl Methacrylate
<i>PS</i>	Pressure Side
<i>REF</i>	Reference test without large fins
<i>SF</i>	Scale Factor
<i>SFC</i>	Specific Fuel Consumption
<i>SH</i>	Shower-head
<i>SS</i>	Suction Side
<i>TC</i>	Thermocouple
<i>TLC</i>	Thermo-chromic Liquid Crystals
<i>TSP</i>	Temperature Sensitive Paint
<i>VR</i>	Velocity Ratio





# Chapter 1

## Introduction

### 1.1 Background of Present Research

History records over a century and a half of interest in and work on the gas turbine. The first gas turbine was patented in 1791 by the Englishman John Barber (Figure 1.1). His invention contained the basics of the modern gas turbine: it had a compressor, a combustion chamber and a turbine. John Barber's concept was sound, but given the technology of that day, it was not possible to realize this invention due to primary technological hurdles in

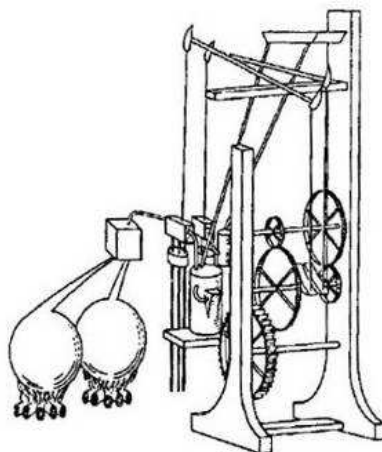


**Figure 1.1:** John Barber's patent

materials and compressor design. Despite several innovative concepts during the 19<sup>th</sup> century it was not until the early part of the 20<sup>th</sup> century that engineers were able to produce a machine that was useful. In particular, the history of the gas turbine as a viable energy conversion device began with Frank Whittle, who designed and patented the first turbo jet engine in January 1930. This engine, which had a single-stage centrifugal compressor coupled to a single-stage turbine known as "the Whittle Unit" (WU), was successfully bench tested in April 1937 (Figure 1.2(a)). The first true jet-propelled aircraft was developed, seemingly unaware of Whittle's work, by the German Hans von Ohain in 1939 (Figure 1.2(b)). In the same year the Brown Boveri company introduced the first gas-turbine-drive electrical power system in Switzerland.

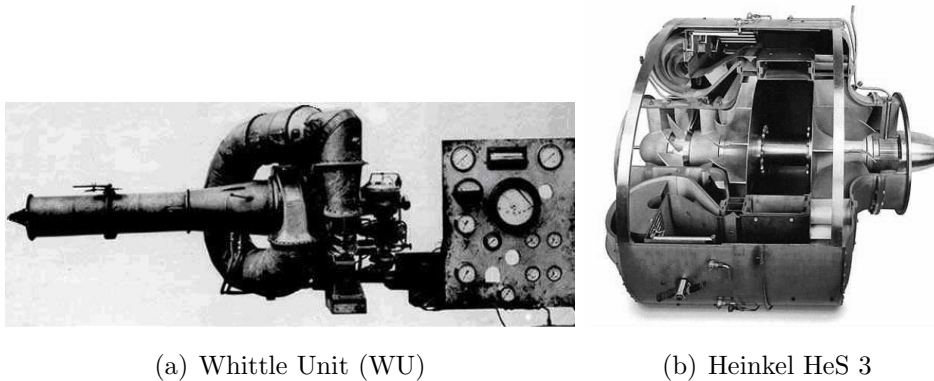


**Figure 1.2:** First invented jet-engines

Since those years, the development of this technology has improved considerably, first in the military engine field during the 1950s, and then, by the 1960s, in civilian aircrafts.

It is important to stress that this development, and the reasonable performances achieved, has been strongly influenced by the possibility, on the one hand to realize compressors with high compression ratios and high efficiency, and on the other hand, to build components capable to withstand high temperatures. Figures 1.3 and 1.4 show the turbogas technological evolution since the 1960s; both graphs illustrate the global pressure ratio and the turbine inlet temperature (TIT) increase during the last decades, which are

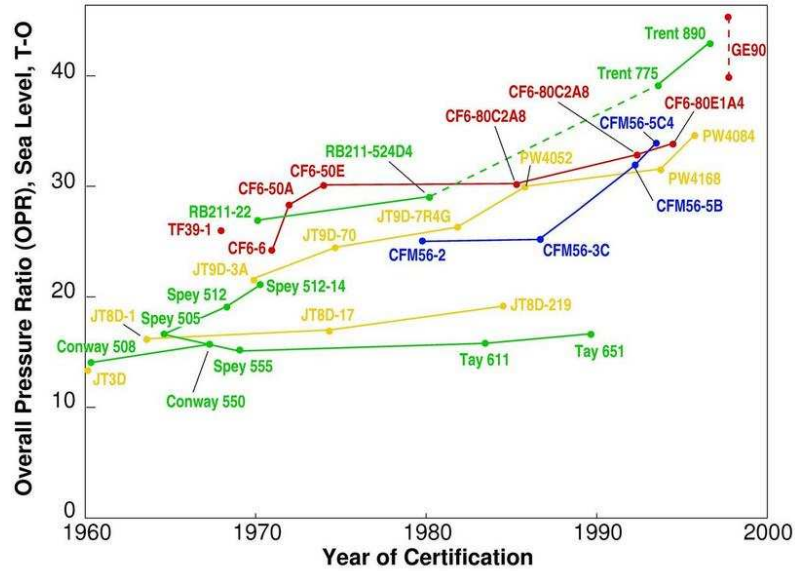


Figure 1.3: Pressure ratio trends for commercial transport engines [1]

directly related to the overall cycle efficiency and power output<sup>1</sup>. In particular, as illustrated in Figure 1.4, specific cycle power production improvement (or specific thrust) can be achieved by increasing the turbine inlet temperature. Nowadays, as predicted by the reported trend, modern gas turbine engines have reached TIT above 1800 K ( $\approx 2800$  °F), as for example the newest Rolls Royce engine Trent 1000, depicted in Figure 1.5, which powers the new commercial Boeing 787. These high temperature levels represent hostile (hot and corrosive) operating conditions for the hot-gas path components that lead to service-induced degradation and, in the worst case, to component failure. The awareness of the temperature limitations of the material has led to continuous turbine development programs for cooling technologies, material development, and related multi-disciplinary subjects such as fluid dynamics, heat transfer, aerodynamic performance, and structures, all aimed at ensuring the resistance of turbine components when exposed to hot gases. In particular the most stressed components are high pressure turbine blades,

<sup>1</sup>For more details about Joule cycle please refer to [18]

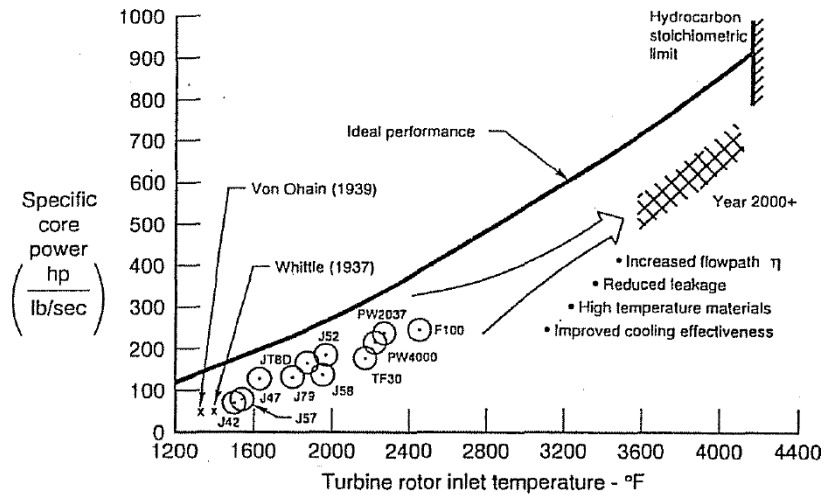
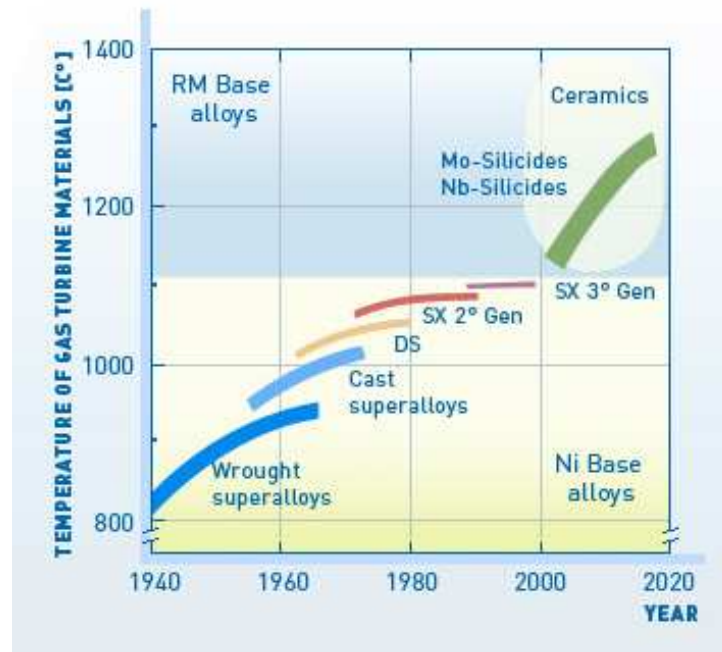


Figure 1.4: Trends in turbine inlet temperature [2]



Figure 1.5: Rolls-Royce Trent 1000

which are subjected to thermal stress as well as centrifugal forces, fatigue, creep and corrosion. Today, many modern turbine airfoils use single crystal superalloys based on nickel-cobalt (Ni-Co) compounds (Figure 1.6). Blade coatings were also developed to protect the base material from corrosion and oxidation.



**Figure 1.6:** Gas turbine material development (source [www.aviogroup.com](http://www.aviogroup.com))

In the 1960s, due to the progress made in metallurgy and manufacturing, gas turbine blade cooling systems were introduced. In the last decades great importance has been given to improving the cooling efficiency of the blade. With a complex feeding system, called Secondary Air System (SAS), the coolant flow is extracted at several axial locations in the compressors and distributed inside the most thermally loaded parts of the turbine to cool such components. Moreover, the air exercises an axial pressure balance on the rotating components and controls the axial loads on the bearings. During the last decades, blade cooling systems have been improved to reduce the blade metal temperature to acceptable levels for the materials by increasing the thermal capability of the engine. A wide range of internal and external cooling arrangements has been used in the past; however, the aim in both cases is to keep the entire blade cool enough and also to ensure that temperature gradients within the blade (which might lead to thermal stresses) are kept at an acceptable level.

Figure 1.7 illustrates well the improvement on the cooling systems in the past

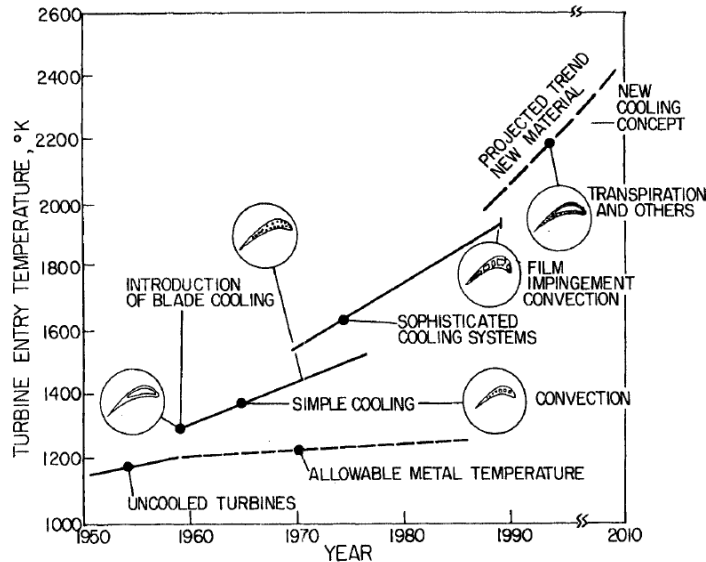


Figure 1.7: Variation of TIT over recent years [3]

50 years, from very simple configurations with radial ducts along the span of the blade to highly sophisticated configurations aimed of increasing the global cooling efficiency and reducing the required coolant mass flow rate.

Further improvements in the research field of gas turbines require higher readiness level studies that provide test cases which are more and more similar to real engine geometries and conditions, keeping the resolution and quality of the obtained results high.

Most of these studies are funded and conducted within European research programmes that are aimed at meeting the targets set by the **ACARE** (Advisory Council for Aeronautics Research in Europe) to be reached in 2020. One of the most important European projects on aero-thermal research and development is the **ERICKA** project.

## 1.2 ERICKA European Project

The ERICKA (Engine Representative Internal Cooling Knowledge and Application) project is a European Project within the Seventh Framework Programme (2007-2013), partly funded by the European Commission (GA-

2009-233799).

The main objective of the ERICKA project is the reduction of CO<sub>2</sub> emissions by 1% compared to the reference engines of the year 2000, a further improvement, in particular with regard to European Research programmes. Hence the project's target is to improve the turbine blade cooling technology.

The project is split into five technical work-packages addressing many critical aspects of internal flow and heat transfer in blades for both high pressure (HP) turbine and low pressure (LP) turbine applications. Other two specific work-packages are instead dedicated to project management and dissemination activities (Fig. 1.8).

The University of Florence (UNIFI) is involved in the work-package WP2 - "Leading edge impingement engine geometry", with experiments on a static rig focused on leading edge cooling systems, representative of current and future engines. The WP2 also includes three industrial partners: AVIO, ALSTOM Switzerland and Rolls-Royce UK. AVIO and ALSTOM provide the baseline geometries to be tested in static conditions by the University of Florence and in the rotating frame by Rolls-Royce UK. The final aim of UNIFI is to provide static experimental results to be compared with the

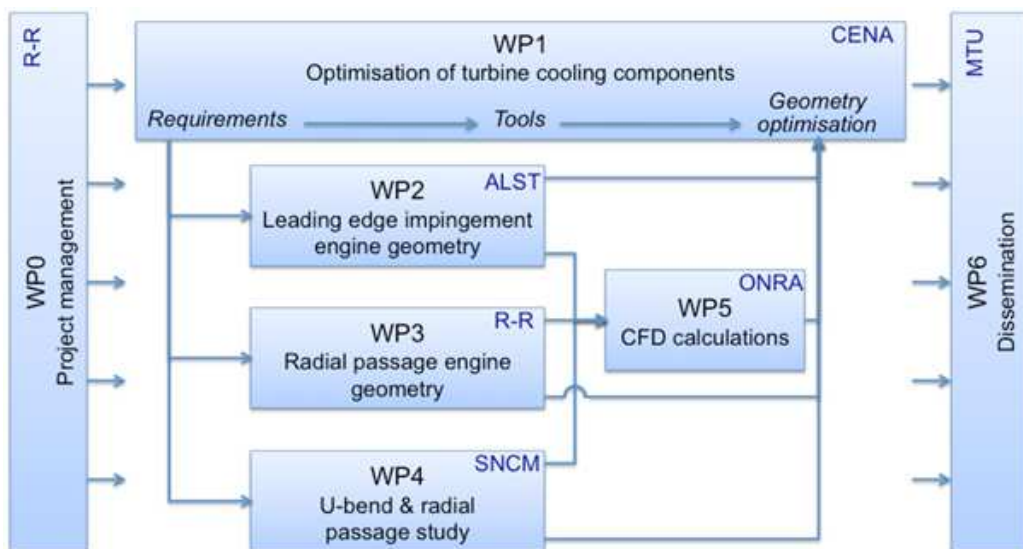


Figure 1.8: ERICKA work breakdown overview

experiments in rotating conditions on the same leading edge geometries, and a database of experimental results for the numerical simulations obtained in the other work-packages. The experiments, together with the CFD analysis, will set the guidelines for the definition of one or more optimized configurations that will be tested by UNIFI.

The whole project started in 2009 and will end in 2013.

### **1.3 Objectives of Present Research**

The main objective of this experimental work is to understand of the heat transfer characteristics inside typical airfoil leading edge cooling systems. These systems are usually based on impingement cooling by means of cold bridge systems or impingement geometries characterized by multiple arrays of small circular holes.

Starting from the definition of the test rig specifications and the geometries to investigate, this research paper will provide detailed results in terms of heat transfer distribution and its modifications due to different impingement geometries, i.e. jet shape and number, jet-to-jet distances, etc in different inlet and outlet flow arrangements to reproduce the complex fluid-dynamic interactions inside the leading edge cavity.

Results provided from the baseline geometries will set the guidelines for the definition of optimized leading edge cooling schemes, that will be tested and compared to baseline geometries.



## Chapter 2

# Overview of Gas Turbine Cooling Systems

The present work is part of the complex subject of gas turbine airfoil internal cooling systems.

Gas turbine blade cooling needs to be studied to ensure that parts of the engine, exposed to the hot main gas, do not exceed wall temperature limits to the extent that is detrimental to their life time.

High engine thermal efficiency is dependent upon high turbine entry temperature, which is limited by the turbine blade and nozzle guide vane materials. Continuous cooling of these components allows external main gas temperature higher than the material's maximum working temperature without affecting the blade and vane integrity. Generally, the fluid used as coolant flow is the air extracted from the compressor at several axial locations, that is distributed inside the most thermally loaded components of the turbine.

Several blade and vane cooling systems have been developed to maximize heat removal from the coolant flow, taking into account the geometrical, mechanical and aerodynamic constraints imposed by the stage design (Fig. 2.1). The amount of heat removed has to be considered together with the pressure losses along the cooling channels, so the design of the internal cooling system requires an accurate knowledge of the fluid-dynamic and thermal phenomena in order to promote heat exchange, keeping the pressure drops low.

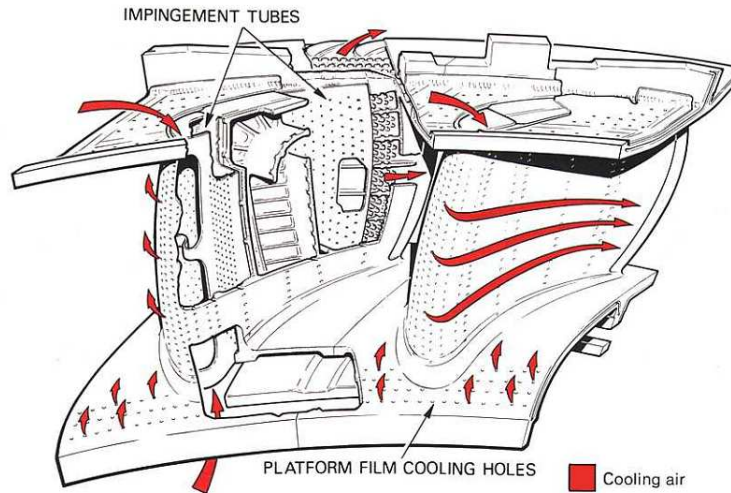


**Figure 2.1:** High pressure nozzle guide vane cooling scheme [4]

To understand the results obtained by the present research paper, it is fundamental to introduce the basics of the airfoil cooling systems starting with an overview of the internal techniques, in particular focusing on the impingement cooling and, finally, concentrating on the state of the art on the leading edge cooling systems.

## 2.1 Internal Gas Turbine Cooling

The internal cooling systems represent all the technologies where the heat exchange takes place inside the thermally loaded component, in particular in the present case, inside blades and nozzles.

### 2.1.1 Radial and Multi-pass Ducts

The main basic cooling system is represented by radial ducts. Radial ducts are a series of straight smooth channels where the coolant flow enters from the hub of the blade, and also from the tip in case of vanes, and develops along the radial direction.

Generally, as shown in Fig. 2.2, cooling channels are either single-pass

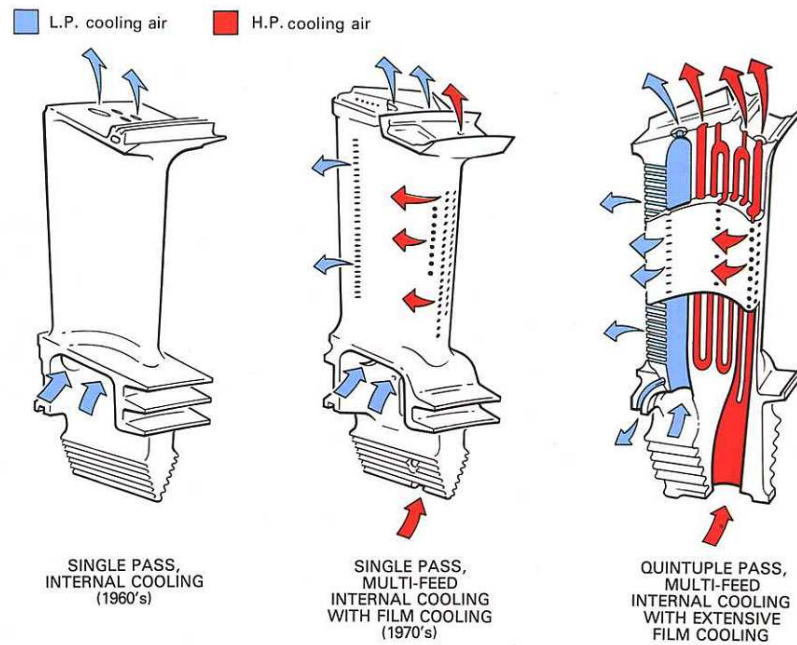


**Figure 2.2:** Radial and multi-pass cooling channels [4]

(with radial outward flow) or multi-pass (both radial outward and radial inward flow). The coolant is circulated through serpentine passages fashioned on the inside of the gas turbine blade in order to remove heat from the blade surface. Furthermore, to enhance the heat transfer coefficient inside

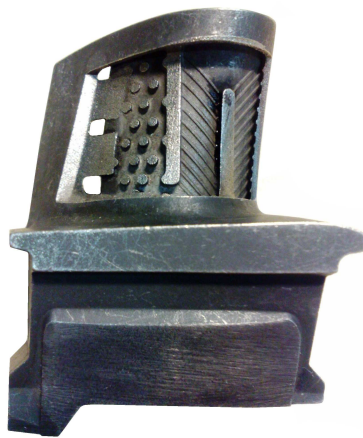


**Figure 2.3:** Section of a cooled blade

radial and multi-pass channels, these passages are roughened with rib-shaped turbulence promoters as shown in Fig. 2.3.

### 2.1.2 Rib Turbulated Cooling

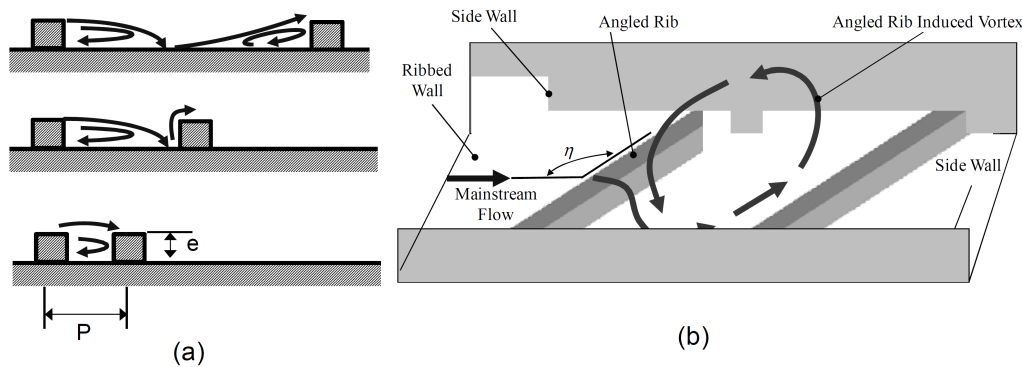


**Figure 2.4:** Rib effects on mainstream flow and secondary flow behaviour [5]

Ribs can be considered obstacles whose role is to simply trip the boundary layer, thus generating turbulences and consequently, increasing cooling effects. This is the reason why they are called "turbulence promoters". After the boundary layer is disturbed, redevelopment begins, and high heat transfer is associated with the thin boundary layer. Figure 2.4 presents conceptual views of the most notable characteristics of the effects of ribs on the mainstream flow. As shown in Fig. 2.4(a), as the mainstream flow near the surface of the channel passes over the rib, it separates from the surface. This separation results in relatively low heat transfer just downstream of the rib, due to a relatively hot cell being trapped in the area of recirculation. However, when the mainstream flow reattaches to the surface (between two ribs), this is an area of relatively high heat transfer due to the impingement of the mainstream flow on the surface. This pattern of separation, recirculation, and reattachment continues throughout the channel along with the pattern of repeating ribs.

Many geometrical parameters affect the heat transfer enhancement and consequently, the pressure losses along the ribbed channel. For more details, please refer to Han et al. [2].

### 2.1.3 Pin Fins

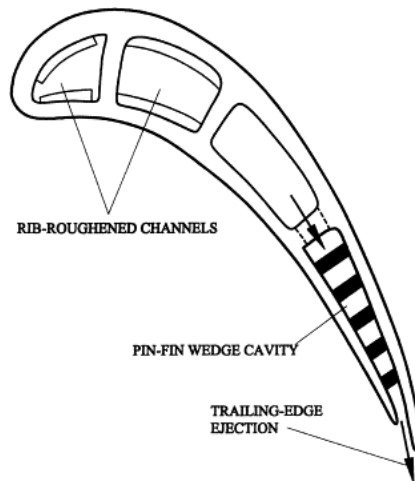


**Figure 2.5:** Cross-sectional view of a modern internally cooled turbine blade

Pin fins are prismatic support, generally with circular cross-sections, and they are one of the most common types of internal cooling devices used in turbine blades.

Pin fins are placed orthogonally to the flow direction to maximize forced convected fin cooling. Like cylinders in a cross-flow, pins shed wake at the downstream flow. The wake shed by each pin increases the free-stream turbulence, and the boundary layer development over the pin-mounted surface gets disturbed. The wakes from upstream pins also affect both the flow and heat transfer performance of downstream pins.

In addition to flow disturbances, pins conduct thermal energy away from the heat-transfer surface, and long pins can increase the effective the wet heat transfer area.

One particular application of pin fins is cooling the trailing edge of a turbine airfoil, in fact ribbed channels are not used on this part of the blade to avoid thickening of the downstream part of the airfoil. Thus, pin fins are introduced in a narrow channel from the root of the blade, as illustrated in Fig. 2.5.

### 2.1.4 Dimple Cooling

Dimpled cooling represents an alternative to rib and pin fins cooling due to the relatively low pressure loss penalty (compared with pins) and moderate heat transfer enhancement. A typical test section for dimple cooling studies is shown in Fig. 2.6.

These concavities induce flow separation and reattachment with pairs of vortices. The areas of high heat transfer include the areas of flow reattachment on the flat surface immediately downstream of the dimple. The heat transfer in the dimpled channel is typically 2 - 2.5 times greater than the heat transfer in a smooth channel with a pressure loss penalty of 2 to 4 times that of a smooth channel [6]. These values show little dependence on Reynolds number and channel aspect ratio. However, the dimple size, dimple depth, distribution, and shape each effect the heat transfer distribution in the channel.

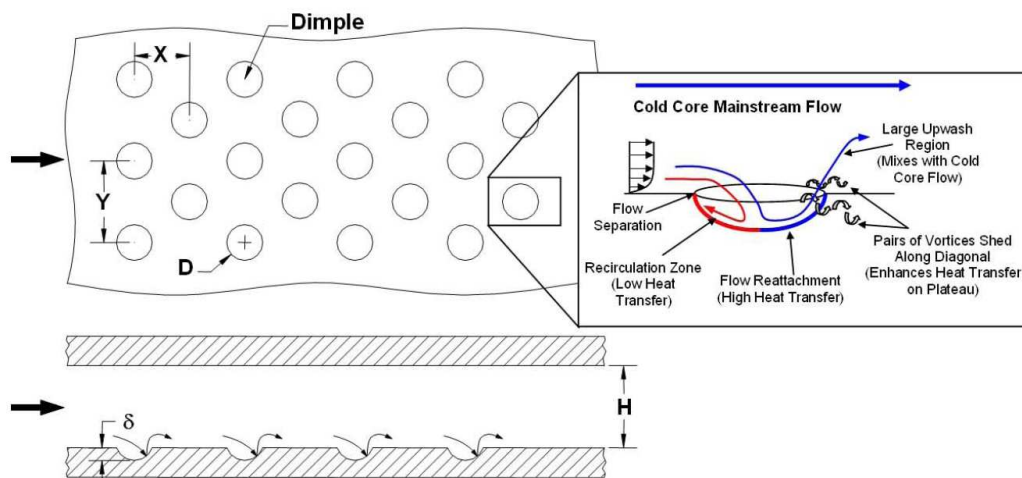


**Figure 2.6:** A typical test model for dimple cooling studies with a conceptual view of dimple induced secondary flow [6]

### 2.1.5 Double Wall Cooling

Double wall cooling uses a thin gap between two walls to enhance heat transfer from the surface of turbine blades. This technology also increases

the area exposed for heat transfer enhancement between cooling fluid and metal.

The presence of a thin gap allows to apply multiple cooling techniques within the gap, such as network of orifices connected by small passages to create impingement areas (discussed in the next section) and outward film cooling. Figure 2.7 shows an example of a patented cooled blade with double wall channels.

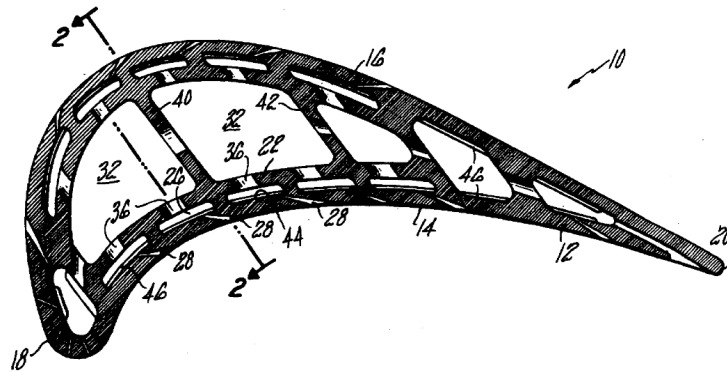


Figure 2.7: A sectional view of a turbine blade with double wall cooling [7]

### 2.1.6 Impingement Cooling

All the described internal cooling techniques are characterized by a limited heat transfer augmentation; moreover, for a long channel as in multi-pass systems, the coolant flow temperature increases along the channel leading to a reduction of the heat removed from the walls. Another internal cooling technique that guarantees considerable heat transfer enhancement is represented by the impingement cooling.

Jet impingement cooling is the application of a high velocity coolant mass flow ejected from a hole or slot and directed to the heat transfer target surface.

Since the cooling performance of impingement jets is very high, this method provides an efficient means of component heat load management where suf-

efficient pressure head and geometrical characteristics are available for implementation. Regular arrays of impingement jets are commonly used on the leading edge and midspan regions of gas turbine blades and vanes to provide relatively uniform and controlled cooling of fairly open internal surface regions. Jets are generally arranged in arrays, including in-line, staggered or arbitrary patterns.

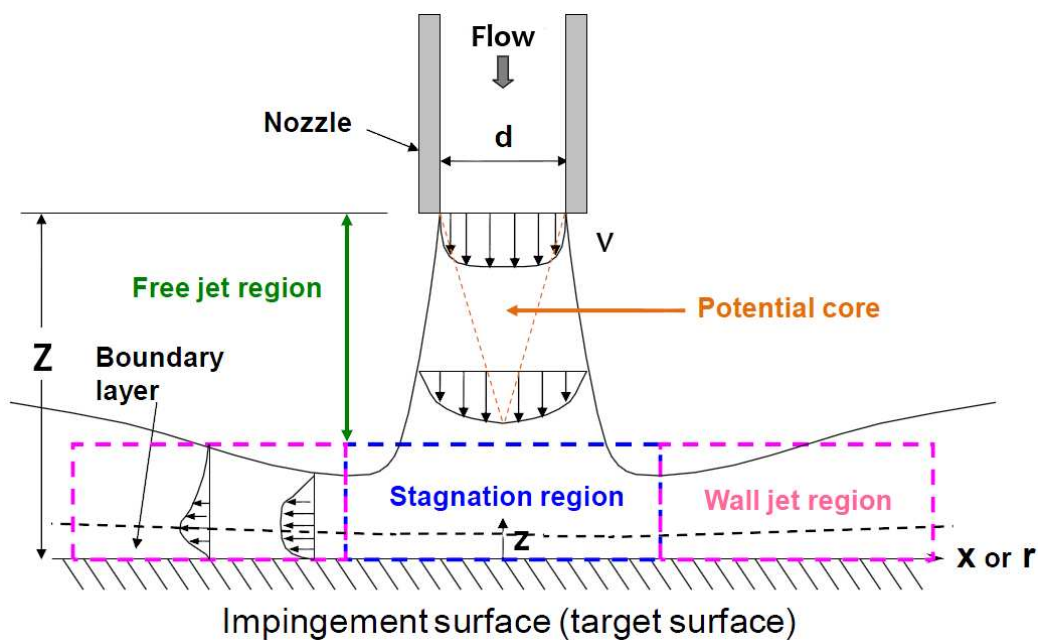


**Figure 2.8:** Schematic diagram of flow regions in an impingement jet [8]

Figure 2.8 shows a typical surface impingement caused by a jet. The flow field of an impinging jet from single round nozzles can be divided into three characteristic regions: the free jet region, stagnation flow and the wall jet regions.

In the free jet region, the jet first begins to broaden due to intensive shear interaction with the surroundings, which produces entrainment of mass, momentum, and energy. This region is called flow development region. Simultaneously, as the shear layers around the jet grow, the potential core, i. e. the region where the velocity is still equal to the bulk velocity, starts diminishing in width. The core is typically visible up to 6 - 7 jet diameters from the



nozzle. Once the free jet is fully developed (absence of core region), its axial velocity can be approximated by a Gaussian distribution.

Flow conditions of impinging flows are typically characterized by the jet Reynolds number, which is generally based on the nozzle or orifice diameter. Depending on the jet Reynolds number, four different jet characteristics can be found:

- dissipated laminar jet:  $Re_j < 3 \times 10^2$ ,
- fully laminar jet:  $3 \times 10^2 < Re_j < 1 \times 10^3$ ,
- transitional or semi-turbulent jet:  $1 \times 10^3 < Re_j < 3 \times 10^3$ ,
- fully turbulent jet:  $Re_j > 3 \times 10^3$ ,

Generally, in internal gas turbine cooling applications, only fully turbulent jets are considered.

Near the stagnation point there is the stagnation region that is strongly affected by the presence of the wall. As the jet approaches the wall, the axial velocity component is decreased and transformed into an accelerated horizontal component. The boundary layer around the stagnation point is laminar because of the favourable pressure gradient; the increase of the velocity along the wall keeps the boundary layer thin, and consequently, the heat transfer rates are high.

The wall jet region is characterized by flow directed radially outwards. The initially laminar boundary layer undergoes a turbulent transition that is induced by the impingement of large eddies created in the jet shear layer. This turbulent transition is believed to increase locally, and the heat transfer rate diminishes progressively.

The heat transfer between an impinging jet and a solid surface is affected by many different factors, such as jet exit velocity, velocity profile, nozzle or orifice geometry, inlet turbulence, entrainment conditions, separation distance between jet and target plate, or thermal wall boundary conditions [19]. For a single impinging jet, the point of maximum heat transfer is typically the stagnation point, from which heat transfer rates decrease monotonously

in radial directions. In the absence of a superimposed cross-flow, the stagnation point coincides with the geometrical center of the jets. The heat transfer coefficient in the stagnation point increases with the jet Reynolds number. On the contrary, for low jet-to-target surface distances ( $Z/d < 1$ ) or high jet Reynolds numbers, an offset between the maximum heat transfer and the center of the jet can appear.

All the reported information on the impingement jet characteristics and heat transfer result from intensive experimental and numerical studies performed since the 1960s. In particular, the first important studies were performed by Metzger et al. [20, 21], Kercher and Tabakoff [22], Martin [23], Florschuetz et al. [24, 25], Goldstein et al. [26]. They focused the attention on single and multiple jets arrangements with a flat target surface for different nozzle-to-plate distances, Reynolds numbers and temperature differences. For more details regarding impingement studies over a flat plate refer to Han et al. [2].

## 2.2 Leading Edge Impingement Cooling

The leading edge region is characterized by a complex target geometry, rather different from the classical studies considered in the open literature. Moreover, the heat transfer coefficient feature is dependent upon the interacting effects of jet impingement, film coolant extraction and convection over the portions of the surface not directly impacted by the jets.

The parameters that may affect the flow and heat transfer include impinging jet Reynolds number, jet size and distribution, leading edge sharpness, travel distance from the jet nozzles to the leading edge surface, film cooling hole distribution (number, location, angle), and distribution of the total cooling flow among the available flow paths. The possible effects of these and other parameters are compounded by their interaction. The presence of cooling extraction holes will inevitably modify the flow field in the leading edge cavity by providing new flow paths for the cooling fluid. Such flowfield modification may affect heat transfer performances either positively or negatively.

In the open literature, the first studies were performed considering the jet

impingement cooling over concave surfaces, that are comparable to a leading edge cooling scheme. In 1969, Chupp et al. [27] performed an experimental study on a single row of impingement jets on a scaled model of a leading edge. The authors correlated the heat transfer results to encompass the effects of jet-to-target surface spacing ( $Z/d$ ), jet-to-jet spacing ( $S/d$ ), and target surface curvature ( $D/d$ ) valid between jet Reynolds numbers of 3000 and 15000, thus providing a correlation for the averaged Nusselt number at the stagnation point. In the following years, Metzger et al. [28, 29] and Hrycak [30] focused on the relationship between the heat transfer coefficient and the shape of the target surface.

Very interesting contributions were provided by Metzger and Bunker [31]. They performed detailed heat transfer measurement using temperature sensitive coatings, varying impingement jet holes spacing, jet-to-target spacing, leading edge radius of curvature and jet Reynolds number. Using the same test rig (Fig. 2.9), Metzger and Bunker [9] studied the effects of film cooling mass flow extraction on the LE internal cooling. The authors found an increase of the HTC with aligned jet holes and extraction holes arrangement,

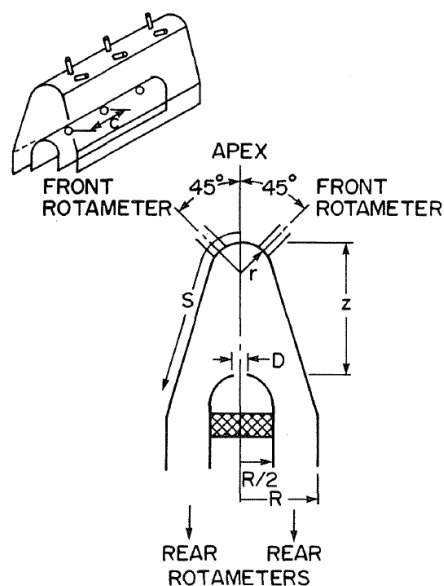


**Figure 2.9:** Test section of Bunker's studies [9]

while staggered configurations led to a decrease of the HTC. The authors also pointed out that the mass flow rate split amongst the extraction holes does not affect the HTC distribution.

In the late 90s, Lee et al. [32] performed experimental heat transfer measurements for a single impinging jet using a steady state liquid crystal technique. The dependence of impingement heat transfer on jet Reynolds number was explored for Reynolds numbers between 11000 and 50000. The authors found that for  $Re_j = 11000$  and 23000, the maximum stagnation Nusselt number was apparent at  $Z/d = 6$  with a slight reduction in the stagnation Nusselt number for smaller  $Z/d$  values. Furthermore, a heat transfer peak offset from the stagnation point was observed at  $Z/d = 2$  and  $Z/d = 4$ . A sharp transition from a laminar to turbulent boundary layer on the target surface resulted in a sudden, localized increase in heat transfer. Fenot et al. [33] explored jet impingement on a cylindrical target surface with the jet Reynolds numbers varying from 10000 to 23000. Nusselt number peaks offset from the stagnation point were observed at  $Z/d = 2$  and  $Z/d = 5$ . A decrease in the spacing between jets caused an increase in overall heat transfer.

Since 2001, Taslim et al. [10, 34] have performed a series of experimental

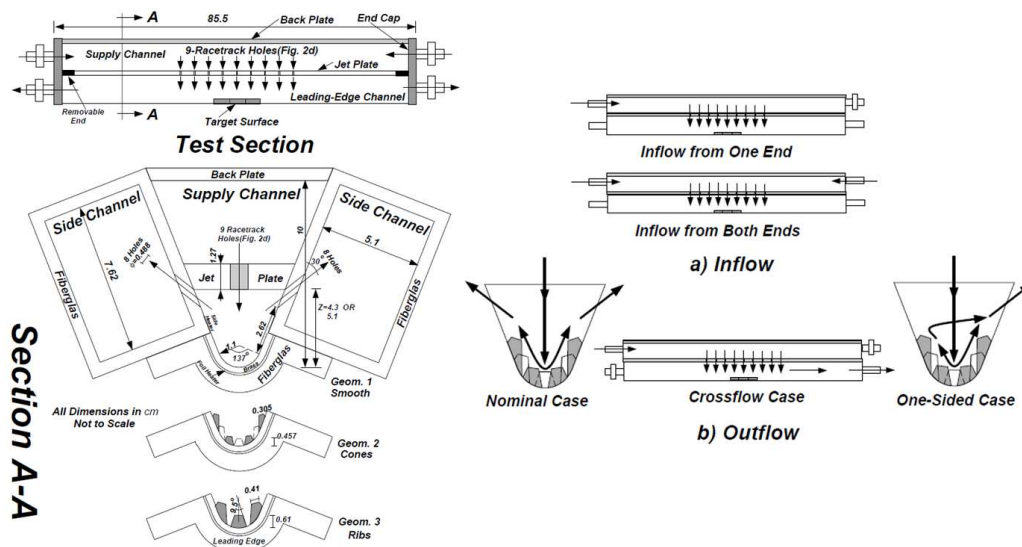


Figure 2.10: Test section of Taslim's studies [10]

and numerical analyses of a complex leading edge cooling system configuration (Fig. 2.10). The geometry is characterized both by jet impingement on a curved surface, and film cooling hole extraction. The most interesting findings are that shower-head film hole extraction and target surface roughness represent the leading parameters for the HTC enhancement with respect to inflow/outflow arrangement and jet-to-target spacing. In a more recent contribution, Taslim and Bethka [35] reported an experimental and numerical analysis of the effect of internal and external crossflow conditions on the heat flux inside a leading edge cavity. Internal crossflow means radial flow directly in the leading edge cavity, while external crossflow means radial flow in the supply channel. They found higher heat transfer coefficient values on the leading edge side walls than on the nose. They also revealed that the external crossflow leads to a reduction of the impinging jet effectiveness. In one of their latest works, Elebiary and Taslim [36] performed a numerical study, supported by experiments, on a LE geometry characterized by

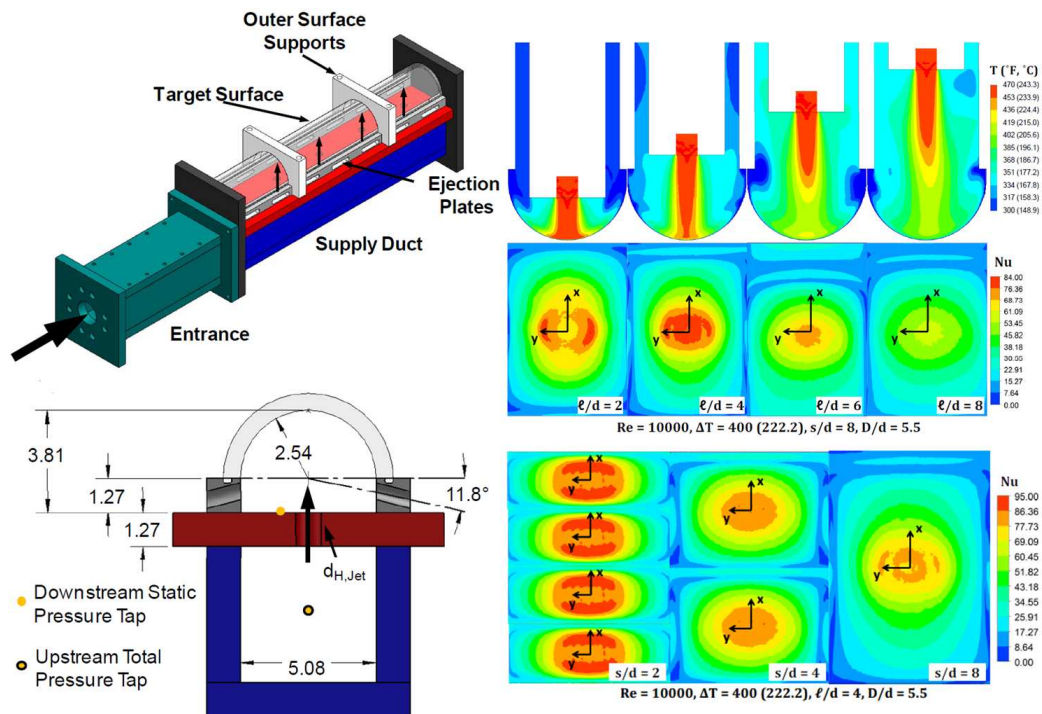


Figure 2.11: Test section and some results of Wright's studies [11, 12, 13]

racetrack (lengthened) shaped crossover holes. They found that the Nusselt number along the leading edge channel is strongly affected by the flow arrangement.

In recent years, Wright et al. [11, 12, 13] have been carrying out intensive studies on the dependence of the Nusselt number varying impingement jet geometries, jet-to-jet spacing, jet-to-target surface distance and jet temperature.

They have found higher Nusselt numbers with racetrack impingement holes and negligible effects due to jet temperature variations. Moreover, by decreasing the width of the jet-to-jet distance and reducing the distance between the jets and target surface, they have found an increase of heat transfer. For small  $Z/d_j$  and  $S_y$  values, local Nusselt number peaks were offset from the center of the jet core (Fig. 2.11).

The present work has provided an interesting contribution to the international scientific community together with three other papers published by Maiuolo et al. [37, 38, 39].

# Chapter 3

## Heat Transfer Coefficient Measurement

The final aim of this work is to measure the convective heat transfer coefficient inside scaled up models replicating typical leading edge cooling schemes. The present chapter will explain the main concepts regarding the thermal phenomena, and measurements methods to obtain local and averaged surface heat transfer coefficient distributions, in internal blade cooling applications.

### 3.1 Convective Heat Transfer between Wall and Fluid

The convective heat transfer process, which will be investigated, is defined by the so-called "Newton's Law", for which a linear relationship between the area's specific heat flux at the surface and a temperature difference between the wall and the fluid is assumed. Although the actual relationship between the heat flux and the temperature difference might be very complex, in general in heat transfer phenomena<sup>1</sup>, the considered proportionality is defined as the heat transfer coefficient ( $h$  or  $HTC$ ):

---

<sup>1</sup>for single phase forced convection

$$h := \frac{\dot{q}_w}{T_w - T_f} \quad (3.1)$$

where  $q_w$  is the area specific wall heat flux from the wall into the fluid for a cooling situation, for which  $T_w > T_f$ . Newton also observed that for a given flow and thermal situation the heat transfer coefficient can be considered time-invariant.

Equation 3.1 was used by Fourier in his transient heat conduction analysis for solid bodies. Describing the relationship between heat flux and wall normal solid temperature gradient at the surface by "Fourier's Law":

$$\dot{q}_w = -k_s \left( \frac{\partial T_s}{\partial n} \right)_w \quad (3.2)$$

where  $k_s$  is the thermal conductivity and  $T_w$  the temperature of the solid. The conduction boundary-value problem for the solid with constant thermal properties is given by:

$$\frac{\partial T_s}{\partial t} = \frac{k_s}{\rho_s c_s} \nabla^2 T_s = \alpha_s \Delta_s T_s = \alpha_s \left( \frac{\partial^2 T_s}{\partial x^2} + \frac{\partial^2 T_s}{\partial y^2} + \frac{\partial^2 T_s}{\partial z^2} \right) \quad (3.3)$$

$$T_s(x, y, z, t = 0) = T_0, \quad -k_s \left( \frac{\partial T_s}{\partial n} \right)_w = h(T_w - T_f) \quad (3.4)$$

With this, the conduction problem within the solid can be formally decoupled from the fluid convection problem and the local solid-fluid temperature field situation near the wall is incorporated in the heat transfer coefficient. The value of the heat transfer coefficient needs then to consider the complexity of the surrounding flow field, the effects of thermal boundary conditions and has to be based on an appropriate fluid reference temperature.

In case of turbulence forced convection, the heat transfer is nearly independent of the temperature boundary condition and is mainly determined by



the flow field situation. Furthermore, if the temperature differences are not too large and the thermal properties of the fluid can be considered constant, the heat transfer coefficient is independent of the actual wall and fluid temperatures [40]. This makes it a useful parameter to relate experimental data from laboratory investigations to actual engine conditions.

The temperature of solid and fluid have to be equal at the wall and the local heat flux from the solid must equal at any time the local heat flux into the fluid:

$$(T_s)_w = (T_f)_w = T_w \quad \text{and} \quad -k_s \left( \frac{\partial T_s}{\partial n} \right)_w = -k_f \left( \frac{\partial T_f}{\partial n} \right)_w \quad (3.5)$$

With equation 3.5, the heat transfer coefficient definition can be given as:

$$h = \frac{-k_f \left( \frac{\partial T_f}{\partial n} \right)_w}{T_w - T_f} \quad (3.6)$$

where  $k_f$  is the thermal conductivity of the fluid. With this consideration, the heat transfer coefficient is shown to be independent of the solid material parameters.

To transfer experimentally determined heat transfer coefficient with respect to the similarity considerations, it needs to be dimensionless represented by the Nusselt number ( $Nu$ ).

From eq. 3.6, using a geometrical scaling with a reference length  $l$ :

$$\tilde{n} = \frac{n}{l} \quad (3.7)$$

and using a dimensionless presentation for the fluid temperature field:

$$\Theta = \frac{T_f - T_w}{T_{ref} - T_w} \quad (3.8)$$

the dimensionless temperature gradient normal to the wall is given by the Nusselt number:

$$Nu = \frac{\Theta}{\partial \tilde{n} \Big|_w} = \frac{hl}{k_f} \quad (3.9)$$

For internal cooling ducts an appropriate reference length is the so-called hydraulic diameter defined as follow:

$$l = D_h = \frac{4A}{P} \quad (3.10)$$

where  $A$  is the through-flow area in each cross-section and  $P$  is the wet perimeter at this location. Of course, for complex internal cooling systems, the hydraulic diameter  $D_h(x)$  can be different at each stream-wise coordinate  $x$ . As long as full geometrical similarity is achieved between experiment and application, this local value will scale with any other geometrical length scale selected. Applying the hydraulic diameter also as reference length for the other dimensionless numbers (see Annex A), the Nusselt number for a given geometry and incompressible flows is a function of:

$$Nu = f(Re, Pr, Ro, Gr, Ec, \text{boundary conditions}) \quad (3.11)$$

## 3.2 Measurement Techniques

Many measurement techniques have been developed to obtain local heat (mass) transfer information for internal cooling applications. The different heat transfer techniques can be classified with respect to the experimental procedure, steady state or transient methods (Fig. 3.1).

All approaches require wall surface temperature measurements, generally based on thermography techniques. A short but thorough review can be found in von Wolfersdorf and Weigand [40]. They described main sensors used for internal cooling investigations (Thermocouples, TLC Thermography, Infrared Thermography, etc.), pointing out their main applications and consequent advantages and disadvantages.

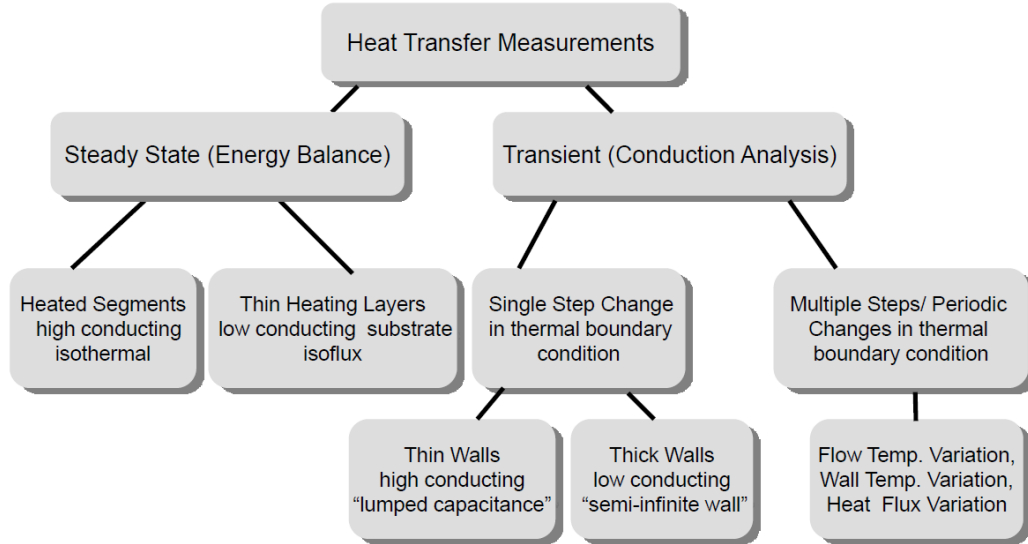


Figure 3.1: Approaches for heat transfer measurements

### 3.2.1 Heat Transfer Steady State Techniques

Measurements based on steady state techniques are generally carried out by imposing a specific heat flux from an electrical power supply. The net heat flux is calculated by estimating the heat losses due to conduction, radiation and outside wall convection. Thereby different thermal boundary conditions can be achieved, for example isothermal walls when using high conducting heated segments or nearly constant heat flux conditions when using a thin heating foil on a low conducting substrate.

#### Heated High Conducting Elements Technique

Applying discrete heated high conducting elements, generally segments, the heater power for each element can be adjusted to achieve a constant wall temperature over the element surface area for all elements within the investigated configuration. With this the local convective heat flux:

$$\dot{q}_{conv} = h(x) (T_w(x) - T_{ref}(x)) \quad (3.12)$$

is averaged over a segment using, in this case, a 2D-description with the element length equal to  $L$ :

$$\dot{q}_{conv} = \frac{1}{L} \int_0^L q_{conv}(x) dx = \frac{1}{L} \int_0^L h(x) (T_w(x) - T_{ref}(x)) dx \quad (3.13)$$

Since for high conducting elements (e.g. copper) the measured segment temperature will be equal to the average wall temperature and with the segments being relatively small so that the fluid reference temperature can be approximated as constant (averaged) over the segment, we have (see scheme in Fig. 3.2):

$$\dot{q}_{conv} = \frac{1}{L} \int_0^L h(x) dx (\bar{T}_w - \bar{T}_{ref}) = \bar{h} (\bar{T}_w - \bar{T}_{ref}) \quad (3.14)$$

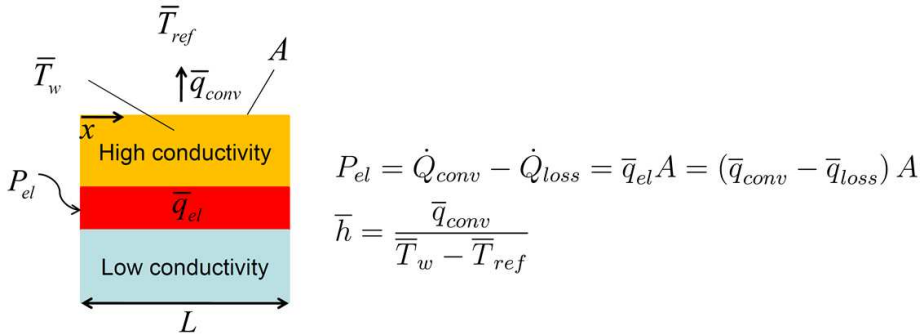


**Figure 3.2:** Diagram of heated element technique

Due to the isothermal wall condition for the segment the true surface averaged heat transfer coefficient can be obtained by measuring the average convective heat flux and the averaged surface and fluid temperatures. Furthermore, because the values of the supplied heat for each segment are known, the variations for the fluid reference temperature in stream-wise direction can be obtained relatively easily from a one-dimensional energy balance by using eq. 3.15:

$$\dot{m}_f c_p \frac{dT_b}{dx} = \int_{P(x)} \dot{q}_w(s) ds \quad \text{with} \quad T_b(0) = T_{inlet} \quad (3.15)$$

or in a segment-wise discrete form (eq. 3.16), considering elements with the same dimensions:

$$\dot{m}_f c_p (T_b(X+L) - T_b(X)) = A \sum_{j=1}^N \bar{q}_{conv,j} \quad (3.16)$$

where  $N$  is the number of elements, and  $T_b$  the bulk temperature for a given position  $X$  defined as:

$$T_b(X) = \frac{\int_A \rho_f c_p v(X, y, z) T_f(X, y, z) dy dz}{\dot{m}_f c_p} \quad (3.17)$$

This technique has been used for blade cooling applications, including also rotational effects, and it allows for temperature differences as in real blade cooling situation to reproduce the buoyancy effects for rotation. An example for a typical test model used by Wagner et al. [14, 15, 16] is given in Fig. 3.3.

The major disadvantages of this method are the restrictions to area averaged information and the relatively high instrumentation effort needed. To obtain locally resolved heat transfer distributions and to relate them to the associated flow physics in steady state experiments, thin heater foils have to be used which cover a low conducting substrate.

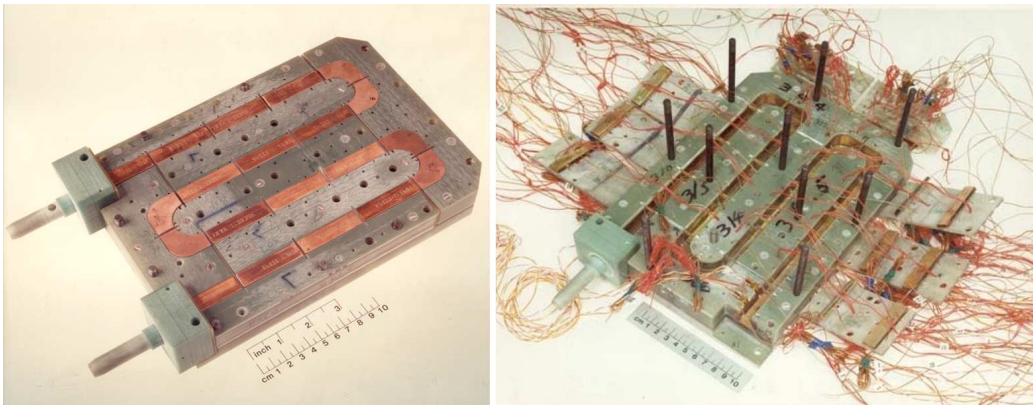


**Figure 3.3:** Cooling passages model using heated copper elements for heat transfer investigations [14, 15, 16]

### Heated Thin Foil Technique

In this method a uniform heat flux is generated by means of a thin heating foil applied over a low conductive substrate, as reported in the scheme of Fig. 3.4.

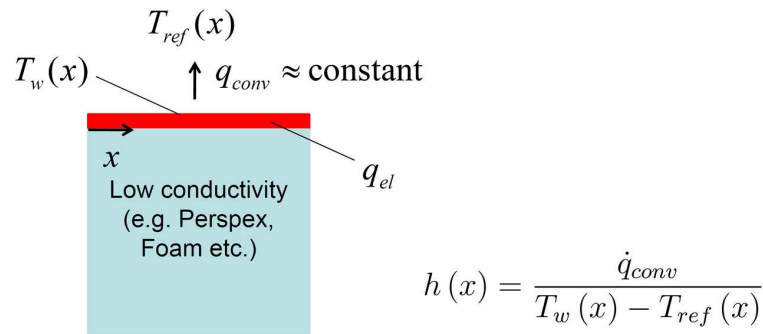


**Figure 3.4:** Diagram of the heating foil technique

If the heating layer has a constant cross section and the electrical resistance has no significant temperature dependency, the heater guarantees an isoflux boundary condition.

The local heat transfer distribution is evaluated knowing the local convective heat flux, so taking into account the heat losses with the energy balance, and measuring the local surface temperature. This can be done using local thermocouples or optical methods such as Infrared-thermography or Thermo-chromic Liquid Crystals (TLC). Depending on the optical properties of the low conducting substrate, the surface temperature might be measured through the substrate or above.

Many studies have been done at the University of Florence using this technique (see for example Maiuolo et al. [41, 42, 17]) including also the effects of the rotation (please refer to Bonanni [43]).

An example is given in Fig. 3.5 for an investigation of heat transfer of an Active Clearance Control (ACC) based on the impingement cooling using TLC, which were applied below the investigated surface and monitored through the substrate.

For the reported case, the surface heat flux is generated by the Joule

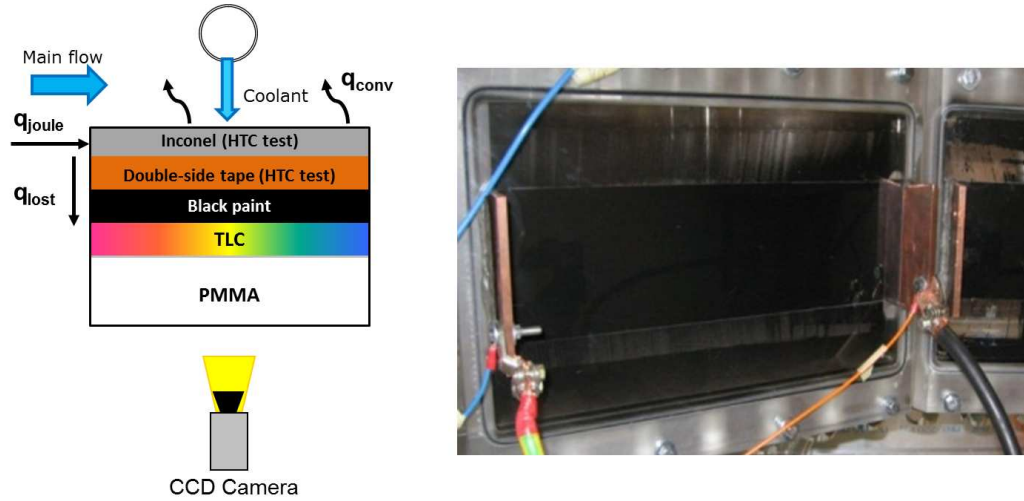


**Figure 3.5:** Thin foil technique with TLC for heat transfer measurements of an ACC system [17]

effect using a  $25.4 \mu\text{m}$  thick Inconel Alloy sheet, fed by a DC power supply connected to the Inconel sheet through two copper bus bars fixed on the extremities of the tested surface.

Heat losses are generally less than 5% of the electrical heat flux imposed at the wall. Lateral conduction heat flows occur mainly within the heating layer (due to higher thermal conductivity even at low thickness) and in the Plexiglas wall (even if it is characterized of low thermal conductivity and larger wall thickness) and depend on the actual heat transfer situation.

The limits of this method are the difficulties to affix the heating element on complex geometries (e.g. multiple curvatures, diverging/converging), so that this technique is usually applied to flat plate or single curvature walls. For more complex configurations specific heating devices might be applicable, but the local electrical field needs to be analyzed, for example, by a FEM approach, reported in Maiuolo et al. [41, 42] and Caciolli et al. [44].

### 3.2.2 Heat Transfer Transient Techniques

To overcome the disadvantages of steady state techniques with respect to the local resolution and applicability on complex surfaces, transient tech-

niques have been considered especially with temperature sensitive coatings (e.g. Ireland et al. [45, 46]).

The transient heat transfer process usually starts with the test model kept at a uniform initial temperature and the flow is set to a different temperature at the beginning of the experiment. This can be done, for example, using valves that open a closed loop bypass channel where the air is pre-heated prior to the experiment. This method, however, changes the flow situation slightly at the beginning of the tests. A very good method to change only the temperature of an already established flow situation was introduced by Ireland et al. [47, 48] using electrical heated fine wire mesh. The time constant for heating the flow using a single fine mesh is relatively low ( $< 0.1$  s) allowing for a very well defined flow temperature step. Using several connected meshes allows also to heat relatively large mass flows in a short time. The next chapter explains the fine mesh heater used for the present study (Fig. 4.2) and illustrates an example of flow temperature increase after the powered heater (Fig. 4.3).

### Thin Wall Lumped Capacitance Method

The lumped capacitance method is based on the assumption that if a solid body is immersed in a fluid with a temperature difference between the solid and the flow, the temperature of the solid is assumed to be spatially uniform at any instant during the transient process. This assumption implies that temperature gradients within the solid are negligible, which indicates an infinite thermal conductivity ( $k_s \rightarrow \infty$ ). Even though such a condition is clearly impossible, it can be closely approximated if the resistance to conduction within the solid is much less compared to the resistance to heat transfer between the solid and the surrounding flow ( $Bi < 0.1$  [49]). On this assumption, the overall energy balance relates the rate of heat loss at the surface to the rate of change of the internal energy:

$$-\dot{E}_{out} = \dot{E}_{st} \tag{3.18}$$



or

$$-hA_s (T_s - T_{ref}) = \rho_s c_p V_s \frac{dT_s}{dt} \quad (3.19)$$

If the solid body is initially at a uniform temperature:

$$T_s (t = 0) = T_i \quad (3.20)$$

this ordinary differential equation can be solved:

$$\frac{T_s - T_i}{T_{ref} - T_i} = 1 - \exp\left(-\frac{hA_s}{\rho_s c_p V} t\right) \quad (3.21)$$

This solution assumes a constant heat transfer coefficient meaning that  $h$  has to be independent of time as well as independent of the actual temperature difference  $T_s - T_{ref}$  at any time.

If in any experiment the highly conductive solid experiences a temperature step in its surroundings (from  $T_0$  to  $T_{ref}$ ) under the given assumptions, we can determine the heat transfer coefficient from the measurement of the solid temperature  $T_s(t)$ , if all other parameters are known. This is, therefore, representative for the average convective heat transfer on the surface of the body to the surrounding flow.

The lumped capacitance method is typically used to measure the averaged heat transfer coefficient on protrusion elements such as ribs, pedestals and pin fins inside cooling channels. In this case, elements are made of a high conductive material and are mounted on a well-insulated substrate. The transient heat transfer process is here described in Fig. 3.6 above. Solid body temperature is generally measured with thermocouples located inside the solid, or with optical methods such as TLC or IR-Thermography.

This method is generally combined with other different measurement approaches to determine the local heat transfer distribution in complex configurations. For example, in a latticework (vortex) cooling channel featuring angled high blockage rib arrangements, Bunker [50] applied the steady state

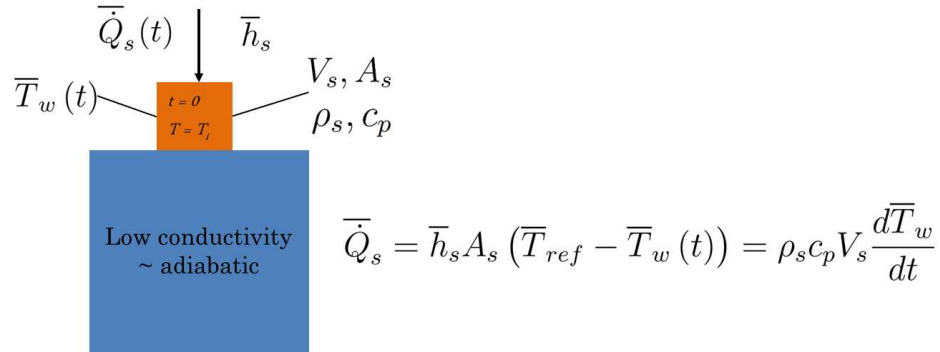


**Figure 3.6:** Diagram for lumped capacitance method to determine the averaged heat transfer coefficient on a rib

technique with the thin heating foil to measure the heat transfer between ribs and a transient IR-Thermography for a metallic model. The combination of the test results allowed to separate the heat transfer contributions from the floor and the rib surfaces including the fin efficiency of the metallic ribs. An other example can be found in Tarchi et al. [51, 52]. They performed heat transfer measurements in several trailing edge cooling configurations based on the combination of pedestals, pin fins and ribs. The average heat transfer coefficient over each pedestal and pin fins was evaluated using a full transient FEM analysis.

### Semi-infinite Wall Method

If the test model is made from a low conductive material to keep lateral conduction effects small during a transient experiment and the wall thickness is large enough, so that the thermal variation at the surface of interest does not influence the remote surface of the model, then the model under investigation can be assumed to be a one-dimensional "semi-infinite" wall and can be analyzed as such. If the assumptions of constant thermal properties and a uniform initial wall temperature of  $T_i$  and a step variation in the fluid properties at time  $t = 0$  to  $T_{ref}$  are valid, then the differential equation for

this problem is given as:

$$\frac{\partial T_s}{\partial t} = \frac{k_s}{\rho_s c_p} \frac{\partial^2 T_s}{\partial y^2} = \alpha_s \frac{\partial^2 T_s}{\partial y^2} \quad 0 \leq y < \infty \quad (3.22)$$

with the initial boundary conditions:

$$\begin{aligned} T_s &= T_i & \text{at} & \quad t = 0 \\ -k_s \left( \frac{\partial T_s}{\partial y} \right)_w &= h(T_w - T_{ref}) & \text{at} & \quad y = 0 \\ T_s &= T_0 & \text{for} & \quad y \rightarrow \infty \end{aligned} \quad (3.23)$$

Considering that the heat transfer coefficient is constant in time, this problem can be solved with the following equation:

$$\frac{T_s(y, t) - T_i}{T_{ref} - T_i} = \operatorname{erfc} \left( \frac{y}{2\sqrt{\alpha_s t}} \right) - \exp \left( \frac{\alpha_s y}{k_s} + \frac{h^2 \alpha_s t}{k_s^2} \right) \operatorname{erfc} \left( \frac{y}{2\sqrt{\alpha_s t}} + \frac{h\sqrt{\alpha_s t}}{k_s} \right) \quad (3.24)$$

Considering the wall temperature, i. e.  $y = 0$ , the eq. 3.24 becomes:

$$\frac{T_w(t) - T_i}{T_{ref} - T_i} = 1 - \exp \left( \frac{h^2 t}{\rho_s c_p k_s} \right) \operatorname{erfc} \left( \frac{h\sqrt{t}}{\sqrt{\rho_s c_p k_s}} \right) = 1 - \exp(Bi^2 \tau) \operatorname{erfc}(Bi\sqrt{\tau}) \quad (3.25)$$

where  $\tau$  is the dimensionless time, or Fourier number, since it is defined as follow:

$$\tau = \frac{\alpha_s t}{s^2} \quad (3.26)$$

and the *erfc* function is the "complementary error function" defined by:

$$\begin{aligned}
 \operatorname{erfc}(x) &= \frac{2}{\sqrt{\pi}} \int_x^{\infty} e^{-r^2} dr \\
 &= 1 - \frac{2}{\sqrt{\pi}} \left( x - \frac{x^3}{3 \cdot 1!} + \frac{x^5}{5 \cdot 2!} - \frac{x^7}{7 \cdot 3!} + \dots \right) \\
 &\approx \frac{e^{-x^2}}{\sqrt{\pi}x} \left( 1 - \frac{1}{2x^2} + \frac{1 \cdot 3}{(2x^2)^2} - \frac{1 \cdot 3 \cdot 5}{(2x^2)^3} + \dots \right)
 \end{aligned} \tag{3.27}$$

Measuring the wall temperature variation, the initial conditions ( $T_i$ ) and the fluid temperature  $T_{ref}$  during the test, it is possible to evaluate the heat transfer coefficient  $h$ . This approach is well applicable using TLC as a surface temperature measurement technique. The multiple wall temperature-time relationship (e.g. via IR-Thermography, TSP or TLC-mixtures) may, of course, improve the experimental accuracy since redundant information can be used.

A major advantage of this method is the relatively easy application on all channel walls of a cooling configuration; however, several assumptions have been made which need to be analyzed and verified otherwise additional effects need to be included in the data reduction process. These include the flow temperature change that might not be a perfect step. If  $T_{ref}(t)$  is measured, the actual temperature history might be approximated by a series of small steps and the superposition approach (Duhamel principle) used leading to:

$$T_w(t) - T_i = \sum_{j=1}^n \left[ 1 - \exp\left(-\frac{h^2(t - \hat{t}_j)}{\rho_s c_p k_s}\right) \operatorname{erfc}\left(\frac{h\sqrt{t - \hat{t}_j}}{\sqrt{\rho_s c_p k_s}}\right) \right] \Delta T_{ref(j,j-1)} \tag{3.28}$$

where  $N$  is the number of steps,  $\hat{t}_j$  the discrete times and  $\Delta T_{ref(j,j-1)}$  the temperature step between the time point  $(j - 1)$  and  $j$ .

Other assumptions to consider are the effects of finite wall thickness, surface curvature and lateral conduction that might violate the one-dimensional hypothesis.

The effect of wall thickness was analyzed by Schultz and Jones [53] with respect to the application of heat transfer gauges. Using the solution for a semi-infinite wall applying a step change in surface flux and temperature at depth  $s$  to their values at the surface are both less than 1% if the dimensionless measurement time below is:

$$\tau = \frac{\alpha_s t}{s^2} < \frac{1}{6} \quad (3.29)$$

This means that for a Plexiglas wall ( $\alpha_s \approx 1.08 \cdot 10^{-7} \text{ m}^2/\text{s}$ ) and a wall thickness of about 10 mm, the measurement should not exceed 60 seconds for eq. 3.25 to be applicable. This might not always be possible for complex geometries with long cooling channels e.g. due to thinner geometrical features (webs, divider walls, etc.), to the fluid temperature change in stream-wise direction and the therewith reduced local temperature differences between fluid and wall, so that this effect on the determined heat transfer coefficient needs to be analyzed.

Moreover, the effect of surface curvature on the evaluated heat transfer coefficient using eq. 3.25 needs to be addressed. Surface curvature effects might be important in leading edge or serpentine bend regions or if cylindrical /spherical turbulator arrangements (e.g. pins, hemispheres, dimples) are applied.

Buttsworth and Jones [54] derived an approximative solution for curved walls in similarity to eq. 3.25 valid for  $\tau_R = (t\alpha_s)/R^2 \ll 1$ , where  $R$  is the radius of curvature, which is:

$$\Theta_w = \frac{1}{1 \pm \frac{\sigma k_s}{2hR}} \left[ 1 - \exp \left( \frac{(h \pm \frac{\sigma k_s}{2R})^2 t}{\rho_s k_s c_p} \right) \operatorname{erfc} \left( \frac{(h \pm \frac{\sigma k_s}{2R}) \sqrt{t}}{\sqrt{\rho_s k_s c_p}} \right) \right] \quad (3.30)$$

where  $\sigma = 1$  is for a cylindrical surface,  $\sigma = 2$  for a spherical surface, the + sign is used for concave, the - sign is applied for convex surfaces. The solution for a spherical surface is identical to the exact solution (see [49]). Wagner et al. [55] compared this solution to the exact solution for cylindrical surfaces. Considering a cylindrical wall of finite wall thickness ( $s = R_2 - R_1$ )

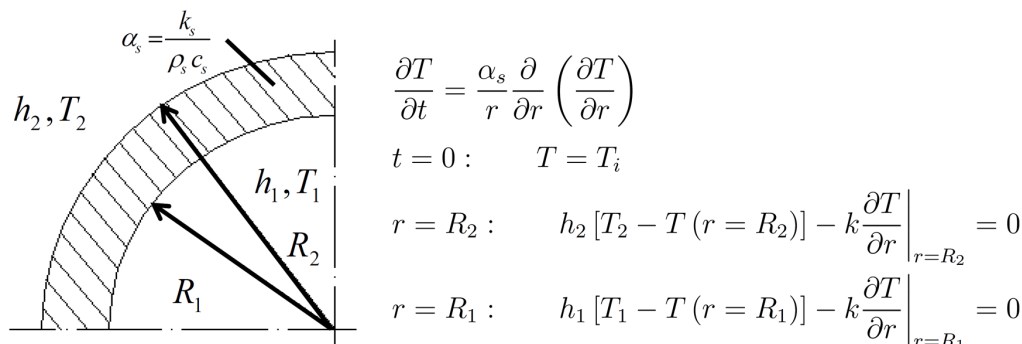


**Figure 3.7:** Transient conduction problem for curved walls of finite wall thickness

with heat transfer on both sides, the one-dimensional transient conduction problem to be analyzed is given in Fig. 3.7.

The solution of this problem can be found e.g. in Wagner et al. [55] and can be used to determine the history of surface temperatures. For  $R_1, R_2 \rightarrow \infty$  with the wall thickness  $s = R_2 - R_1$ , this solution becomes the same one as that of the plane wall of finite thickness. The effect of finite wall thickness and/or the surface curvature on the evaluated heat transfer coefficient can be then analyzed with the following procedure: for the given parameters the transient wall temperature response is calculated using the exact solution. The obtained wall temperature for a given time is then used to evaluate a heat transfer coefficient using either eq. 3.25 to address the finite wall thickness effect or eq. 3.30 to address the surface curvature effect. The obtained value is then compared to the original parameter used in the exact solution. Figures 3.8 and 3.9 show the results of this procedure. Figure 3.8 shows the ratio of the evaluated heat transfer coefficient  $h_{fp,si}$  using the flat-plate, semi-infinite wall solution (i.e. eq. 3.25) in relation to the exact parameter  $h_2$  for specific dimensionless evaluation times  $\tau$ , and the adiabatic wall at  $r = R_1$ , meaning that  $Bi_1 = 0$ , and for variations in  $h_2$  in the dimensionless form  $Bi_2, s = (h_2/s)/k_s$ .

This figure shows that the evaluated heat transfer coefficient will always be larger than the real one due to the adiabatic back side in case of a finite wall for a wide range of Biot numbers which are typical for laboratory experi-

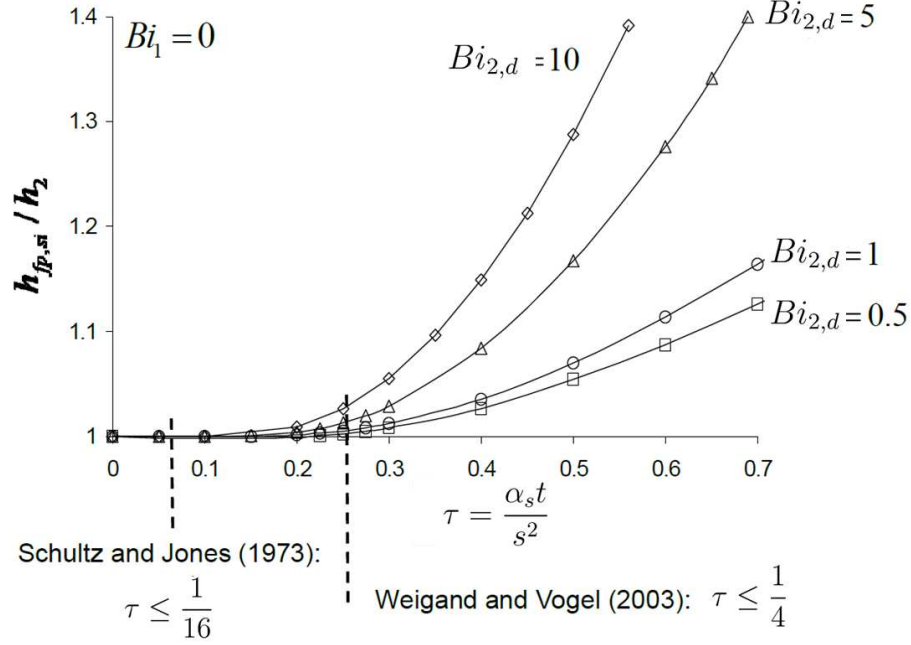


**Figure 3.8:** Effect of wall thickness

ments. It follows that as long as:

$$\tau = \frac{\alpha_s t}{s^2} \quad (3.31)$$

the error using eq. 3.25 compared to the exact case is less than 3%. Therefore, this more relaxed criterion compared to eq. 3.29 can be applied for most investigations.

Using the same procedure and the simplified solution for the curvature effects (eq. 3.30) in relation to the exact solution, the following results are obtained for a cylindrical surface (Fig. 3.9): the approximative solution provided by Buttsworth and Jones [54] covers well the curvature effects compared to the exact solution within the usual range of the heat transfer coefficient for dimensionless times based on the radius of the surface curvature  $\tau < 0.1$ . This kind of analysis can be extended to combine the effects of curvature and wall thickness, including also the convection heat transfer on the back side of a finite wall as given by Wagner et al. [55].

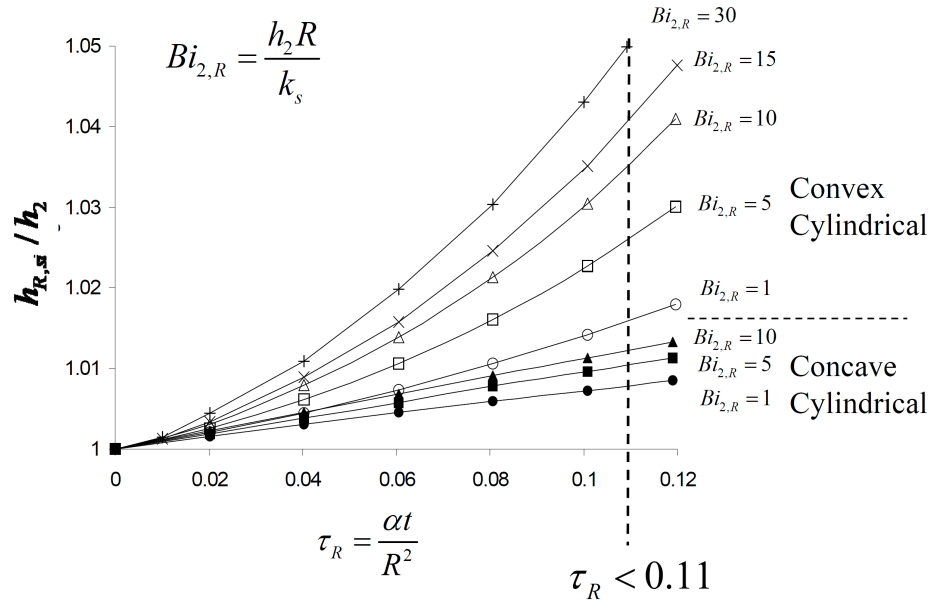


**Figure 3.9:** Effect of surface curvature

### Finite-Difference Methods

Analytical solutions to transient problems are restricted to simple geometries and boundary conditions. However, in many cases the geometry and/or boundary conditions preclude the use of analytical techniques, and recourse must be made to numerical methods, i.e. *finite-difference* methods. In this research paper only the *explicit* form of the finite-difference solutions of the transient conduction will be treated. For more details please refer to Incropera [49].

Considering a generic one-dimensional system, under transient conditions with constant properties and no internal heat generation, the appropriate form of the heat equation, already introduced in section 3.2.2, is:

$$\frac{\partial T}{\partial t} = \alpha \frac{\partial^2 T}{\partial y^2} \quad (3.32)$$

To obtain the finite-difference form of this equation, the domain represented by the solid thickness is subdivided into a number of small regions



and a reference point is assigned to each region and located at its center. This reference point is generally termed *node*, and the aggregate of points is termed *grid* or *mesh*. In the present case, the subscript  $j$  may be used to designate the  $y$  location of discrete nodal points. Considering the right term of the one-dimensional transient heat equation,  $\partial^2 T / \partial y^2$ , the value of this derivative at the  $j$  nodal point may be approximated as:

$$\left. \frac{\partial^2 T}{\partial y^2} \right|_j \approx \frac{T_{j+1} + T_{j-1} - 2T_j}{(\Delta y)^2} \quad (3.33)$$

In addition to being discretized in space, the problem must be discretized also in time. The integer  $i$  is introduced for this purpose, where:

$$t = i\Delta T \quad (3.34)$$

and the finite-difference approximation to the time derivative in equation 3.32 is expressed as:

$$\left. \frac{\partial T}{\partial t} \right|_j \approx \frac{T_j^{i+1} - T_j^i}{\Delta t} \quad (3.35)$$

The superscript  $i$  is used to denote the time dependence of  $T$ , and the time derivative is expressed in terms of the difference in temperature associated with the *new* ( $i + 1$ ) and *previous* ( $i$ ) times. Hence, calculation must be performed at successive times separated by the interval  $\Delta t$ , and just as a finite-difference solution restricts temperature determination to discrete points in space, it also restricts it to discrete points in time (Fig. 3.10).

If equation 3.35 is substituted by equation 3.32, the nature of the finite-difference solution will depend on the specific time at which temperatures are evaluated in the finite-difference approximations to the spatial derivatives. In the explicit method of solution, these temperatures are evaluated at the *previous* ( $i$ ) time. Hence, equation 3.35 is considered to be a *forward-difference* approximation to the time derivative.

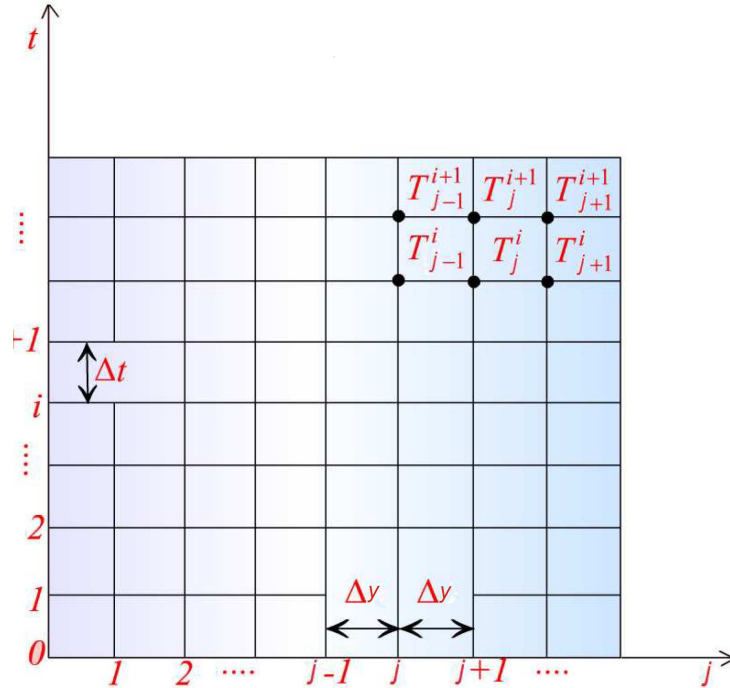


**Figure 3.10:** Finite-difference formulation of transient conduction problems

Substituting all the approximated terms in equation 3.32, the explicit form of the finite-difference equation for an interior node  $j$ , is:

$$\frac{1}{\alpha} \frac{T_j^{i+1} - T_j^i}{\Delta t} = \frac{T_{j+1}^i + T_{j-1}^i - 2T_j^i}{(\Delta y)^2} \quad (3.36)$$

It follows that the nodal temperature at the new  $(i + 1)$  time is:

$$T_j^{i+1} = Fo (T_{j+1}^i + T_{j-1}^i) + (1 - 2Fo) T_j^i \quad (3.37)$$

where  $Fo$  is the finite-difference form of the Fourier number:

$$Fo = \frac{\alpha \Delta t}{(\Delta y)^2} \quad (3.38)$$

Equation 3.37 is *explicit* because *unknown* nodal temperatures for the new time are determined exclusively by known nodal temperatures at the previous

time. Hence, calculation of the unknown temperatures is straightforward. Since the temperature of each interior node is known at  $t = 0$  ( $i = 0$ ) from prescribed initial conditions, the calculations begin at  $t = \Delta t$  ( $i = 1$ ).

The accuracy of the finite-difference solution may be improved by decreasing the values of  $\Delta y$  and  $\Delta t$ . It is obvious that the number of internal nodal points that must be considered increases when  $\Delta y$  decreases, and the number of time intervals required to carry the solution to a prescribed final time increases when  $\Delta t$  decreases. The choice of  $\Delta y$  is typically based on a compromise between accuracy and computational requirements. Once this selection has been made, however, the value of  $\Delta t$  may not be chosen independently, but it is determined by the stability requirements. The stability is determined by requiring that the coefficient associated with the node of interest at the previous time is greater than or equal to zero. This means that for a one-dimensional interior node ( $1 - 2Fo \geq 0$ ), or:

$$Fo \leq \frac{1}{2} \quad (3.39)$$

Let us now consider the surface node of the one-dimensional system shown in Fig. 3.11. In order to determine the thermal conditions near the surface more accurately, this node has been assigned a thickness that is one-half that of the interior nodes.

Considering heat convection transfer from an adjoining fluid and absence of heat generation, it follows from the energy balance that:

$$hA (T_\infty - T_0^i) + \frac{kA}{\Delta y} (T_1^i - T_0^i) = \rho c_p A \frac{\Delta y}{2} \frac{T_0^{i+1} - T_0^i}{\Delta t} \quad (3.40)$$

or, solving for the surface temperature at  $t + \Delta t$ :

$$T_0^{i+1} = \frac{2h}{\rho c_p} \frac{\Delta t}{\Delta y} (T_\infty - T_0^i) + \frac{2\alpha \Delta t}{\Delta y^2} (T_1^i - T_0^i) + T_0^i \quad (3.41)$$

Recognizing that  $(2h \Delta t / \rho c_p \Delta y) = 2(h \Delta y / k)(\alpha \Delta t / \Delta y^2) = 2 Bi Fo$  and

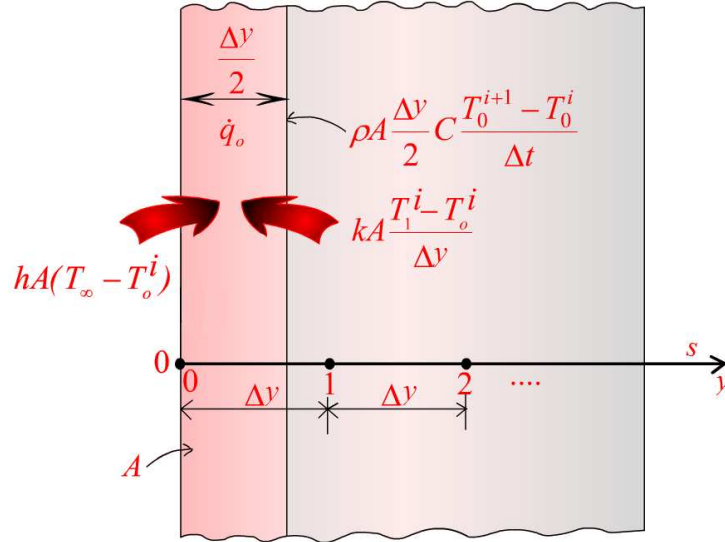


**Figure 3.11:** Diagram of the explicit finite difference formulation of the convection condition at the left boundary of the solid

grouping terms involving  $T_0^i$ , it follows that:

$$T_0^{i+1} = 2Fo (T_1^i + BiT_\infty) + (1 - 2Fo - 2BiFo) T_0^i \quad (3.42)$$

The finite form of the Biot number is:

$$Bi = \frac{h\Delta y}{k} \quad (3.43)$$

Recalling the procedure for determining the stability criterion, it is necessary that the coefficient for  $T_0^i$  is greater than or equal to zero, hence:

$$1 - 2Fo - 2BiFo \geq 0 \quad (3.44)$$

or

$$Fo(1 + Bi) \leq \frac{1}{2} \quad (3.45)$$

# Chapter 4

## Experimental Apparatus and Data Post-processing

The present chapter reports in detail the experimental apparatus starting from the test rig layout, with the vacuum system and the extraction line, the investigated geometries and the instrumentation devices used in the present experimental work. The chapter will also illustrate the data reduction procedure, from the raw experimental data to the refined results, and the uncertainties of measurements.

### 4.1 Test Rig Layout

The present experimental work has been performed at the "Sergio Stecco" Energy Engineering Department of the University of Florence. The test rig consists in an open-loop suction type wind tunnel. The vacuum system is composed of four rotary vane vacuum pumps: two with a capacity of 900 m<sup>3</sup>/h each (PVR) and two with 300 m<sup>3</sup>/h each (Becker). The mass flow rate is controlled by the speed of the pumps. The test rig was designed in order to satisfy different requirements of the tested models, that are the impingement jet Reynolds number similitude and different extraction arrangements. Therefore, several leading edge models were designed with different scale factors (SF).

As reported in Figure 4.1, all the models share the extraction lines composed

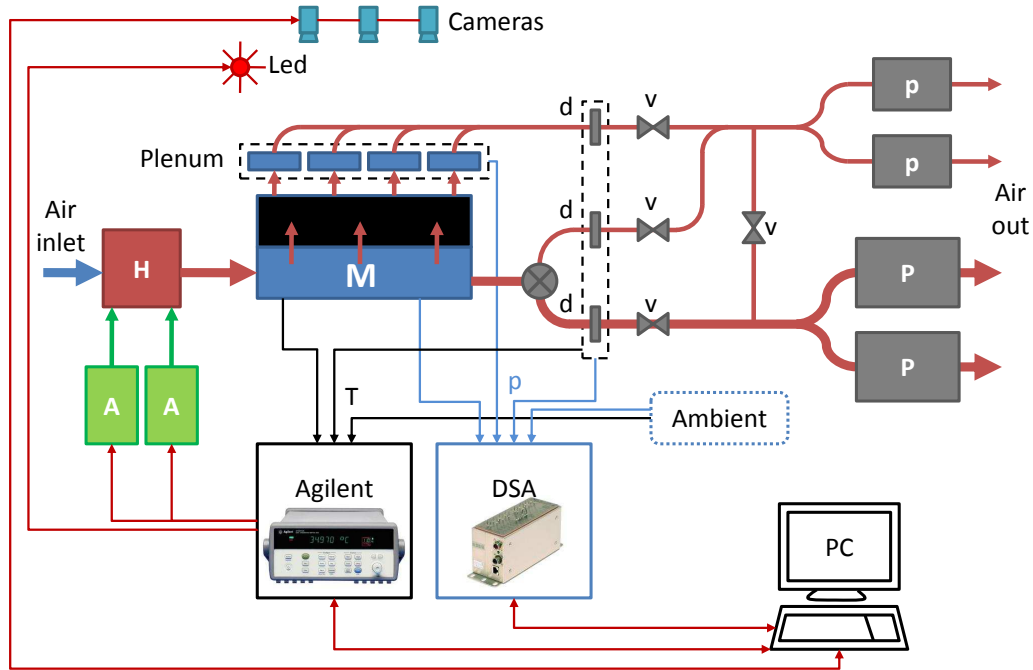
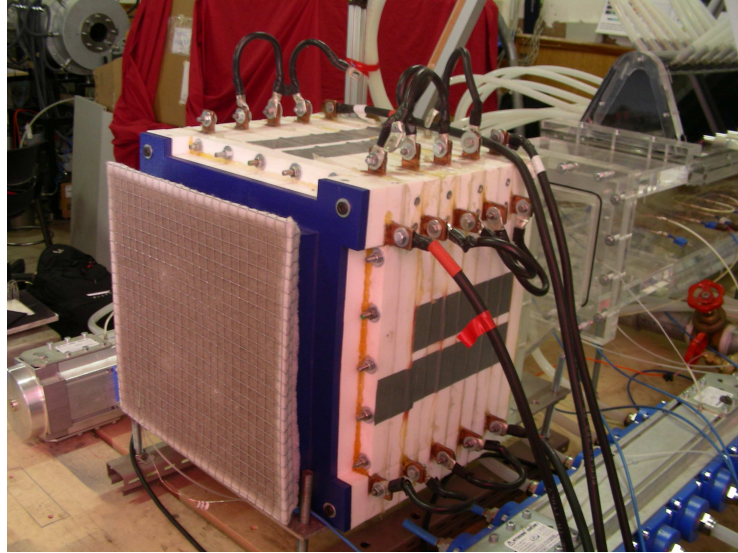


Figure 4.1: Test rig layout

of 2" and 6" ducts, that are connected to the vacuum pumps. A series of ball valves, located along the extraction lines, allow to select which pump, or pumps, to use in order to choose the best solution between the mass flow required and the related pressure losses. In vacuum systems, as in the present case, the mass flow extracted by the pumps is dependent on the total pressure at the inlet of the pumps, so an accurate estimation of the pressure losses across the extraction line is necessary to evaluate the maximum mass flow rate, hence the maximum jet Reynolds number, that can be generated.

As shown in Fig. 4.1, the test rig is composed of an inlet section where air at atmospheric pressure and ambient temperature passes through a ten-stage mesh heater in order to provide an instantaneous and uniform temperature step change to the inlet mass flow. More details on the heater will be given in section 4.1.1. After the heater, the flow enters the supply channel of the tested model and impinges onto the internal surface of the leading edge cavity through the impingement geometry. The flow in the leading edge cavity



**Figure 4.2:** Picture of the mesh heater

is then extracted by means of four arrays of circular holes simulating the shower head and film cooling extraction. With regard to the measurements performed on AVIO models, the extraction at the tip of the feeding channel is also present in order to reproduce the different crossflow conditions at the hub, mid-span and tip of the real blade.

The extraction hole arrays are connected to four distinct plenum, one for each array, by means of flexible hoses. The mass flow extracted from each plenum can be regulated with several gate valves. More details on the plenum features are given in section 4.1.2.

The total mass flow rate varied between 0.04 - 0.30 kg/s in order to cover all the tests planned in the test matrix.

#### 4.1.1 Mesh Heater

The heater used for the present experimental activity is a mesh heater (Fig. 4.2). The mesh heater (patented by Gillespie et al. [56]) is composed of ten independent stages. Each stage is made of a PTFE frame, a 304 stainless steel woven wire mesh with a wire diameter of 0.030 mm and a distance between the wires of 0.039 mm, and four copper bus bars that tighten the mesh and allow the electrical connection with the power supply.

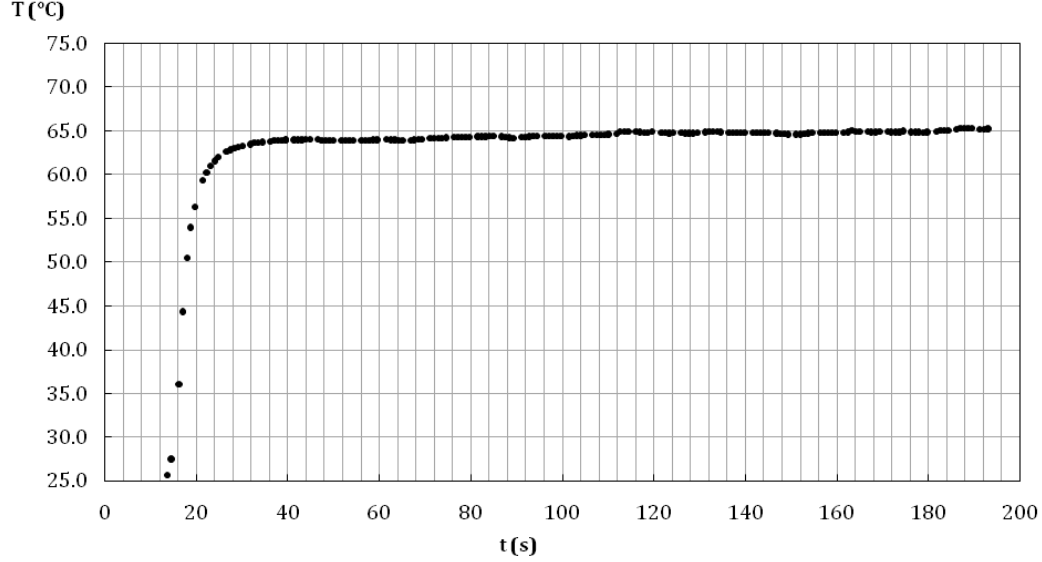


**Figure 4.3:** Main flow temperature variation ( $\dot{m} = 0.170$  kg/s)

The mesh heater is fed by two Zivan NG7 DC power supplies with a maximum electrical power of 11 kW, which is then transferred as thermal power to the fluid. This heating system guarantees a uniform spatial temperature distribution and a step variation in time, as reported in Fig. 4.3.

For each test, the number of the powered grids was chosen in order to have a mainflow temperature between 50 and 65°C, depending on the jet Reynolds number and, consequently, on the expected heat transfer coefficient. Once the mass flow rate and the ambient temperature are known, and imposing the final asymptotic mainflow temperature, it is possible to evaluate the thermal power to transfer to the fluid, applying the energy balance:

$$\dot{Q} = R \cdot I^2 \cdot \eta_g = \dot{m} \cdot c_p \cdot \Delta T \quad (4.1)$$

where  $R$  is the electrical resistance of the mesh,  $I$  the current intensity, and  $\eta_g$  the grid efficiency. This thermal power is transferred to the fluid by convection.



### 4.1.2 Extraction Plenum

In the real blade a different external pressure gradient is present, leading to higher pressure levels on the pressure side and lower levels on the suction side. Considering a uniform pressure distribution inside the blade, the mass flow discharged from the film cooling and shower-head holes will be different along the blade profile. In order to reproduce a different mass flow distribution due to the different external pressure gradient, four independent plenums have been used. The mass flow extracted from each plenum can be controlled by means of gate valves. In this configuration it is not possible to insert a flow meter, or similar mass flow measurement devices, due to the very short length of the ducts. Therefore, to estimate the mass flow extracted from each plenum, a preliminary fluid-dynamic characterization was performed to evaluate the flow function, considering each plenum as a concentrated pressure loss.

Figures 4.4 and 4.5 report the mass flow extracted from each plenum as a function of the pressure ratio ( $p_{cr}/p_{pl}$ ), for both AVIO and ALSTOM test rigs. In particular, for the AVIO tests, the evaluated flow functions allow to

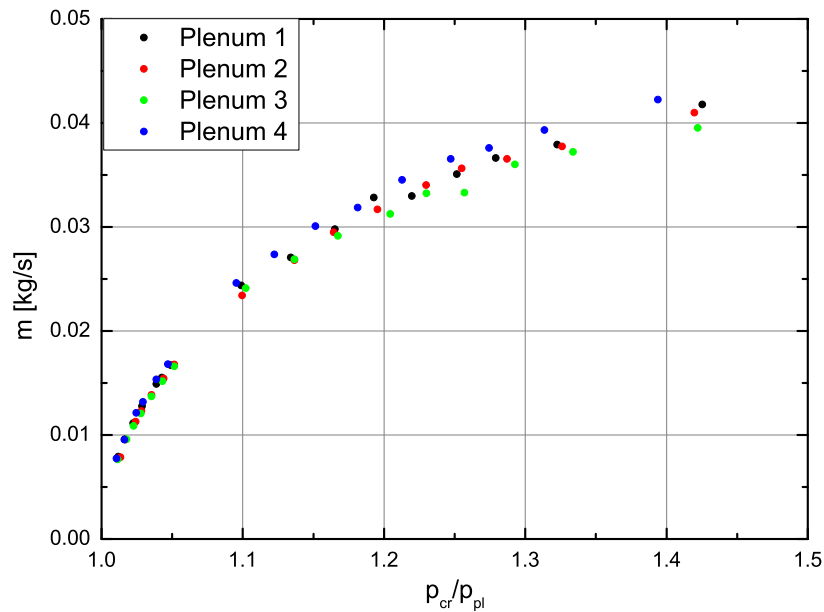
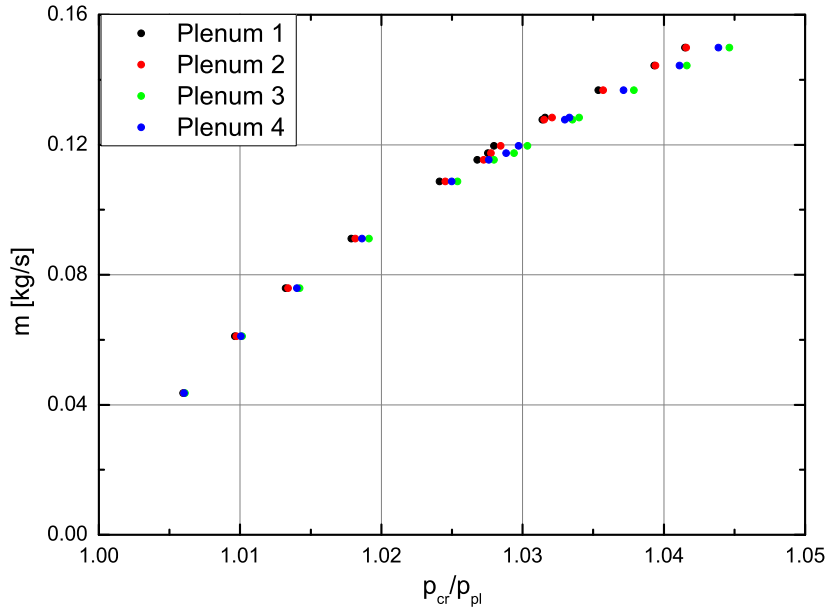


Figure 4.4: AVIO plenum characterization



**Figure 4.5:** ALSTOM plenum characterization

set a different mass flow split, by imposing a different static pressure level in each plenum.

With regard to the ALSTOM tests, the mass flow extracted from the four arrays is the same, so the fluid-dynamic characterization was done only to verify the absence of leakages, and also the symmetrical distribution of the pressure losses along the flexible hoses.

## 4.2 Tested Geometries

All the tested models are entirely made of transparent PMMA ( $k = 0.19$  W/mK), in order to obtain the required optical access for TLC measurements and to limit thermal losses across the material.

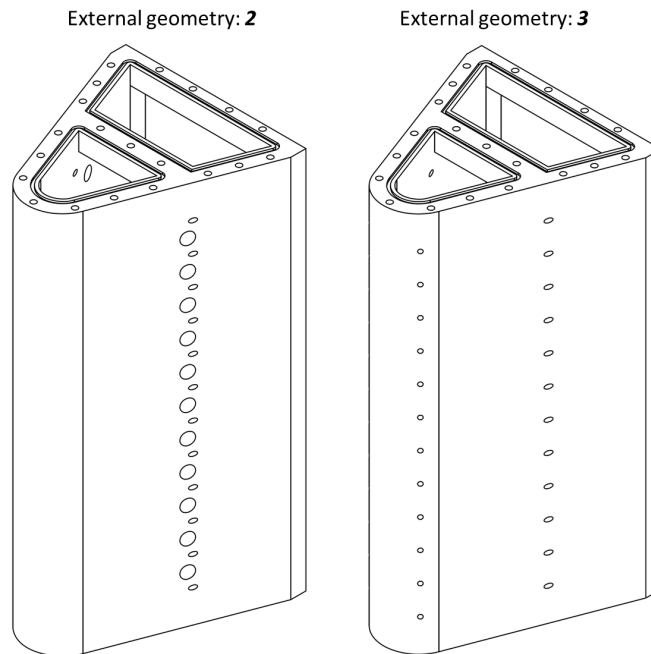
Two different sections are dedicated to AVIO (§4.2.1) and ALSTOM (§4.2.2) tested models.

### 4.2.1 AVIO Geometries

A preliminary analysis made by AVIO during the first period of the project, has allowed to select the geometries of interest for the experimental survey.

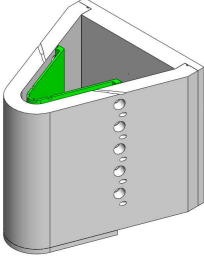
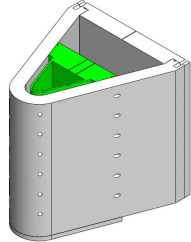
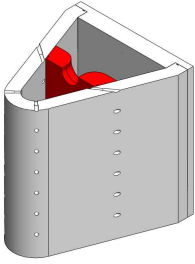
The AVIO tested geometries are composed of two different external leading edge models and three internal impingement geometries. The external geometries, named **2** and **3** and shown in Fig. 4.6, have the same geometrical characteristics but differ in the extraction system: geometry **2** has the extraction only from the film cooling holes, and an additional array of extraction holes is present to draw in all of the coolant flow, while geometry **3** has the coolant extraction both from the film cooling and the shower-head holes.

A total of three different leading edge cooling systems have been tested combining the above mentioned external models **2** and **3** with three internal impingement geometries. Table 4.1 reports the main geometrical parameters of the three systems, while Fig. 4.7 illustrates more in detail the three inter-



**Figure 4.6:** AVIO external leading edge models

nal impingement geometries.

Geometry	SF	$d_j$ [mm]	n	$S_y/d_j$	$Z/d_j$	$l/d_j$
B2 	10:1	7	76	3.83	1.57	0.57
B3 	10:1	6.35	60	6	1.73	0.63
C3 	43:1	50.84	3	3.75	2.36	0.85

**Table 4.1:** AVIO tested geometries

Geometry **B2** is characterized by a radial inlet flow which enters the trapezoidal feeding channel, then impinges on the internal surface of the leading edge through the impingement geometry with 4 arrays of circular holes, and it is extracted from the cavity by means of film cooling holes. Measurements have been performed at 5 different jet Reynolds numbers:  $Re_j = 5500 - 8250 - 11000 - 16500 - 22000$ .

Geometry **B3** is characterized by a radial inlet flow entering directly in the leading edge cavity. Part of the flow impinges on the internal surface of the leading edge through the impingement geometry and the remaining amount of mass flow is extracted at the tip of the model. Varying the ratio between the impingement flow and the crossflow extracted at the tip of the model, it is possible to experimentally reproduce the different feeding conditions of

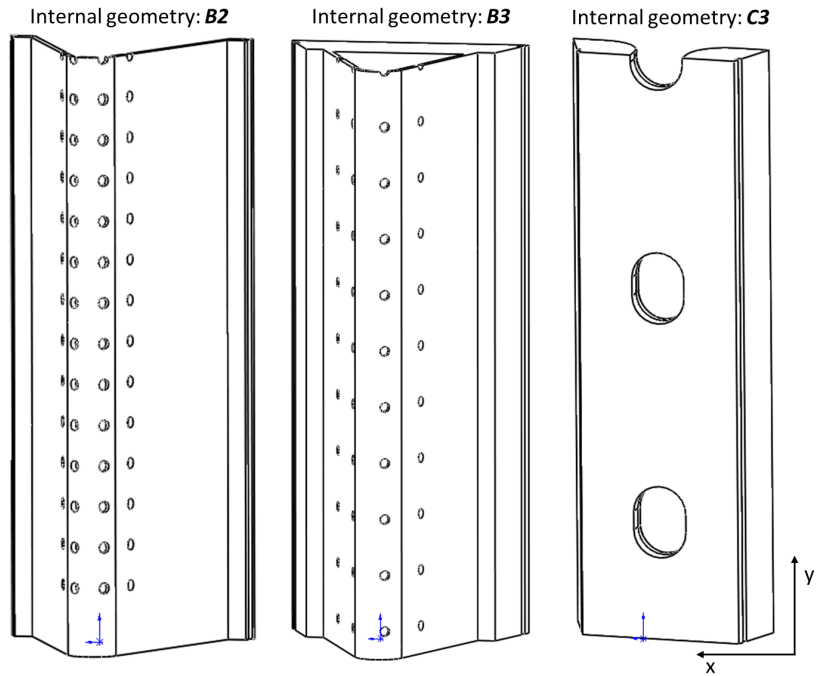


Figure 4.7: AVIO internal leading edge models

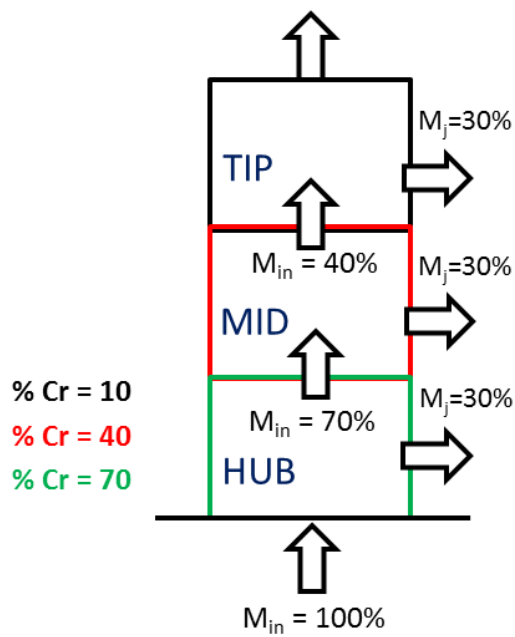


Figure 4.8: AVIO crossflow condition schematic diagram

the hub, mid-span and tip of the real blade (see schematic diagram in Fig. 4.8). The impingement geometry has 4 arrays of circular holes, similarly to geometry **B2**, but they are located asymmetrically along the circumferential direction. Measurements have been performed at 5 different jet Reynolds numbers:  $Re_j = 4000 - 7250 - 8500 - 10500 - 17000$ , and three crossflow conditions:  $\% Cr = 10 - 40 - 70$ .

Geometry **C3** has a radial inlet flow entering the trapezoidal feeding channel. Similarly to geometry **B3**, part of the flow impinges on the internal surface of the leading edge through the impingement geometry and the remaining amount of mass flow is extracted at the tip of the model. The impingement geometry is characterized by three large racetrack holes and four large fins inside the leading edge cavity. Measurements have been performed at 5 different jet Reynolds numbers:  $Re_j = 10000 - 20000 - 30000 - 40000 - 50000$ , and three crossflow conditions:  $\% Cr = 10 - 40 - 70$ .

#### 4.2.2 ALSTOM Geometries

ALSTOM tested geometries are composed of two different external leading edge models and eight internal impingement geometries. The models are enlarged with a scale factor SF of 10:1.

The external geometries, named **LE 1** and **LE 2** and illustrated in Fig. 4.9, differ only in the leading edge opening angle ( $\vartheta$ ):  $70^\circ$  and  $100^\circ$ .

The internal impingement geometries are rectangular plates that separate

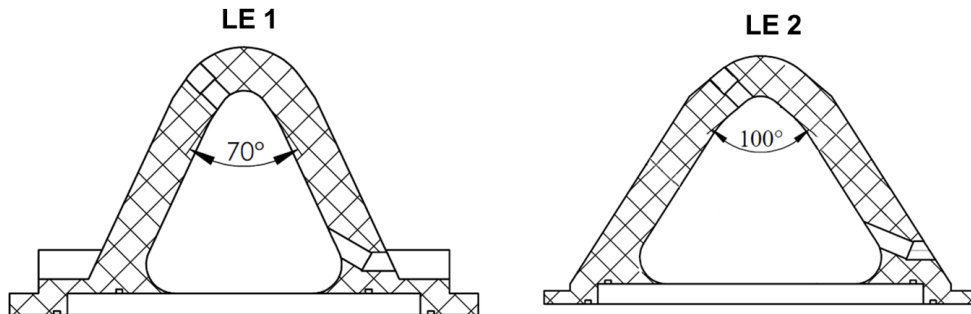


**Figure 4.9:** ALSTOM leading edges

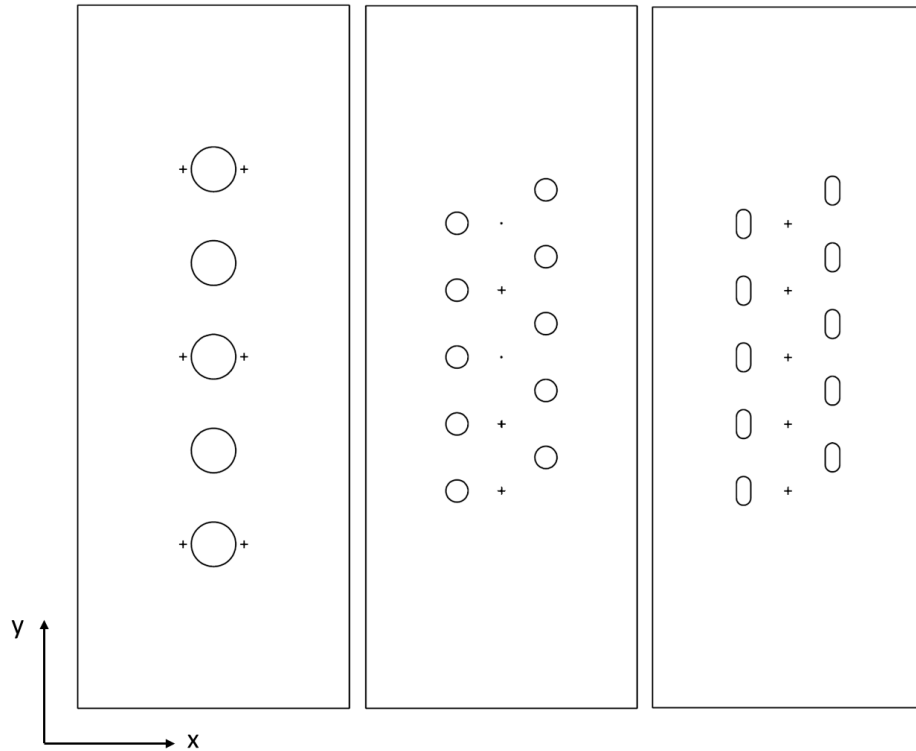


**Figure 4.10:** ALSTOM internal impingement geometries

the leading cavity from the feeding channel.

These geometries differ in the number, the shape and the position, in radial and tangential-direction, of the jets. Figure 4.10 shows some of the tested internal geometries. A total of 12 configurations have been tested, varying both the external and the internal geometries. Moreover, the effect of the shower-head extraction was taken into account (configuration G5).

All of the planned tests are reported in Table 4.2, with the main geometrical features of each geometry.

Each geometry has been tested at four different jet Reynolds number:  $Re_j = 15000 - 25000 - 35000 - 45000$ , where the jet Reynolds number is calculated considering the hydraulic diameter  $d_j$  of the impingement jets as the reference length.

Geometry	$\vartheta$ [deg]	n	$d_j$ [m]	$S_x/d_j$	$S_y/d_j$	$Z/d_j$	$l/d_j$	$D/d_j$
<b>G1</b>	70	5	0.04	-	2.1	3.4	0.83	0.88
<b>G2</b>	70	10	0.02	4	3	4	1.65	1.75
<b>G3</b>	70	10	0.0181	4.3	3.3	4.4	1.82	1.93
<b>G4</b>	100	5	0.04	-	2.1	3.5	0.83	0.88
<b>G5</b>	100	10	0.02	4	3	5.23	1.65	1.75
<b>G6</b>	100	10	0.02	3	3	5.95	1.65	1.75
<b>G7</b>	100	10	0.02	4.5	3	4.84	1.65	1.75
<b>G8</b>	100	10	0.02	5	3	4.53	1.65	1.75
<b>G9</b>	100	10	0.02	4	4	5.23	1.65	1.75
<b>G10</b>	100	10	0.02	4	5	5.23	1.65	1.75
<b>G11</b>	100	10	0.02	4	3	5.23	1.65	1.75
<b>G12</b>	100	10	0.0181	4.3	3.3	5.78	1.82	1.93

Table 4.2: ALSTOM tested geometries

## 4.3 Measuring Devices

Test rigs are equipped with thermofluid-dynamic and optical measurement devices in order to describe the fluid properties and to evaluate the heat transfer coefficient distribution. This section is dedicated to the description of such instrumentations.

### 4.3.1 Mass Flow Rate Measurements

Mass flow rate measurements are required to set the jet Reynolds number and, in some cases, to impose the crossflow conditions. The mass flow rate is measured according to the standard UNI EN ISO 5167-1, by means of two orifices located at the end of the wind tunnel. Static pressure measurements are located at  $D$  and  $D/2$  from the orifice, where  $D$  in the present case represents the hydraulic diameter of the duct (Fig. 4.11). A temperature measurement is also required to calculate the density of the flow, and hence the mass flow rate.

In order to maximize the measurement accuracy, different orifices sizes (12.5



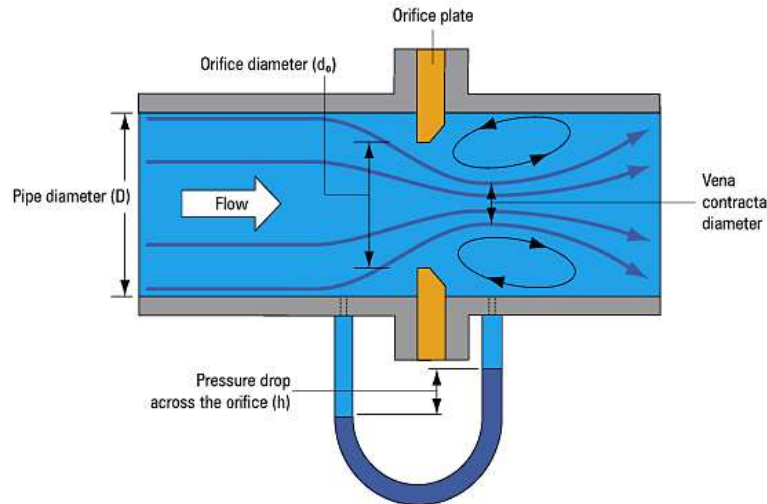


**Figure 4.11:** Orifice plate mass flow measurement

mm, 25 mm, 37.1 mm, 37.5 mm for the 2" duct and 76 mm for the 6" duct) have been used depending on the mass flow rate to be measured, with a measurement accuracy below 2%.

### 4.3.2 Static Pressure Measurements

As described in the previous sections, pressure measurements are required to calculate the mass flow rate through the orifices (§4.3.1) and in each extraction plenum (§4.1.2). Moreover, other static pressure taps have been located inside the tested models to evaluate the fluid properties and pressure losses along the test rig.

Static pressure measurements have been performed using two pressure scanners Scanivalve DSA 3217 Digital Sensor Array (Fig. 4.12). Each scanner incorporates 16 temperature compensated piezoresistive pressure sensors with a pneumatic calibration valve, a RAM memory, a 16 bit A/D converter, and a microprocessor. The microprocessor compensates for temperature changes and performs unit conversion. Pressure data are output in engineering units via Ethernet using the TCP/IP protocol.

The DSA modules used for the present activity have multiple pressure ranges



**Figure 4.12:** Scanivalve DSA pressure scanner

with a total of 8 channels of 1 psid ( $\simeq 7000$  Pa) and 0.20% F.S. of accuracy, 16 with 5 psid ( $\simeq 35000$  Pa) and 8 channels with 15 psid ( $\simeq 100000$  Pa) and 0.05% F.S. of accuracy. These sensors measure a differential pressure, so an absolute pressure is needed as a reference value. In the present case, the reference pressure used was the ambient pressure given by a mercury barometer.

### 4.3.3 Flow Temperature Measurement

Temperature measurements of the elements involved in the heat exchange are fundamental in convective heat transfer problems. Measurements are focused on the elements involved in the heat exchange, that in the present case are the flow and the internal surfaces of the leading edge.

The wall temperature has been measured by means of thermo-chromic liquid crystals, that will be described in section 4.4.

The flow temperature has been measured with several T-type thermocouples (copper - constantan) connected to a data acquisition control unit (Agilent 34970A), and acquired with a PC via a GPIB interface.

Thermocouples were found in different locations:

- at the inlet of the test rig, to get the ambient initial conditions,
- inside the model, to measure the flow temperature at different locations

during the test,

- inside the extraction plenum and in correspondence of the orifices, to evaluate the flow density and hence the mass flow rate.

The position of the thermocouples located inside the model was varied between each geometry, depending on the position of the jets and on the flow arrangement, in order to obtain the temperature variation of the jets for the HTC data reduction procedure.

Thermocouples used are sheathed, with different wire diameters: 0.5 mm, for the impingement jets temperature to get the temperature step variation of the flow inside the model, and 1 mm for the other probes.

These instruments have an accuracy range of 0.5 K certified by the manufacturer. The temperature of the reference junction has been measured by means of a RTD Pt100 sensor with a global accuracy of 0.1 K.

## 4.4 Thermo-chromic Liquid Crystals

Wall temperature measurements of the internal leading edge surfaces have been performed using Thermo-chromic Liquid Crystals.

TLCs are temperature indicators that modify incident white light and display color whose wavelength is proportional to the temperature. Usually clear, or slightly milky in appearance, liquid crystals change in appearance over a range of temperature called the "color-play interval" [57] (the temperature interval between first red and last blue reflection), starting from the "activation temperature" that represents the minimum temperature of the color-play interval at which the displayed color is red. Outside this activation temperature range, they become transparent again. More details on the working principle and properties of thermo-chromic liquid crystals can be found in [57, 58, 59].

TLCs can be found in different formulations depending on the width of the color-play interval; substantially, they are divided into *narrow band* (1 - 2°C) and *wide band* (5 - 30°C).

In the present study, measurements have been performed using a narrow

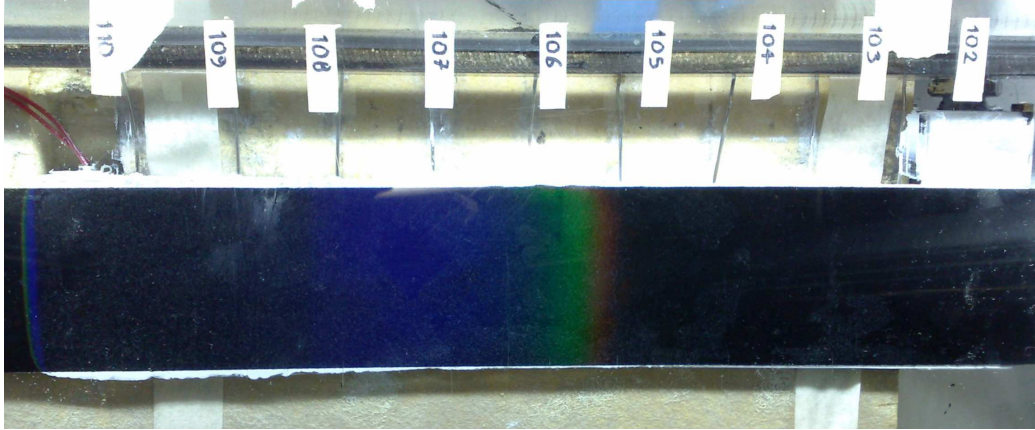


**Figure 4.13:** Calibration setup

band TLC supplied by Hallcrest Ltd and active from 40°C to 41°C. Crystals are thinned with water and sprayed with an airbrush onto the tested surfaces; successively, a water base black paint is sprayed to obtain a black background.

The TLCs have been calibrated to replicate the same optic conditions of the real test: the green color peak intensity is found at 40.5°C and it is the most repeatable and evident effect, so it was used as the event temperature in the data reduction procedure.

The TLC calibration was performed following the steady state gradient method (see Chan et al. [60]). Figure 4.13 shows the calibration set up. It is made of a 4.5 mm thin aluminium rectangular plate, housing seven thermocouples, sprayed with black background paint and then the TLCs. One of the edges is heated by an electric heater, while the other is cooled by air. The whole apparatus is housed in an insulated base. The digital camera and illumination system are placed at the same distance and inclination of the real test, so as to replicate the exact optic conditions. A linear temperature gradient will appear on the TLC surface: once steady conditions are reached, a single picture is sufficient to relate the color information acquired by the camera with the temperature measured by the thermocouples. The experiments were repeated several times in order to increase global accuracy.

## 4.5 Video Acquisition

Due to the large dimensions of the models, the complete view of the whole measurement section was obtained using three digital cameras Sony XCD-SX90CR equipped with Tamron M118FM08 lenses (Fig. 4.14). The cameras simultaneously record a sequence of raw bitmap images ( $1280 \times 480$  pixel - 7 *fps*) from the TLC painted surface on a PC via IEEE 1394b interface (Firewire 800) and acquired with the Unibrain Fire-i software. One camera records the leading edge curved region while the other two record the lateral walls.

The illumination system is composed of four 8W white LED arrays (120 LED) of 750 - 800 lumen, to ensure a uniform illumination on the tested surface. The synchronization between the optical and the thermo-fluid dynamic measurements is performed using a red light visible from all the three cameras, that is controlled by a actuator/GP switch module inserted in the data acquisition unit Agilent.



**Figure 4.14:** Camera used for video acquisition

## 4.6 Post-processing Procedure

The experimental methodology used in the present work is the transient technique already described in chapter 3. For each experiment, this procedure gives a set of thermal and fluid-dynamics data measured with thermocouples and pressure taps, and a sequence of bitmap images, acquired from the three digital cameras. The following description of the post-processing procedure is the same for all the tested geometries.

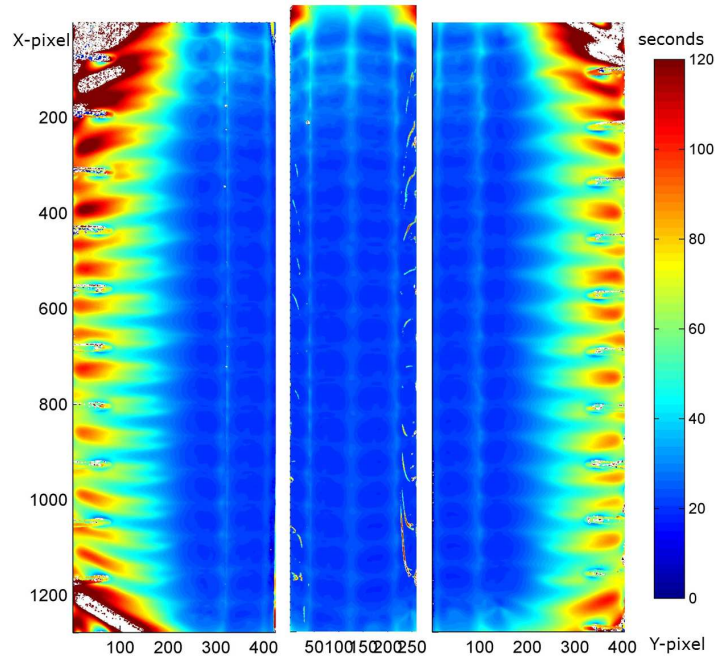


**Figure 4.15:** Event time matrices of geometry AVIO B2

The first step is the synchronization between the fluid-dynamic data and the sequence of bitmaps. This task allows to correctly define the beginning of the transient test: a shift of the zero point can lead to significant measurement errors in the evaluation of the heat transfer coefficient. The synchronization is done by means of a red light located close to the model and visible from the three cameras, that is switched off at the beginning of the test by means of the actuator/GP switch module inserted in the data acquisition unit Agilent and controlled from the PC.

Each bitmap image acquired from the cameras is in RAW format that contains minimally processed data from the image sensor of the digital cameras. A demosaicing algorithm is used to reconstruct a full color image with a color filter array (CFA). A Matlab macro is used to detect the green peak intensity for each pixel throughout the acquired images. The result of this procedure is an *event time* matrix that represents the time required for each pixel to reach the green peak intensity, as illustrated in Fig. 4.15. Event time matrix is one of the input parameters for the solution of the Fourier's

heat conduction equation, the other inputs are the variation of the air flow temperature during the test, the initial conditions and the material properties.

As described in section 3.2.2 dedicated to the measurement techniques with transient procedure, Fourier's equation might be solved applying the semi-infinite wall method. However, due to the complex geometry considered in the present study, the assumption of one-dimensional heat conduction through a flat wall would surely introduce errors in the evaluation of the heat transfer coefficient. Therefore, the finite-difference method has been applied dividing the tested geometry into two distinct parts: the central concave region, that was solved considering a cylindrical domain, and the lateral walls of the leading edge, that can be assimilated to flat walls.

The solution of the Fourier heat equation was performed with the in-house code `HTCvalue`. On each point of the event time matrices, the program calculates the heat transfer coefficient with an iterative procedure, applying the following steps:

1. setting of a first-attempt heat transfer coefficient
2. solution of the Fourier heat equation with the imposed heat transfer coefficient until the event time  $t^*$
3. comparison between the wall temperature  $T(0, t^*)$  calculated with the imposed HTC and the event temperature known from the TLC calibration
4. if the difference between the two temperatures is less than a defined quantity (typically  $0.001\text{ }^\circ\text{C}$ ), the imposed heat transfer coefficient is considered valid, otherwise the procedure restarts from point 1, changing the assumed HTC until the convergence of the procedure.

Considering that images acquired from the cameras have a resolution of 1280 x 480 pixel (about 500000 - 600000 points depending on the images crop), the iterative procedure described above would take a lot of time to calculate all the selected points. For this reason, a fast-procedure approach was implemented in the program to strongly reduce the computational time.

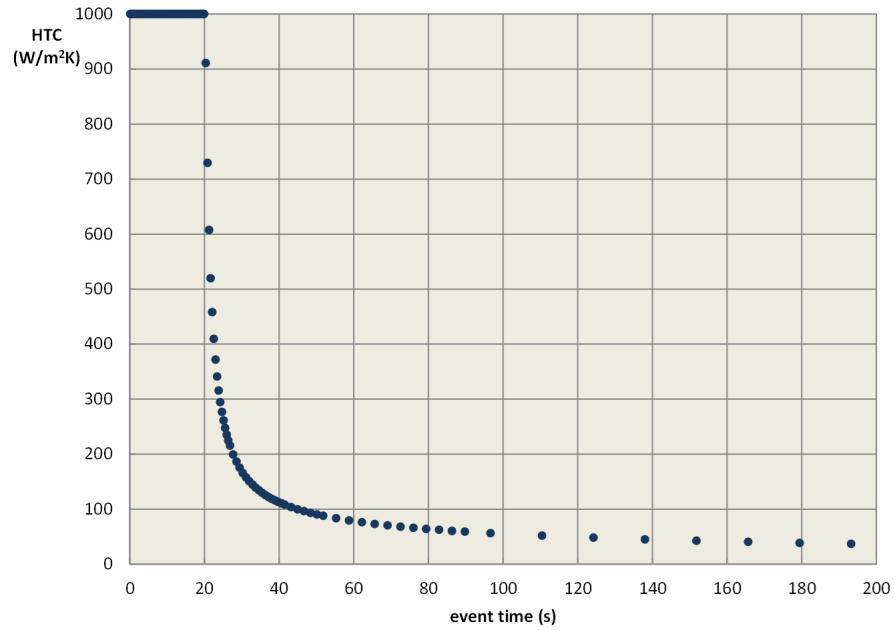


**Figure 4.16:** Fast-approach curve for finite-difference method

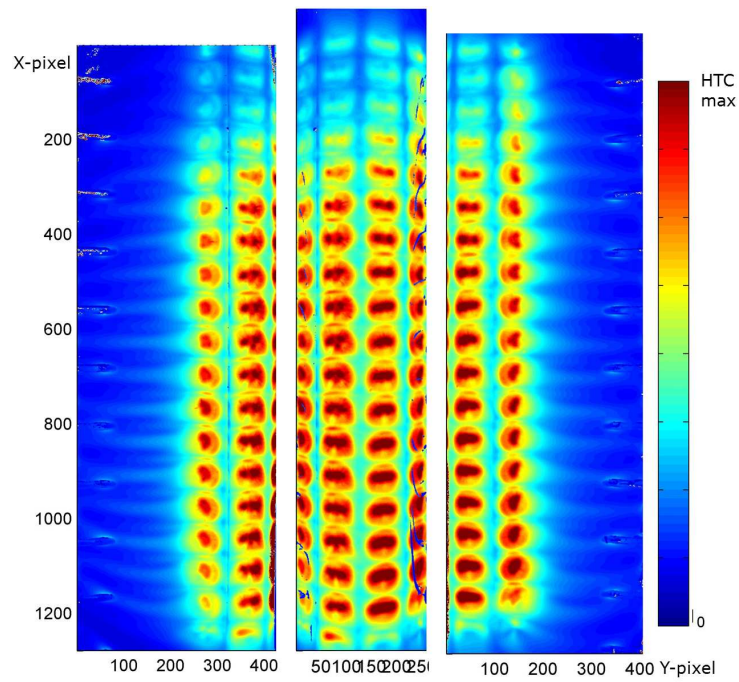


**Figure 4.17:** HTC result from HTCvalue of AVIO B2 geometry



The fast-approach procedure is based on the application of the iterative procedure only for a limited number of points (generally 500). These points are then interpolated in order to obtain a relationship  $h = f(t)$  between the heat transfer coefficient and the event time, as reported in Fig. 4.16. For all the remaining elements of the event time matrices the program applies the interpolated curve. The maximum error introduced with the present procedure is around 0.1% of the extrapolated heat transfer coefficient, therefore clearly negligible.

The `HTCvalue` output is represented by the heat transfer coefficient maps for each camera, as reported in Fig. 4.17.

Contour plots need further post-processing for the refinement of the HTC data. In particular, looking at Fig. 4.17, there are areas where the one-dimensional heat conduction assumption is not valid (e.g. extraction holes),

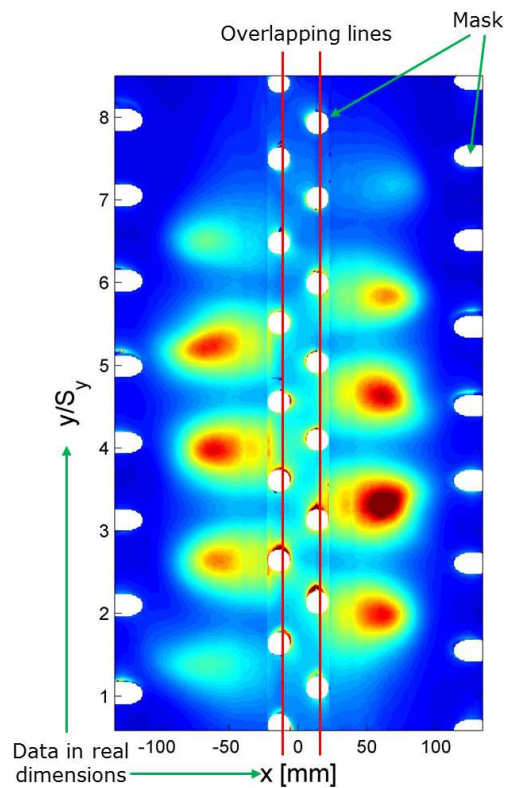


**Figure 4.18:** HTC result from EPROM.m of ALSTOM G9 geometry

or where the TLC paint does not reach the green peak intensity, due to very low heat transfer coefficient values. These regions have to be covered or treated in a different way, moreover, maps need to be resized in order to obtain the same dimensions for the overlapping of the images. In particular, images acquired from the camera focused on the curved surface were interpolated with a x-curvilinear abscissa in order to obtain the "unrolled" internal HTC contour plot.

All of these modifications were done with a macro written in Matlab (`EPR0M.m`). Input data for the macro are represented by the real dimensions in mm of the tested geometries, i.e. the impingement jet size, the distances between the extraction holes, the curvature of the leading edge, and the image crop that defines the overlapping lines between the three HTC matrices.

The final result of this procedure is visible in Fig. 4.18, where contour plots are interpolated to have the same dimensions, overlapped and masked with NaN elements. For the present case, the overlapping was done along the shower-head arrays that represent a common reference visible from the cameras.

The refined and overlapped results allow to correctly extract all the requested information, such as jet stagnation region dimensions, averaged values in radial and tangential directions, and spatially averaged data of the single jet stagnation regions or of a portion of the matrix, as will be shown in the Results chapter.

This entire procedure is summarized in the block diagram reported in Fig. 4.19, starting from the raw data to the final refined HTC/Nusselt number results.

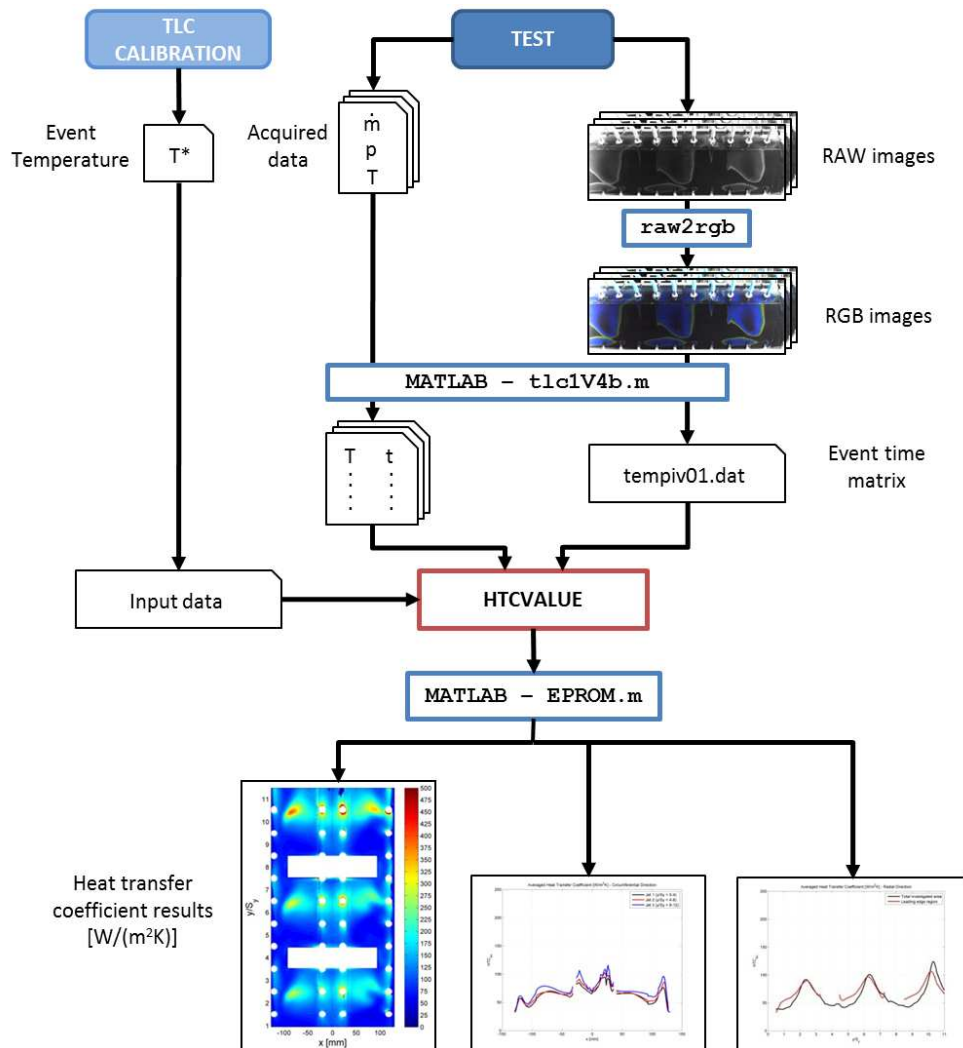


Figure 4.19: Measurement post-processing procedure

## 4.7 Measurement Uncertainty

All the data derived from experiments or tests are measured with devices and sensors that are characterized by an instrumentation accuracy. So it is fundamental to know what the accuracy or the measurement uncertainty related to a single or multiple data measured is.

For the present study, the techniques used to carry out the uncertainty analysis follows the method presented by Kline and McClintock [61].

On the whole, the uncertainty analysis may be divided into two parts:

- determining the uncertainty in primary or direct measurements,
- determining the uncertainty in a result derived from those measurements.

A primary measurement is one that is not derived from any other, e.g. voltage from a voltmeter, temperature from a thermometer, etc. Each primary measurement should be given the related *uncertainty interval* that is the symmetrical band around a measurement within which the true value should lie. For example, a certain temperature measurement might be expressed as:

$$T = 330K \pm 0.5K$$

In case of a set of measurements, as in the present work for the determination of the mass flow rate and the heat transfer coefficient that are derived from direct measurements, the global uncertainty on the indirect result  $R$  is a given function of the independent variables  $x_1, x_2, x_3, \dots, x_n$  and their uncertainties:

$$R + \Delta R = f(x_1 + \Delta x_1, x_2 + \Delta x_2, \dots, x_n + \Delta x_n) \quad (4.2)$$

Let  $\Delta R$  be the uncertainty in the result and  $\Delta x_1, \Delta x_2, \dots, \Delta x_n$  be the uncertainties in the independent variables, then the uncertainty in the result is given by:

$$\Delta R = \sqrt{\left(\frac{\partial R}{\partial x_1} \Delta x_1\right)^2 + \left(\frac{\partial R}{\partial x_2} \Delta x_2\right)^2 + \dots + \left(\frac{\partial R}{\partial x_n} \Delta x_n\right)^2} \quad (4.3)$$

Applying the equation reported above, it is possible to estimate the global uncertainties of the mass flow and heat transfer coefficient measurements.

As regards the mass flow rate, this was measured with an orifice, therefore, the global uncertainty is mainly given by the combination of the uncertainty in the primary measurement of the relative pressure and temperature. Global measurement uncertainty was found to lie between  $\varepsilon_m = 2 - 4\%$ .

As regards the heat transfer coefficient, the global uncertainty  $\Delta HTC$  can be expressed as:

$$\Delta HTC = f(\Delta T_f, \Delta T_{TLC}, \Delta T_0, \Delta t_{event}, \Delta \rho c_p k) \quad (4.4)$$

where  $\Delta T_{TLC}$  is the uncertainty of the TLC green peak temperature related to their calibration,  $\Delta t_{event}$  the uncertainty on the detection of the event time of the TLC, and  $\Delta \rho c_p k$  the uncertainty on the material properties. This latter parameter is estimated around 5% by Camci [58]. Applying equation 4.3 to the HTC contour plots, it is possible to obtain uncertainty maps expressed

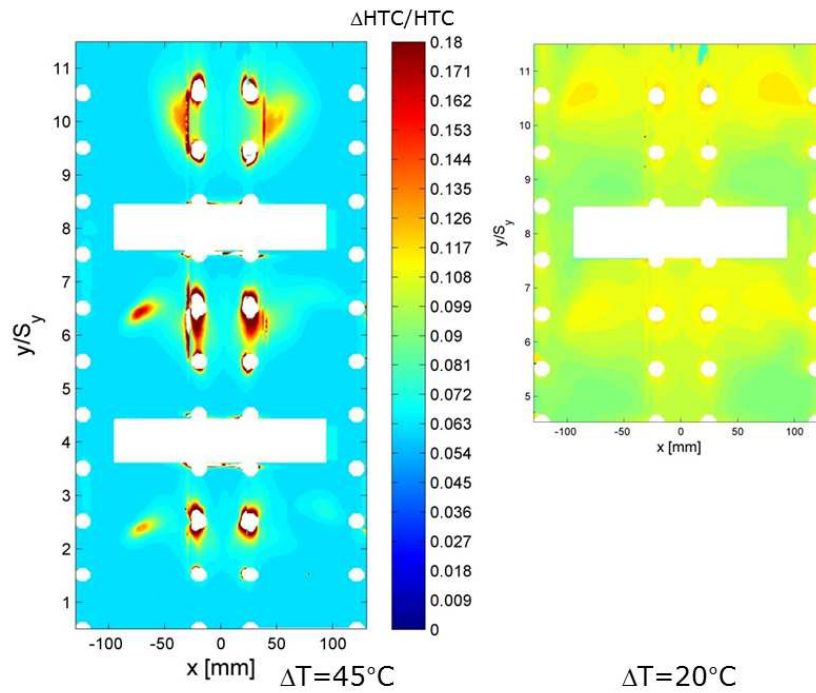


**Figure 4.20:** Uncertainty maps for AVIO C3 measurements

in terms of  $\Delta HTC/HTC$ , as shown in Fig. 4.20 for AVIO C3 measurements. The examples reported in Fig. 4.20 show well how the transient technique is dependent on the selection of the flow temperature. In the map on the left, a temperature difference between the initial conditions and the flow temperature regime conditions of  $\Delta T = 45^\circ\text{C}$  leads to measurement uncertainty higher than 18% due to very low event times in points with higher heat transfer coefficients, i.e. jet stagnation regions and SH extraction. Such uncertainty can be reduced imposing a lower  $\Delta T$ , as shown in the map on the right. In this case, the uncertainty is quite constant along the tested area with values comprised between 8% and 11%. If in the first case the error in the TLC event time detection has a higher influence on the global uncertainty, in the second case the uncertainty is mainly driven by an error in the fluid temperature measurement.

Thus, the uncertainty of the heat transfer coefficient measurements needs to be evaluated case by case depending on the weight of the primary parameters, in particular fluid temperature variation and local event time.

# Experimental Results





# Chapter 5

## Baseline Geometries

The final aim of the present work is to measure the convective heat transfer on the internal surface of different leading edge cooling systems. The present chapter will show all the experimental findings obtained based on the AVIO and ALSTOM baseline geometries. These results have provided the guidelines to select the optimized geometries, illustrated in Chapter 6. Results are reported in terms of two-dimensional contours, stream and tangential averaged values and spatially averaged Nusselt numbers.

### 5.1 Heat Transfer Results on AVIO Geometries

As already described in section 4.2.1, three different AVIO leading edge cooling systems have been studied named B2, B3 and C3.

#### 5.1.1 B2 Results

Figure 5.1 shows the geometrical characteristics of geometry B2. The model is fed radially from the heater, it enters the feeding channel, and before the air jet flows out from the impingement sheet, a honeycomb is present in the insert to uniform the air jet flow (Fig. 5.1(a)). After the flow impinges on the internal surface of the leading edge cavity, the air is extracted from four arrays of extraction holes, that reproduce the discharge

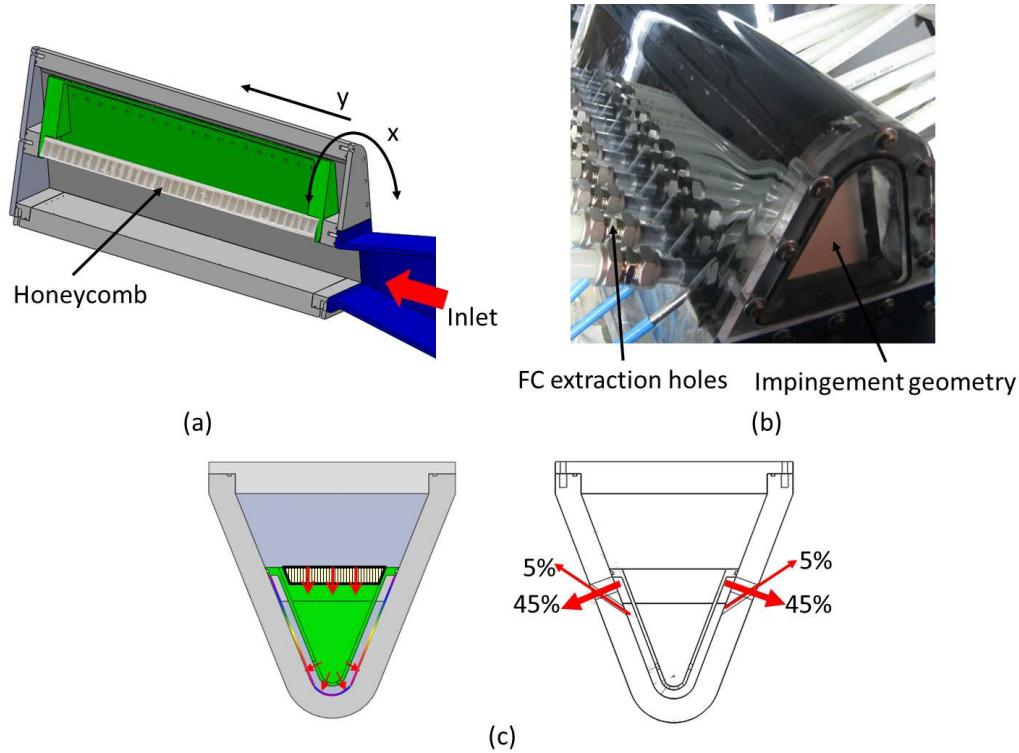


**Figure 5.1:** Details of geometry AVIO B2

of coolant from the film cooling holes. The amount of mass flow extracted has been set with the gate valves in order to draw out 10% from the film cooling holes and the remaining 90% from the auxiliary extraction holes in order to reduce the pressure losses across the extraction lines (Fig. 5.1(b)).

This geometry is characterized by an internal impingement insert with four arrays of circular impingement jets with a total of 76 holes, as illustrated in Fig. 5.1(c).

A total of five jet Reynolds numbers have been tested:  $Re_j = 5500 - 8250 - 11000 - 16500 - 22000$ .

Figure 5.2 shows the  $Nu/Nu_0$  maps for the tested jet Reynolds numbers, where  $Nu_0$  represents the spatially averaged Nusselt number calculated at  $Re_j = 5500$ .

The most interesting result, as expected, is the strong dependence of the Nusselt number on the jet Reynolds number. An increase in the  $Re_j$  leads to an increase in the Nusselt number in terms of peak intensity and its

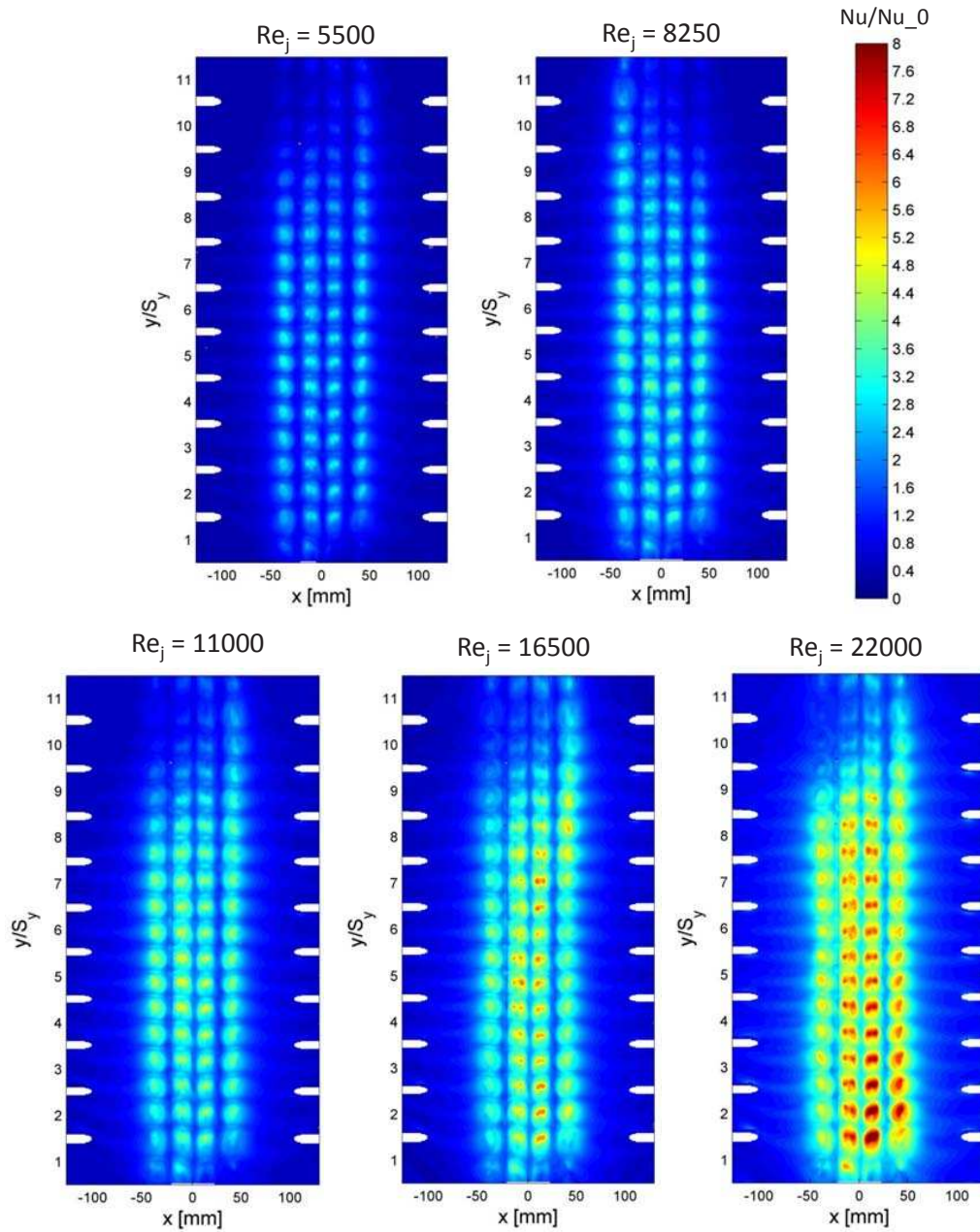
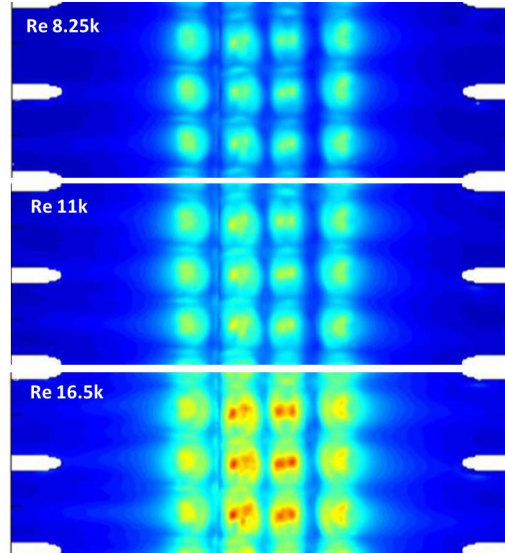


Figure 5.2: AVIO B2  $Nu/Nu_0$  contours

distribution.

A detailed view of the Nusselt number contours shows the particular shape of the jet stagnation region, visible at all the tested jet Reynolds numbers (Fig. 5.3), in particular, in the central curved region. This finding



**Figure 5.3:** AVIO B2  $Nu/Nu_0$  contours: detailed results

can be due to several aspects that need to be considered.

As visible by Fig. 5.3, the Nusselt number maximum is completely offset from the true stagnation point (center of the jet hole), meaning the highest heat transfer occurs outside the stagnation region, typical of the low jet-to-target surface distance  $Z/d_j = 1.57$ . Two near identical regions on either side of the stagnation line represent the maximum Nusselt number. Although a different flow arrangement and internal impingement geometry, similar results have been found by Wright et al. [13].

The curvature of the target surface promotes the flow acceleration and increases the mixing, leading to more pronounced offset maximums. On the other hand, the extraction only from the film cooling holes guarantees a favourable pressure gradient also along the lateral walls of the leading edge. Moreover, the inlet flow arrangement from the feeding channel also induces a pre-rotation on the inlet flow leading to the formation of kidney shape flow structures at the exit of the impingement jets. In any case, these aspects should be analyzed more in depth by means of numerical analysis to better understand the flow interactions inside the cavity.

Averaged Nusselt number values are shown in Figs. 5.4 and 5.5. As

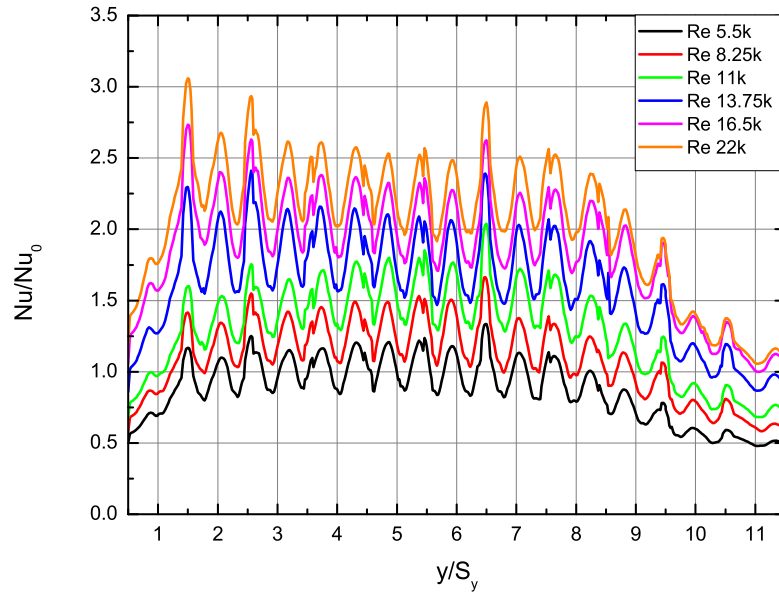


Figure 5.4: AVIO B2  $Nu/Nu_0$  radial averaged values

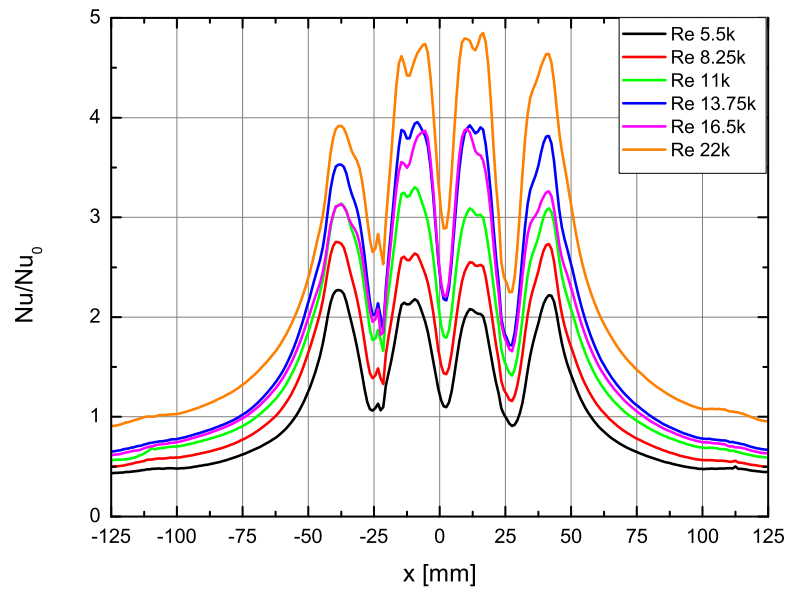


Figure 5.5: AVIO B2  $Nu/Nu_0$  tangential averaged values

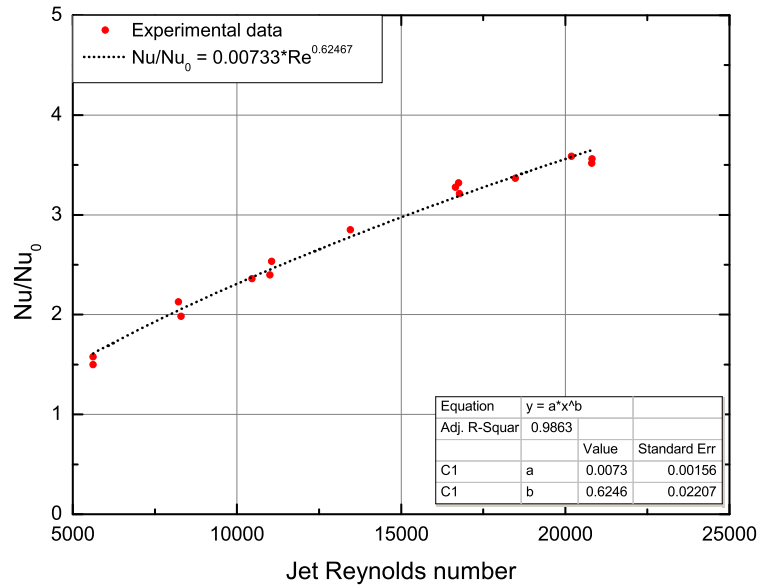


Figure 5.6: AVIO B2  $Nu/Nu_0$  spatially averaged values

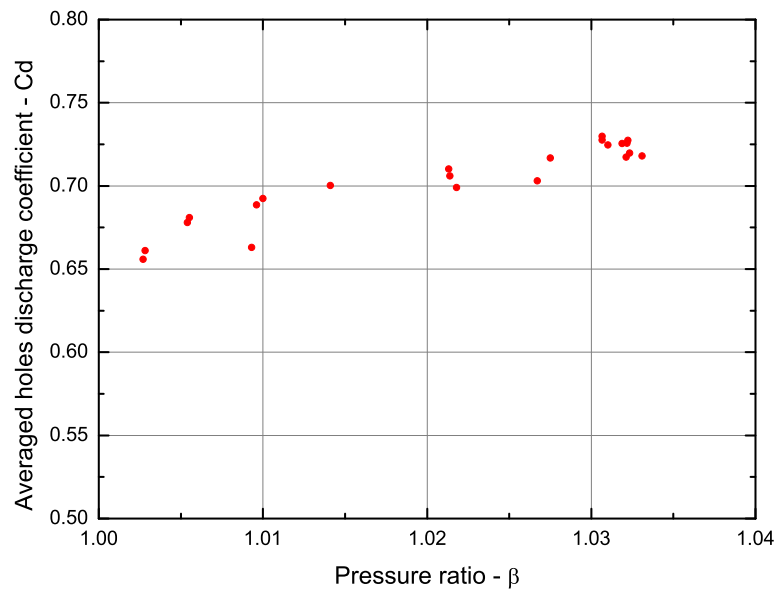


Figure 5.7: AVIO B2 holes discharge coefficient

already pointed out by the two-dimensional contours, the most interesting result is the strong dependence of the Nusselt number on the jet Reynolds numbers.

Tangential averaged values are evaluated considering the central region of the model (i.e.  $3 < y/S_y < 7$ ) which does not take into account the spurious effects due to the model edges. The plot shows symmetrical peaks at lower jet Reynolds numbers, whereas when increasing the jet Reynolds number, higher Nu values were found on the central curved region. Bearing in mind that the whole mass flow is extracted from the film cooling holes, asymmetric results at higher jet Reynolds numbers can be accounted for by the influence of the extraction on the impingement jets. In fact, when looking at the detailed view of the Nusselt contours in Fig. 5.3, the shape of the stagnation region of the lateral jets changes from almost circular to a lengthened imprint.

Figure 5.6 shows the trend of the spatially averaged Nusselt numbers at all the tested jet Reynolds numbers. Looking at the constant and the exponent of the power law used to fit the experimental data, they are consistent with the data found in the open literature on similar impingement cooling systems.

Finally, Fig. 5.7 reports the averaged discharge coefficient measured during the tests by means of four pressure taps located at the hub and at the tip of the model.

### 5.1.2 B3 Results

Figure 5.8 shows the detailed geometrical characteristics of geometry B3. The flow enters directly into the leading edge cavity, part of the flow impinges on the internal surface of the leading edge by means of the impingement geometry, and the remaining part is extracted at the tip of the test rig. Varying the ratio between the impingement flow and the extracted flow at the tip, it is possible to reproduce the different crossflow conditions of the hub, mid-span and tip of the blade.

The impingement geometry is characterized by four arrays of circular impingement jets, with a total of 60 holes, located in a non-symmetric location along the curvilinear abscissa.

A total of five jet Reynolds numbers and three different internal crossflow

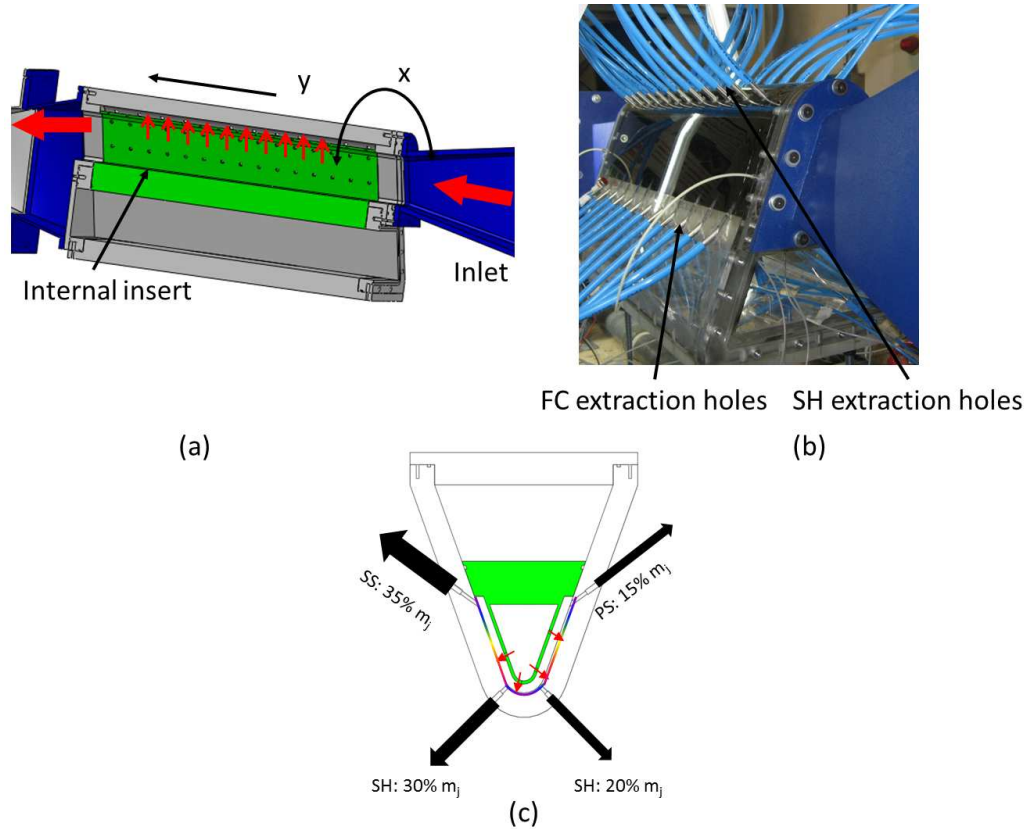


**Figure 5.8:** Details of geometry AVIO B3

conditions have been tested:  $Re_j = 4000 - 7250 - 8500 - 10500 - 17000$ , % Cr = 10 - 40 - 70. Results are expressed in terms of  $Nu/Nu_0$  2D contours, where  $Nu_0$  is the spatially averaged Nusselt number calculated at  $Re_j = 4000$ .

Figures 5.9 and 5.10 report all the 2D Nusselt number contours, in particular, when moving from left to right there is an increase in the jet Reynolds number while when moving from the bottom to the top the crossflow conditions change from 70%, that reproduces the crossflow condition in the hub of the blade, to 10% representative of the tip.

Maps clearly show the increase in the Nusselt number with an increase in the jet Reynolds number. Moreover, the effect of a different crossflow condition inside the leading edge cavity seems not to have any influence on the jet stagnation region shape and on the peak's intensity. Moreover, the presence of the shower-head extraction does not affect the Nusselt number



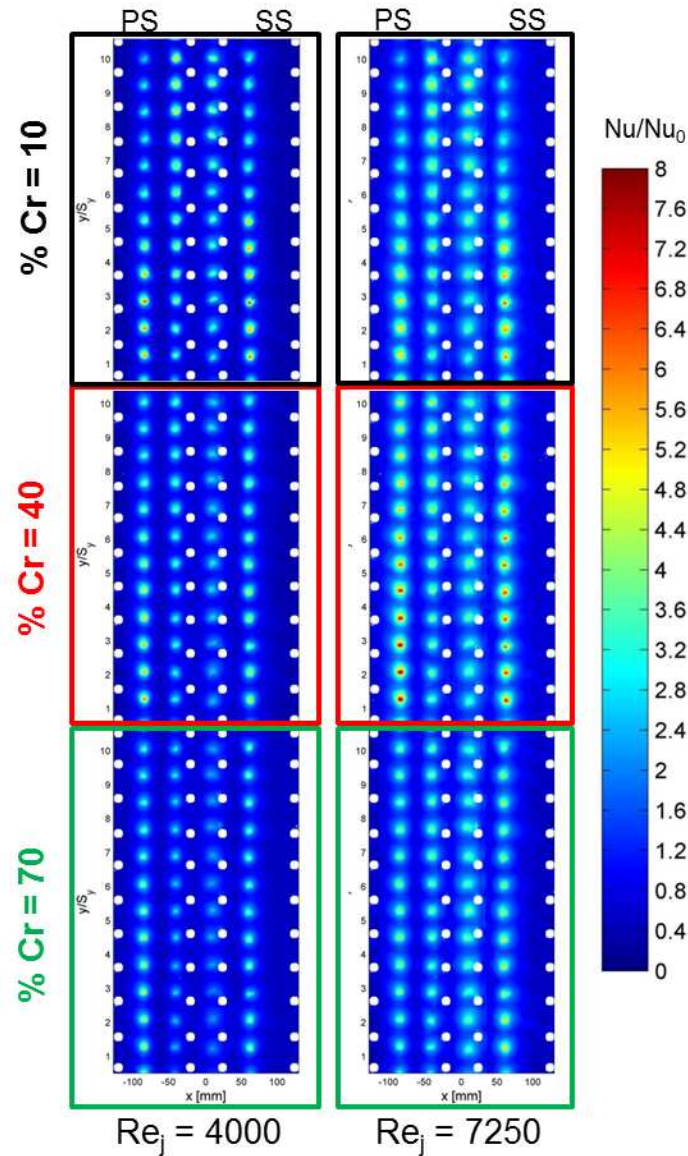
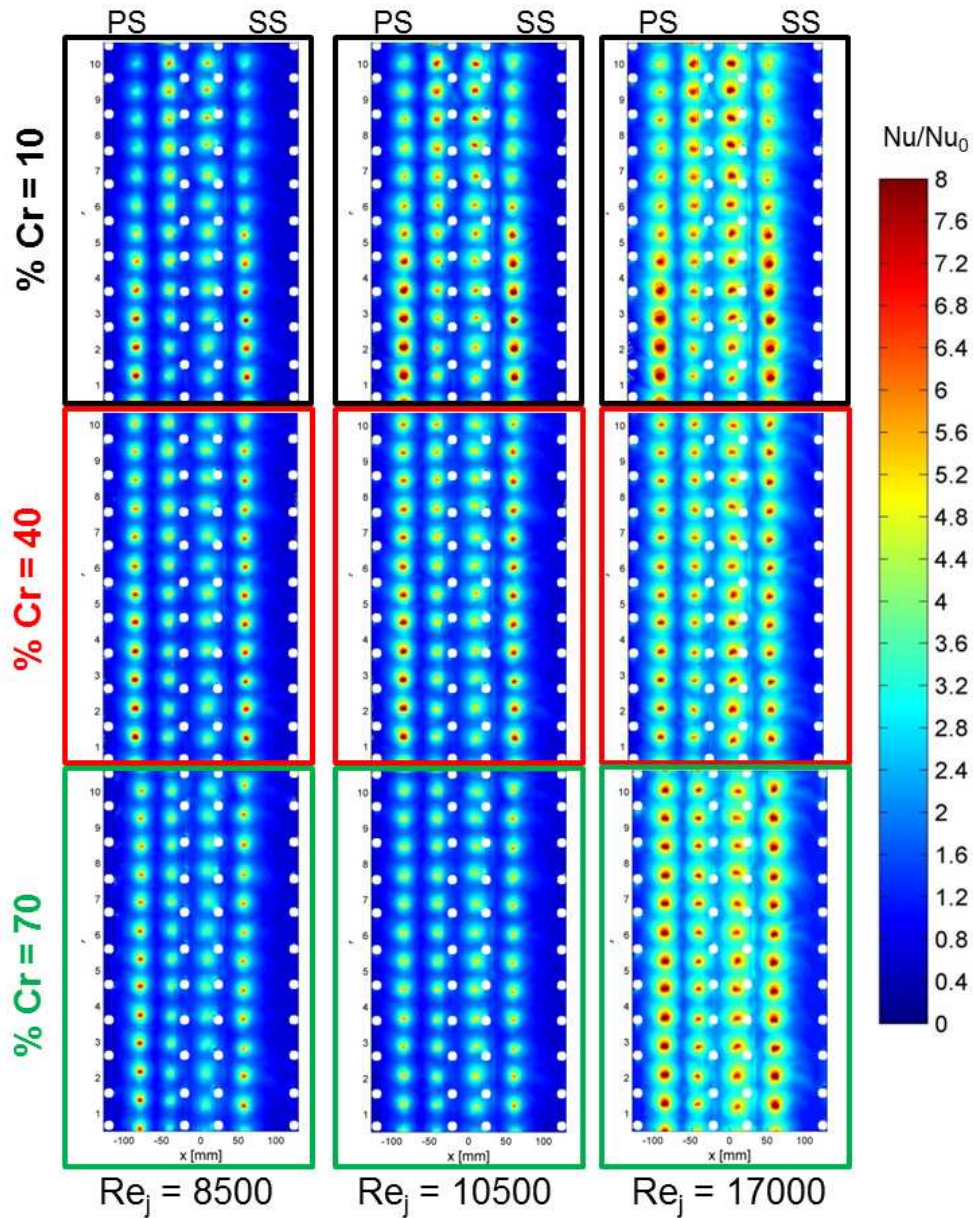


Figure 5.9: AVIO B3  $Nu/Nu_0$  contours, lower  $Re_j$

distribution. This result can be justified by the low jet-to-target surface distance  $Z/d_j$  that is less than 2.

Differently to the results found in geometry B2, in this case heat transfer coefficient peaks are aligned with the center of the jets, resulting in a circular shape of the stagnation region of the jets. This difference is due to the



**Figure 5.10:** AVIO B3  $Nu/Nu_0$  contours, higher  $Re_j$

different inlet flow arrangement between the two geometries.

Averaged Nusselt number values are reported in Figs. 5.11 and 5.12 for 40% of the crossflow condition. As already seen in the 2D contours, the main result is the strong dependence of the Nusselt number on the jet Reynolds

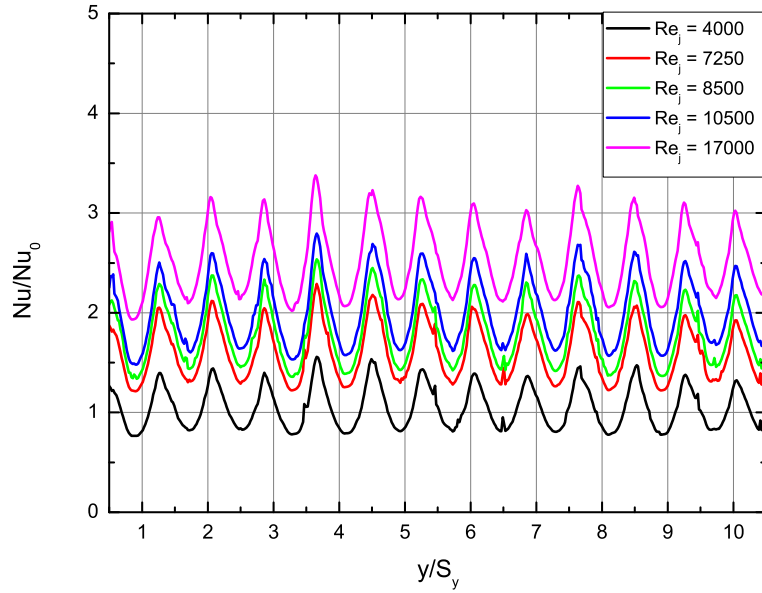


Figure 5.11: AVIO B3  $Nu/Nu_0$  radial averaged values at % Cr = 40

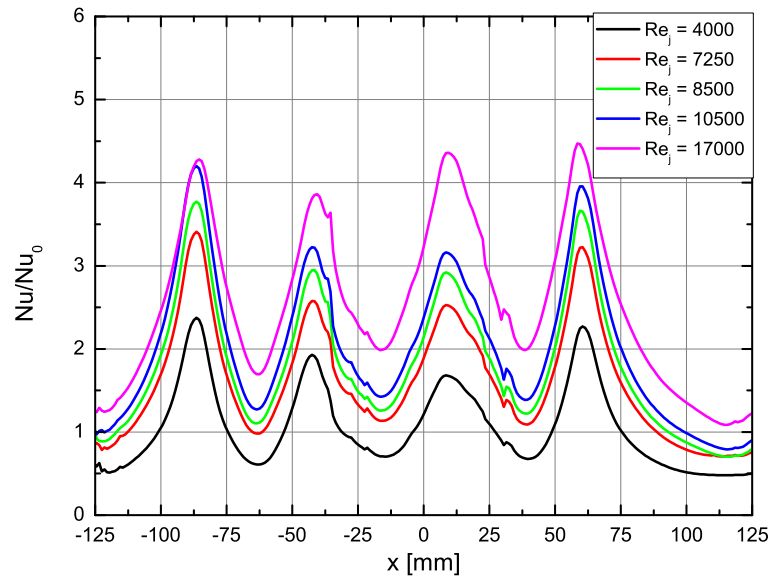
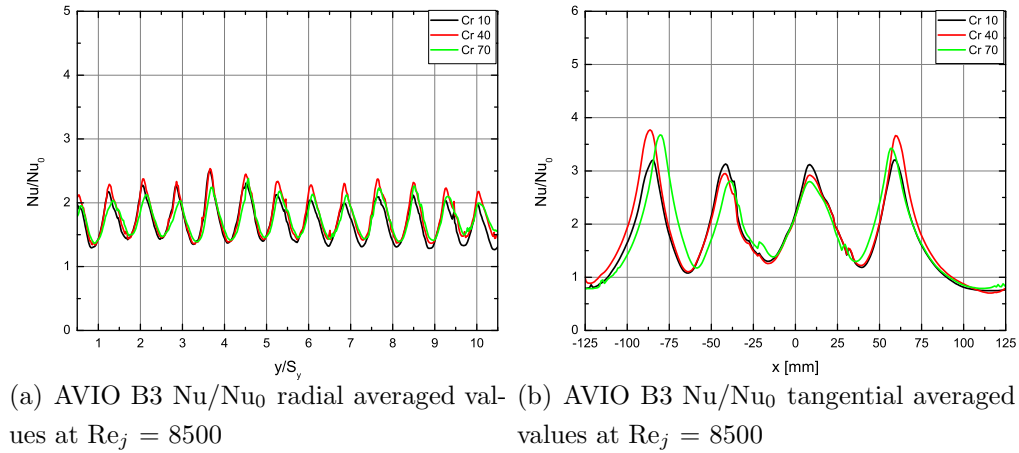
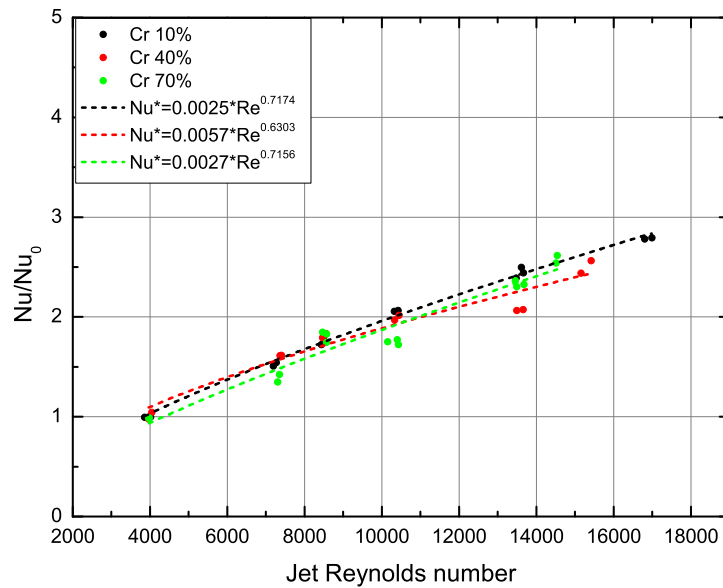


Figure 5.12: AVIO B3  $Nu/Nu_0$  tangential averaged values at % Cr = 40



**Figure 5.13:** AVIO B3  $Nu/Nu_0$  averaged values: effect of % Cr



**Figure 5.14:** AVIO B3  $Nu/Nu_0$  spatially averaged values

numbers. The plots show symmetrical peaks both in radial and tangential directions. Figure 5.13 compares the radial and tangential averaged values for the three different crossflow conditions. Graphs clearly show the negligible influence of a different feeding condition on the Nusselt number.

Figure 5.14 reports the trend of the spatially averaged Nusselt numbers at all the tested jet Reynolds numbers. This plot also confirms the independence of the found Nusselt number results on the different crossflow conditions. Looking at the constant and the exponent of the power law used to fit the experimental data, they are consistent with the data found in the open literature on similar impingement cooling systems.

Finally, Fig. 5.15 shows the averaged discharge coefficient ( $C_d$ ) measured during the tests by means of four pressure taps located at the hub and at the tip of the model.

Unlike the heat transfer results, in this case the holes discharge coefficient is strongly affected by a different feeding condition. In particular, a higher discharge coefficient has been found at % Cr = 10, due to a higher ratio between the jet momentum and the internal crossflow momentum ([62], [63]).

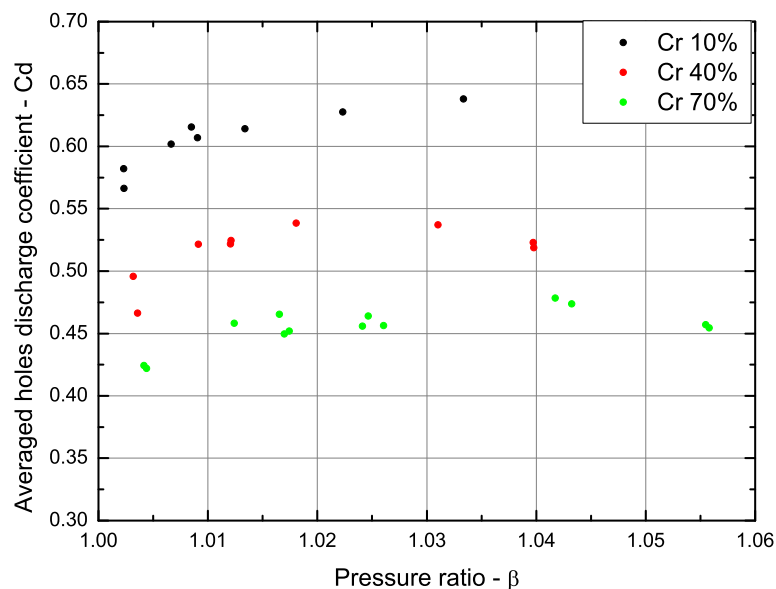


**Figure 5.15:** AVIO B3 hole discharge coefficient

### 5.1.3 C3 Results

Figure 5.16 reports the main geometrical characteristics of geometry C3. As illustrated in Fig. 5.16(a) the flow enters in a radial direction in the feeding channel of the measurement section. Part of the flow passes through the impingement plate, characterized by three large racetrack holes, while the remaining flow is drawn by large pumps in order to set the desired crossflow conditions ( $\% Cr = 10 - 40 - 70$ ).

Four big fins are glued on the leading edge internal surface, with the aim of confining the impingement jets in order to limit their radial dispersion. The flow in the leading edge cavity is then extracted by means of four arrays of circular holes simulating the shower-head and film cooling extraction (Fig. 5.16(b)). Moreover, measurements are performed imposing a different amount of mass flow extracted from each array of extraction holes to reproduce different pressure levels on the airfoil external walls. In particular, 40% of the total mass flow is extracted from the SS row, 10% from the PS row and 50% from the two arrays of SH holes, as depicted in Fig. 5.16(c).

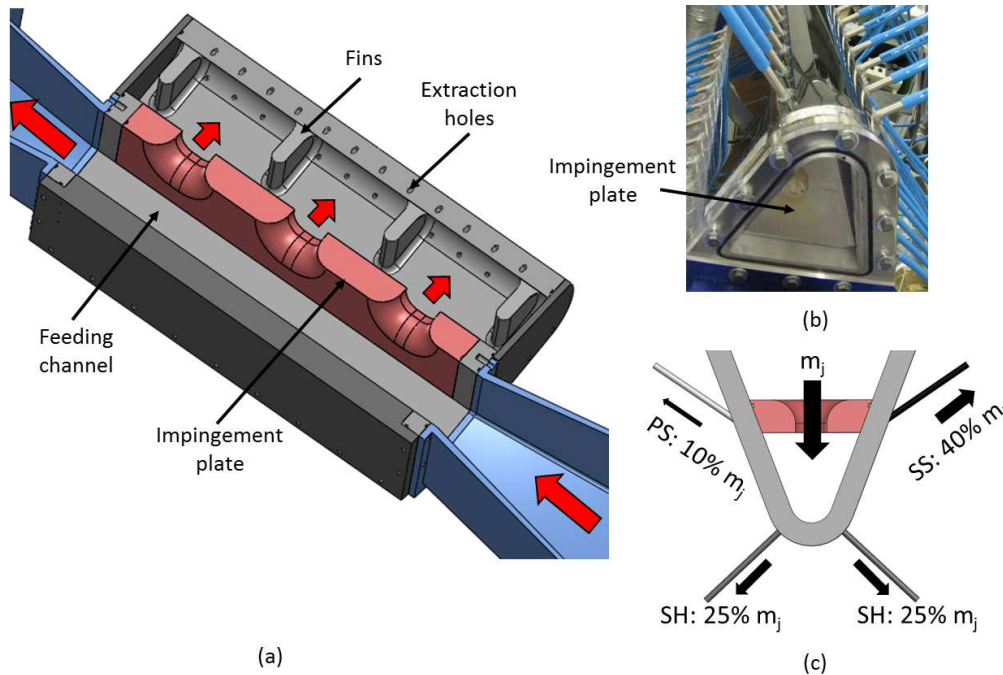


**Figure 5.16:** Details of geometry AVIO C3

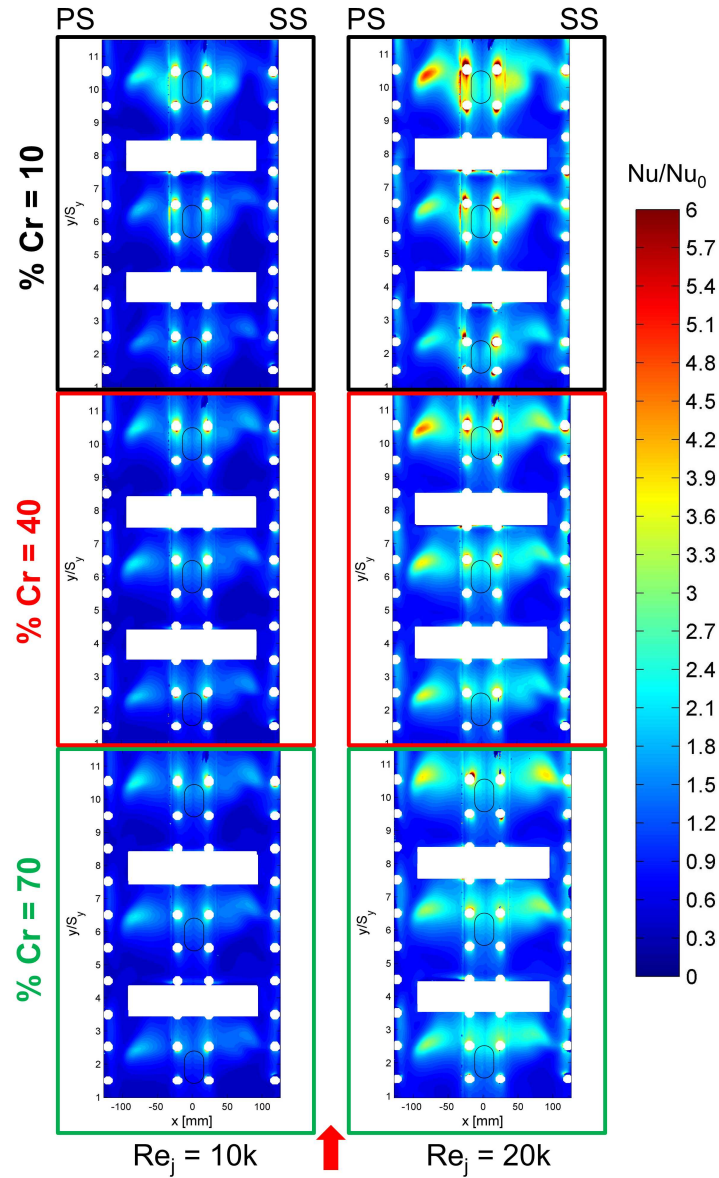


Figure 5.17: AVIO C3  $Nu/Nu_0$  contours, lower  $Re_j$

A total of five jet Reynolds numbers are tested,  $Re_j = 10000 - 20000 - 30000 - 40000 - 50000$ , in three different crossflow conditions in the supply channel,  $\% Cr = 10 - 40 - 70$ . Due to high pressure losses across the extraction lines that have limited the mass flow extracted,  $Re_j = 50000$  has been tested

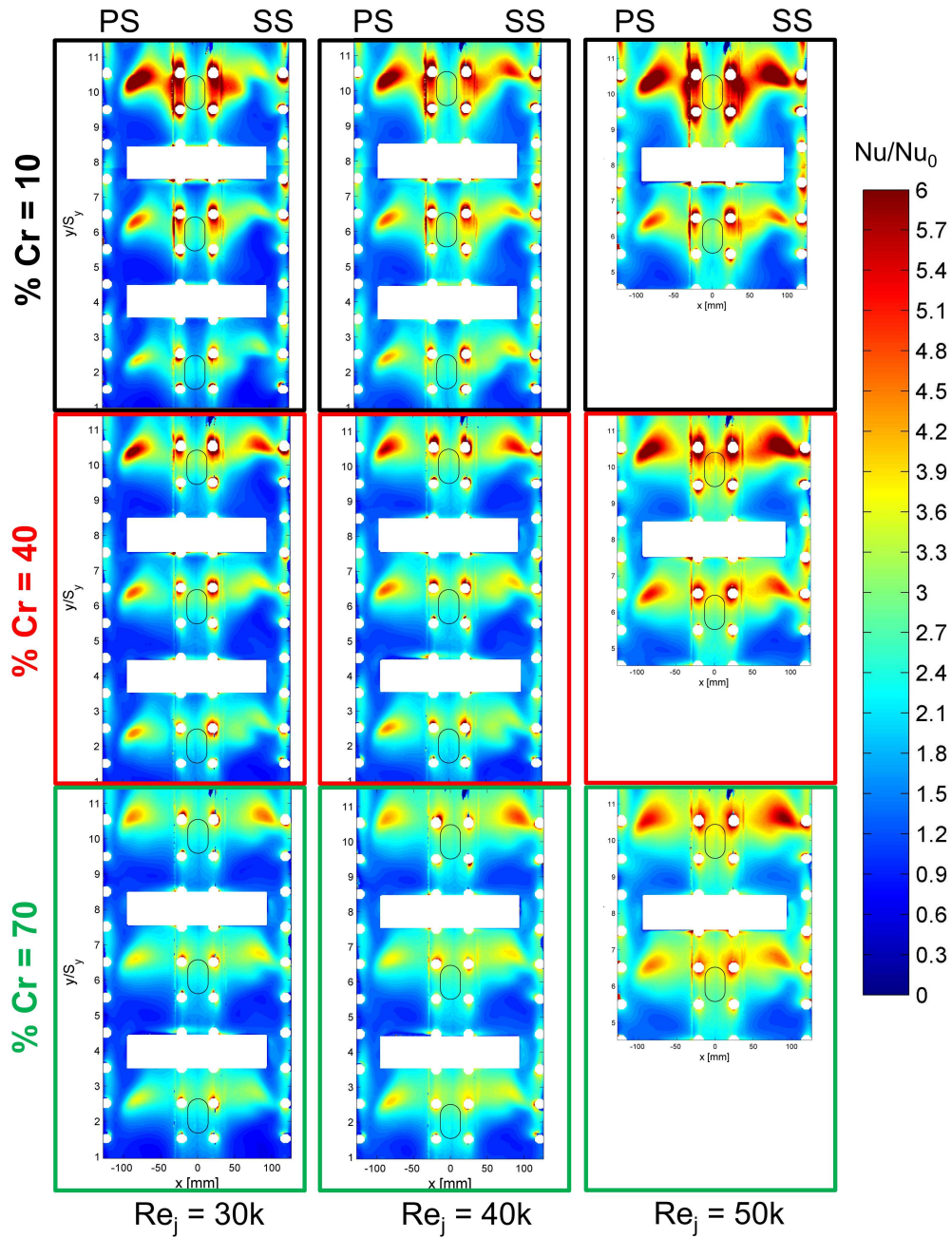


Figure 5.18: AVIO C3  $Nu/Nu_0$  contours, higher  $Re_j$

with only 2 impingement jets.

Figures 5.17 and 5.18 report the experimental non-dimensional Nusselt



number contours at the five tested jet Reynolds numbers. The local distribution of  $Nu$  was normalized with the averaged Nusselt value evaluated at  $Re_j = 10000$  and  $\% Cr = 10$  in order to highlight the Nusselt number variations at higher  $Re_j$  and different  $\% Cr$  conditions. Contour plots related to three crossflow conditions, for each jet Reynolds number, are depicted to give a global overview of the airfoil along the radial direction (from hub to tip). The white rectangles represent the base area of the fins.

For each impingement module delimited by two consequent fins, the Nusselt number peaks are located in four lobes. This evidence could be related to the wedge-shaped leading edge and to the presence of the extraction holes. As discussed before, the test rig is operated in order to set a desired mass flow rate split among the hole arrays. Due to this split, Nusselt number contours appear slightly asymmetric. Higher  $Nu$  peaks are located on the pressure side of the blade. The larger amount of extracted mass flow on the suction side leads to higher  $Nu$  levels close to the film cooling holes. The values of the  $Nu$  peak lobes and their location have been motivated by means of a numerical analysis carried out by Maiuolo et al. [37]. The numerical results presented

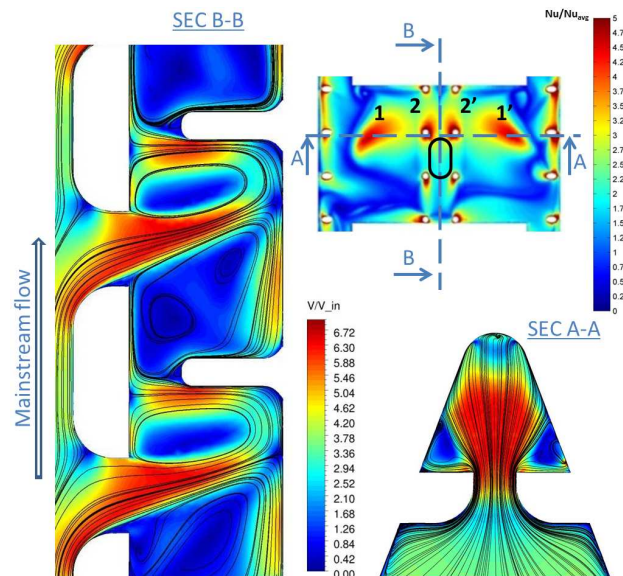


**Figure 5.19:** Central module,  $\% Cr = 40$ : velocity streamlines

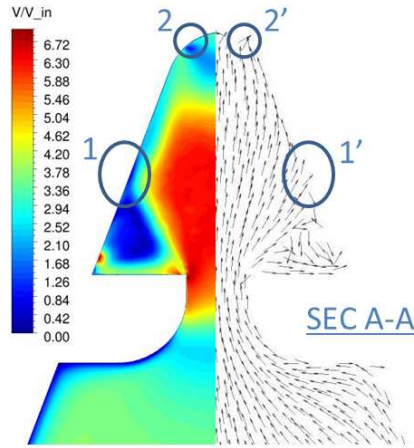


**Figure 5.20:** Central module, % Cr = 40: coolant jet impinging zones

in [37], are only related to the case of  $Re_j = 30000$  in conjunction with the three crossflow conditions. As shown in Fig. 5.19, the lobes are placed downstream of the cold bridge hole center-lines; this evidence could be motivated by observing that these nozzles are not able to completely deflect the coolant jet through the target surface due to their small length-to-diameter ratio  $l/d_h$  (left side of Fig. 5.19).

The pressure gradient related to the wedge-shaped leading edge leads to a relevant coolant jet spreading (right side of Fig. 5.19): that results in the impinging zones labelled as 1 and 1' reported in Fig. 5.20. Approaching the blade leading edge, the coolant flow is finally captured by the shower-head extraction holes. The last evidence motivates the lobes labelled 2 and 2' depicted in Fig. 5.20.

Figures 5.21 and 5.22 show the  $Nu/Nu_0$  averaged values in the radial and tangential direction, for all the tested jet Reynolds numbers, at % Cr = 40. In particular, Fig. 5.22 refers to the central jet that is not affected by possible spurious phenomena due to the model edges.

The plots show a relevant influence of the  $Re_j$  on the heat transfer coefficient. Furthermore, moving from the first impingement module to the last one (Fig. 5.23(a)), which means a different external crossflow condition, the averaged Nusselt number level slightly increases for all the tested conditions. This last

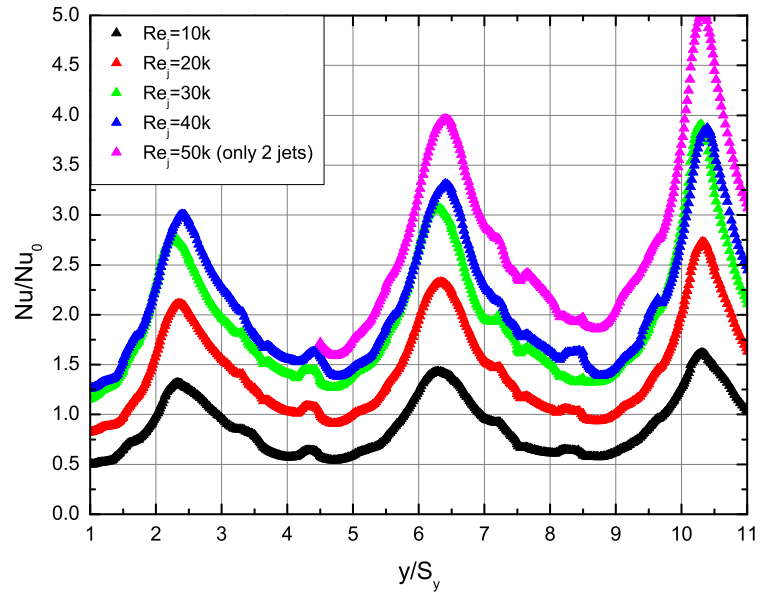


Figure 5.21: AVIO C3  $Nu/Nu_0$  radial averaged values at  $\% Cr = 40$

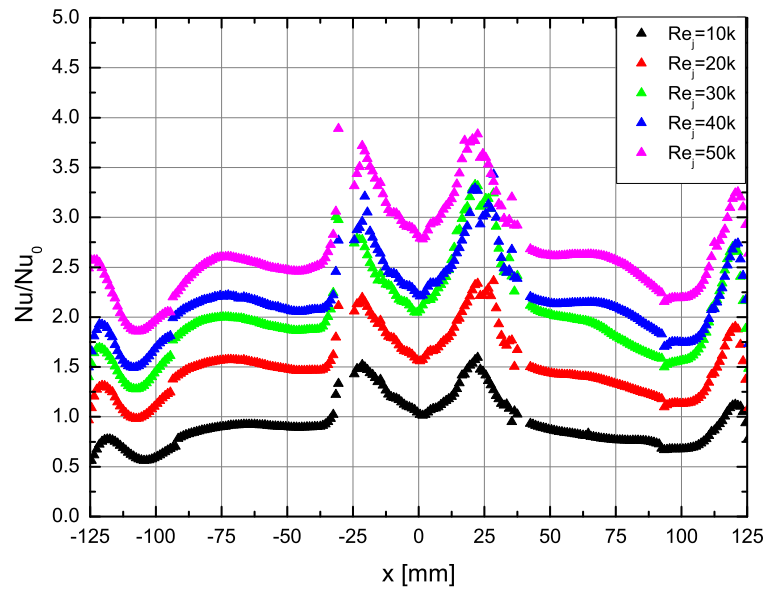
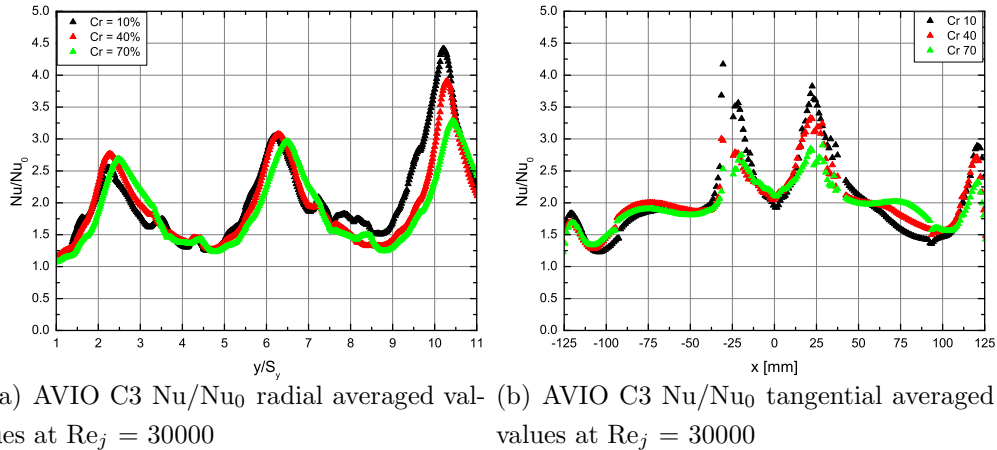


Figure 5.22: AVIO C3  $Nu/Nu_0$  tangential averaged values at  $\% Cr = 40$



**Figure 5.23:** AVIO C3  $Nu/Nu_0$  averaged values: effect of % Cr

evidence could be explained by observing that, as the coolant approaches the blade tip, the jets velocity ratio increases leading to higher heat transfer coefficient peaks, due to the higher discharge coefficient of the jets.

Far away from the region where the coolant jet impinges directly (i.e. moving towards film cooling holes), the averaged radial-wise profiles seem not affected by the % Cr parameter, as illustrated in Fig. 5.23(a). This behaviour can be explained when observing that the mass flow rate extracted by the holes does not change across the rig, as highlighted by the CFD calculations. All the experiments demonstrate that an asymmetric mass flow extraction and variable crossflow conditions slightly influence the Nusselt number.

Finally, Fig. 5.24 presents some comparisons between the present experimental results and data on similar test cases, found in the open literature (Chupp et al. [27] and Taslim et al. [10]). The figure reveals a very good agreement with Chupp et al.'s prediction [27] in all tested operating conditions. On the other hand, Taslim found Nusselt number levels about 30% higher but with a trend similar to the present data.

The revealed discrepancies could be explained by to the differences in the investigated geometries, in terms of  $Z/d_h$ , and different inlet and outlet flow arrangements. Moreover, most of the published data take into account only the nose area, while present averaged data also considers low HTC regions

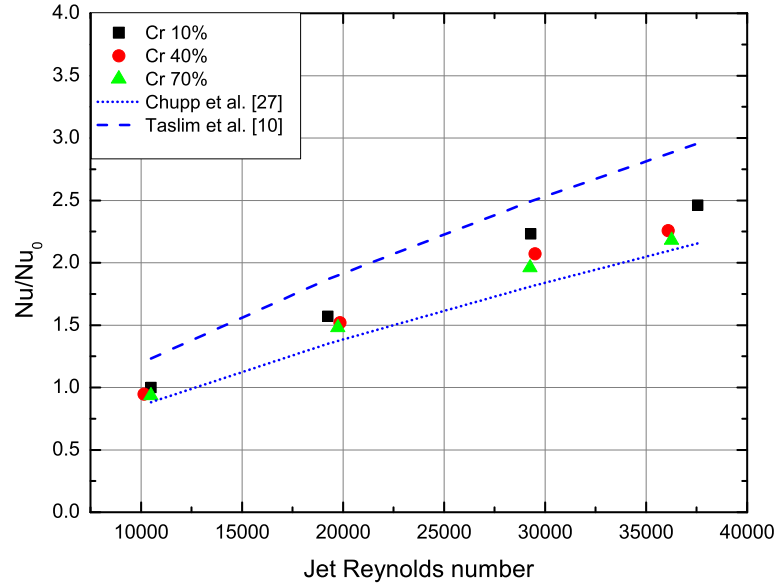


Figure 5.24: AVIO C3  $Nu/Nu_0$  spatially averaged values

on the lateral walls.

## 5.2 Heat Transfer Results on ALSTOM Geometries

As already described in section 4.2.2, two different external geometries have been studied named **LE 1** and **LE 2**. In the next sections, comparisons will be shown to highlight the influence of different leading edge opening angles, shape and number of impingement jets and their pitches along the radial and tangential directions on the heat transfer distribution.

### 5.2.1 Effect of the LE Opening Angle

Figure 5.25 compares the experimental Nusselt number two-dimensional contours of geometry **G1** and **G4**, that share the same internal impingement geometry but with a different leading edge opening angle:  $\vartheta = 70^\circ$  vs  $100^\circ$ .

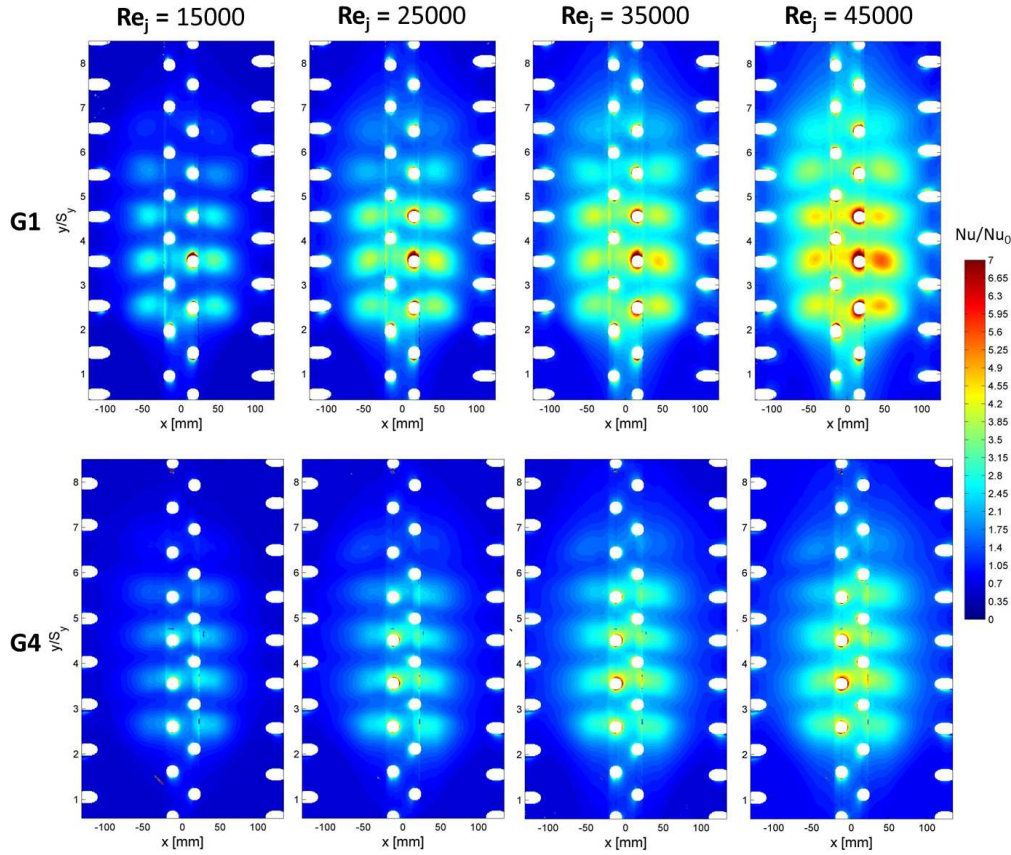


**Figure 5.25:** Effect of the LE opening angle: **G1** vs **G4** contour plots

The difference on the wet internal surface between the two leading edge is negligible.

Results are reported in terms of  $Nu/Nu_0$  where  $Nu_0$  is the spatially averaged Nusselt number found at  $Re_j = 15000$  for geometry **G4**. The internal impingement geometry is characterized by a single array of 5 circular holes.

For each contour plot it is evident that the number of Nusselt peaks is related to the number of impingement jets and the 5 peaks generated by the impingement jets are well defined.

Figures 5.26 and 5.27 show the comparisons in terms of averaged Nusselt number in the radial and tangential direction respectively. To avoid spurious effects due to the model edges, comparisons in the tangential direction have been made considering the surface from  $y/S_y = 3$  to 5.

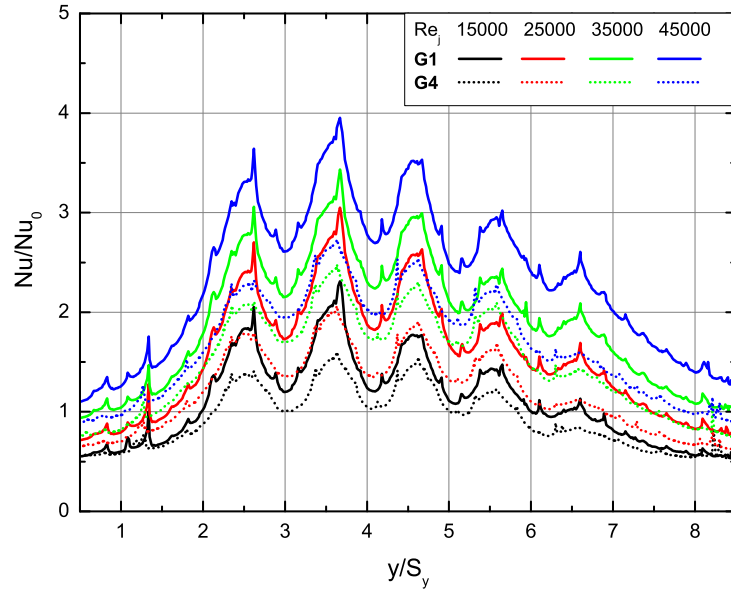


Figure 5.26: Effect of the LE opening angle: **G1** vs **G4** radial averaged values

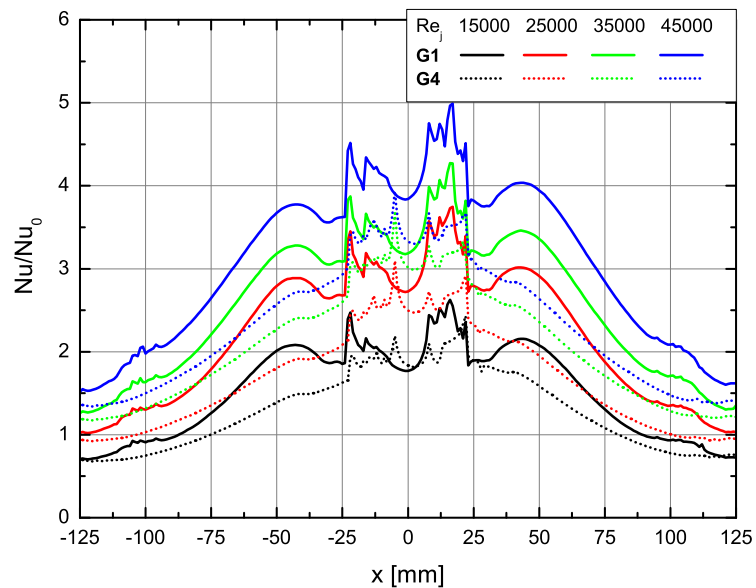
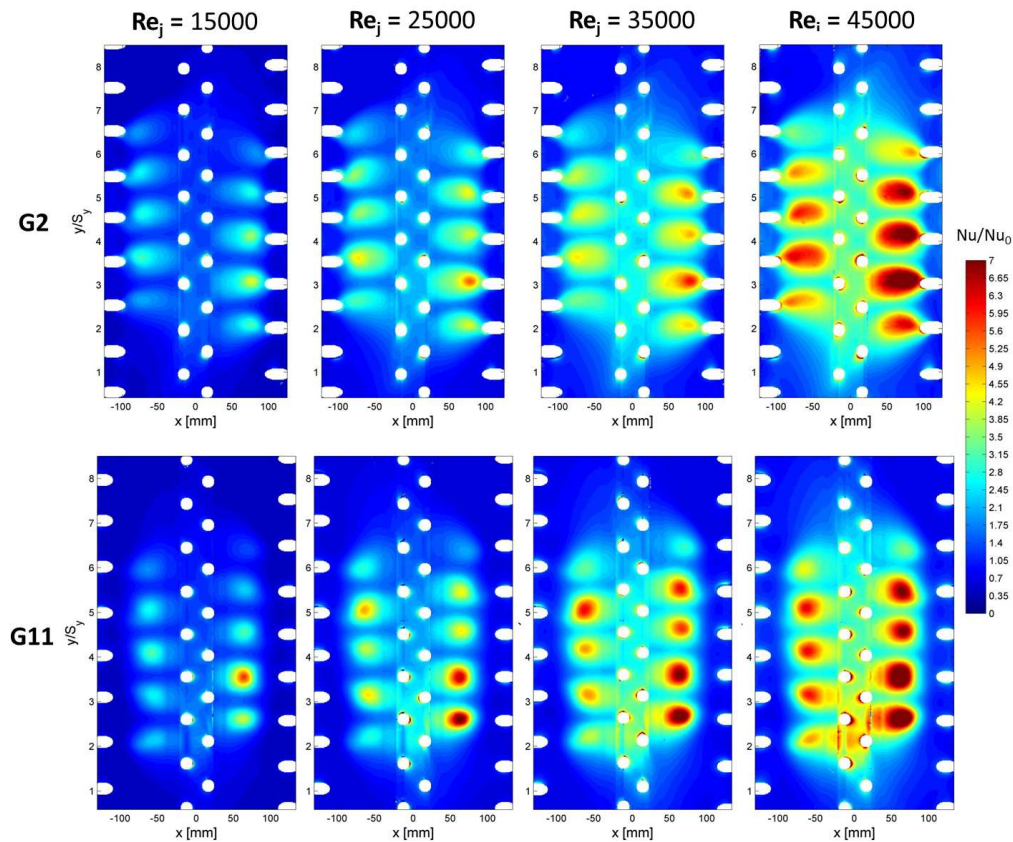


Figure 5.27: Effect of the LE opening angle: **G1** vs **G4** tangential averaged values

The effects of a different leading edge wedge-angle are visible from both the 2D contour plots and in the averaged Nusselt number trends. Noticeable differences have been found by varying the leading edge opening angle, both in the central curved region and on the lateral walls. In particular, higher values of  $Nu/Nu_0$  have been measured at  $\vartheta = 70^\circ$ , especially at higher Reynolds numbers. As can be seen from the tangential averaged values, a lower  $\vartheta$  leads to the formation of Nusselt number peaks on the lateral walls, due to a lower local  $Z/d_j$  and to the impingement jets spreading. Moreover, the extraction from the shower-head and film cooling holes contributes to maintaining a uniform coolant flow distribution over the tested surface. In both cases the correlation strongly underestimates the measured values. The high Nusselt number gradients at  $x = \pm 25$  mm are due to optical aberrations



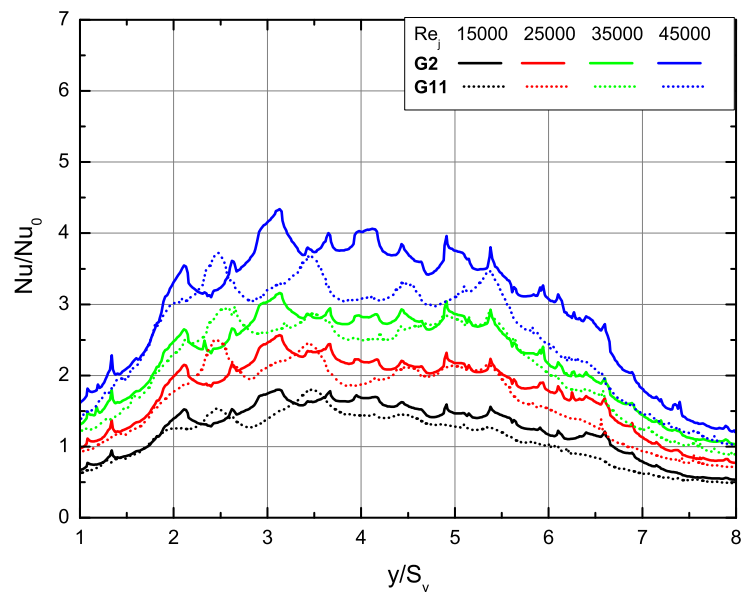
**Figure 5.28:** Effect of the LE opening angle: **G2** vs **G11** contour plots



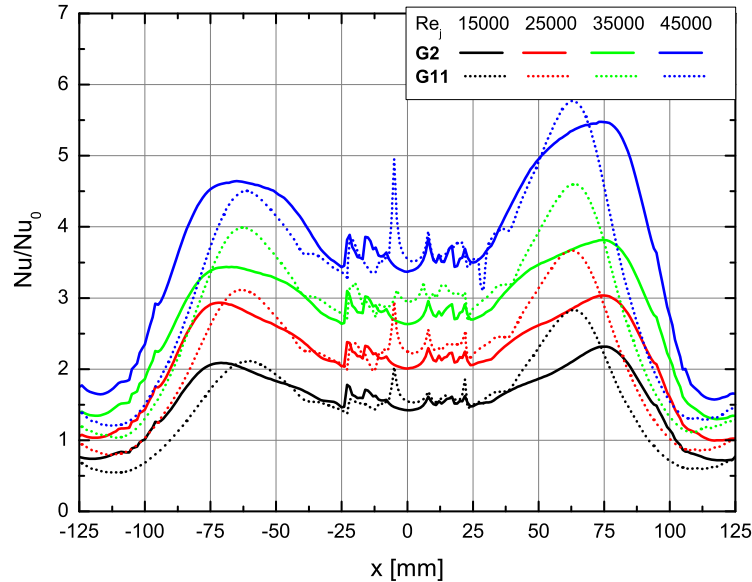
in correspondence to the connection between the central curved region and the lateral walls.

Figure 5.28 shows the comparison between the experimental Nusselt number 2D contours of geometry **G2** and **G11**, that share the same internal impingement geometry but with a different leading edge opening angle:  $\vartheta = 70^\circ$  vs  $100^\circ$ . Results are reported in terms of  $Nu/Nu_0$  where  $Nu_0$  is the spatially averaged Nusselt number found at  $Re_j = 15000$  for geometry **G11**. The internal impingement geometry is characterized by a double array of circular holes.

As for the double array of circular holes (**G2**), Nusselt number contours show the effect of different  $\vartheta$ s on the spatial distribution of the heat transfer coefficient. At  $\vartheta = 100^\circ$  the Nusselt peaks are almost circular, with a slight distortion due to the extraction of the coolant from the shower-head holes. At  $\vartheta = 70^\circ$  the effect of film cooling extraction is visible on the lateral walls leading to a lengthening of the jet stagnation region that increases the area subjected to heat transfer enhancement. The presence of the shower-head



**Figure 5.29:** Effect of the LE opening angle: **G2** vs **G11** radial averaged values



**Figure 5.30:** Effect of the LE opening angle: **G2** vs **G11** tangential averaged values

extraction holes guarantees a uniform distribution of the Nusselt number in the central region as well. The averaged Nusselt number shows the same trend found in the contour plots. As shown by the  $Nu/Nu_0$  trends reported in Figure 5.29, no significant differences can be found along the streamwise abscissa between the two test cases, mainly due to the presence of the shower-head extraction. This behaviour is also confirmed by looking at the tangential  $Nu/Nu_0$  trends (Figure 5.30). On the lateral walls higher peaks of Nusselt numbers are found at  $\vartheta = 100^\circ$  in correspondence to the stagnation region of the impingement jets. On the contrary, at  $\vartheta = 70^\circ$ , slightly lower Nusselt number peaks are measured, with a shift of the jet stagnation region from  $x = \pm 60$  to  $\pm 75$  mm. In the central region (from  $x = -25$  to  $25$  mm) the same Nusselt values are measured.

Figure 5.31 shows the comparison between the experimental Nusselt number 2D contours of geometry **G3** and **G12**, that share the same internal impingement geometry but with a different leading edge opening angle:  $\vartheta = 70^\circ$  vs  $100^\circ$ . Results are reported in terms of  $Nu/Nu_0$  where  $Nu_0$  is the spatially averaged Nusselt number found at  $Re_j = 15000$  for geometry **G12**.

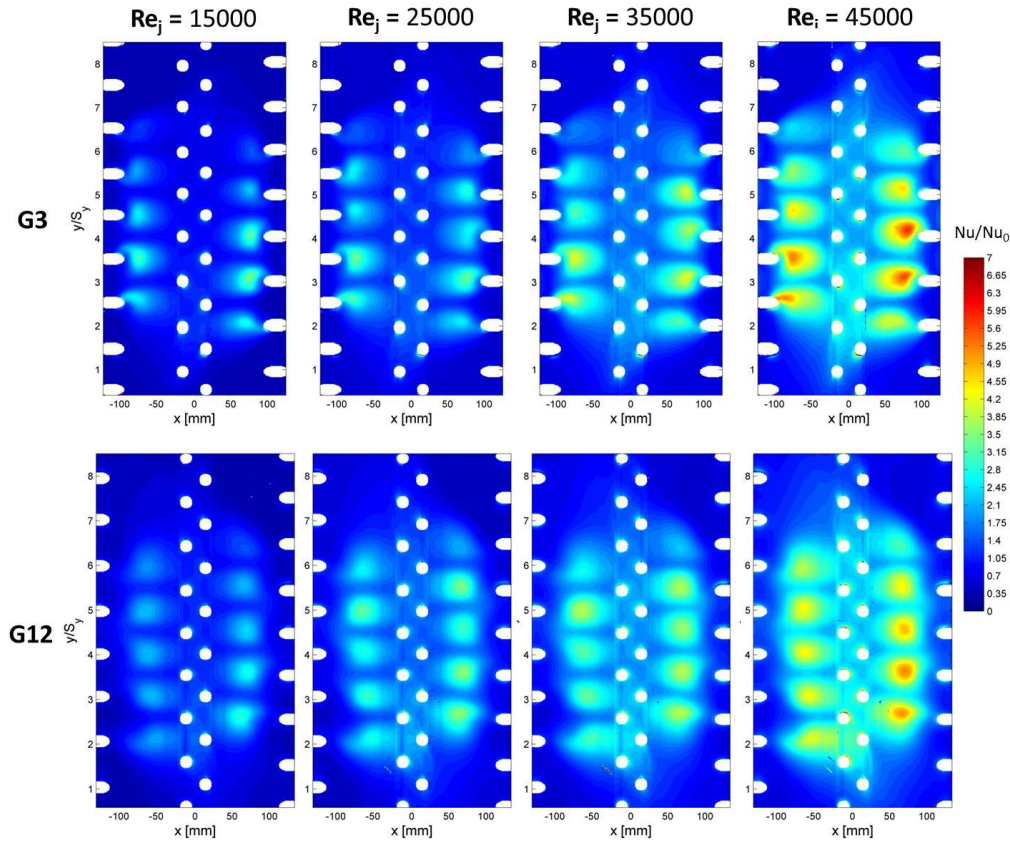


**Figure 5.31:** Effect of the LE opening angle: **G3** vs **G12** contour plots

The internal impingement geometry is characterized by a double array of racetrack holes.

Comparing the two external leading edge geometries with the double array of racetrack holes, it can again be seen that Nusselt number contour plots show once again the influence of the film cooling extraction on the jet stagnation region. The presence of a narrower opening angle combined with the jet spreading moves the jet stagnation region very close to the film cooling holes, thus leading to a distortion of the stagnation region shape. This effect is highlighted also in the tangential averaged values of Fig. 5.33 where slightly lower Nusselt numbers are found in the central region at  $\vartheta = 70^\circ$ . No relevant differences have been measured on the lateral walls, except for a different stagnation point position between the two opening angles  $\vartheta$ .

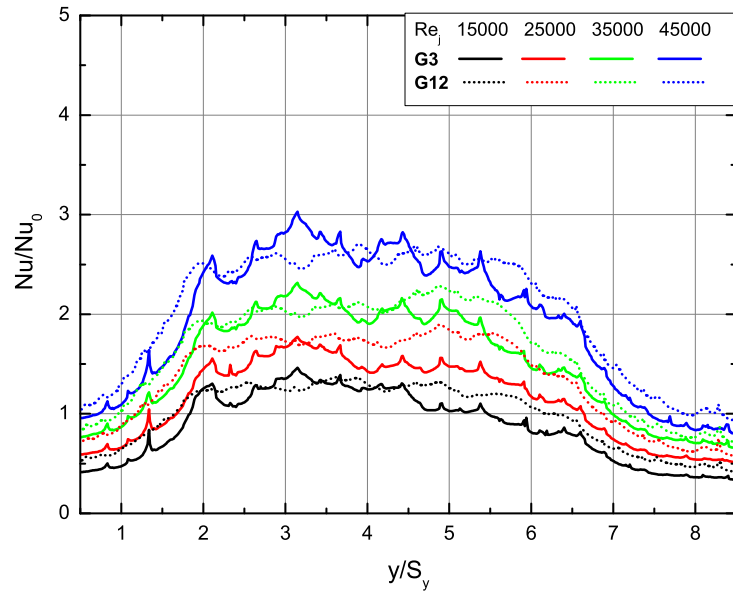


Figure 5.32: Effect of the LE opening angle: **G3** vs **G12** radial averaged values

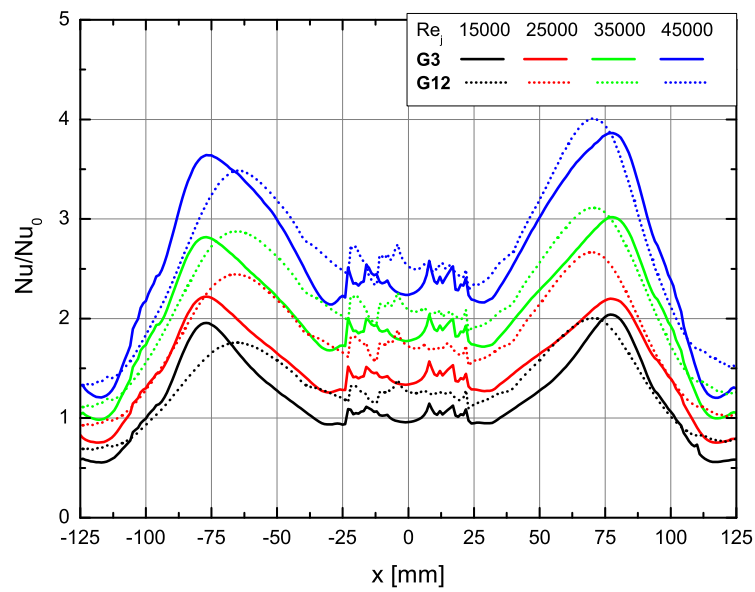
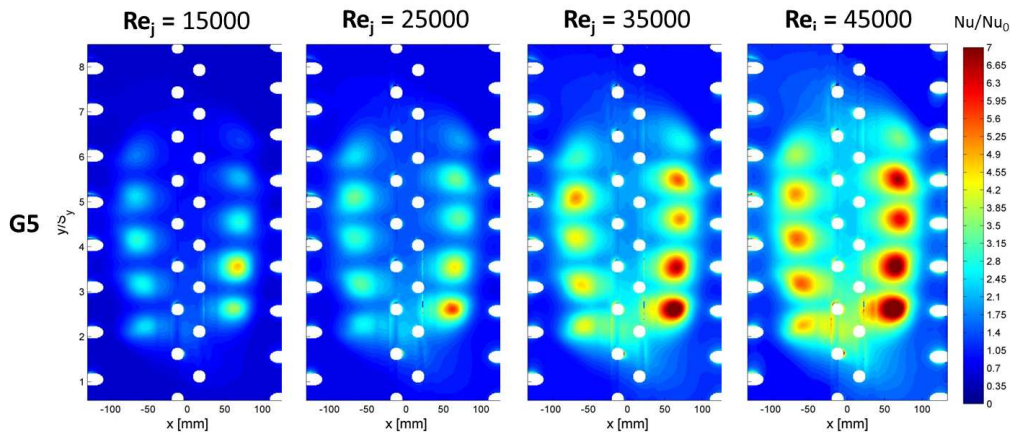


Figure 5.33: Effect of the LE opening angle: **G3** vs **G12** tangential averaged values

To summarize all the experimental results discussed in this section, the Nusselt number found with the single row of circular holes is strongly affected by the leading edge opening angle. As for the internal geometries with a double row of holes (circular and racetrack), a different angle  $\vartheta$  has a predominately local influence on the Nusselt number, thus leading to local distortions and a shift of the jet stagnation region, while global results remain quite similar.

### 5.2.2 Effect of the SH Extraction

Figure 5.34 shows the two-dimensional contours of geometry **G5**, in order to highlight the effect of the coolant extraction from the shower-head holes. Figures 5.35 and 5.36 show the comparison between **G5** and **G11** geometries in terms of averaged Nusselt number in the radial and tangential directions, at all the tested Reynolds numbers.



**Figure 5.34:** ALSTOM contour plots. Effect of the SH extraction

Looking at the maps in Fig. 5.34, the absence of extraction from the SH holes is mainly visible in the central curved region, where lower values of the Nusselt numbers were found, compared to the reference geometry **G11** already shown in Fig. 5.28. However, even if there is no coolant extraction in the central region, Nusselt number values are not as low as they are close to the lateral extraction holes because coolant is naturally directed by the

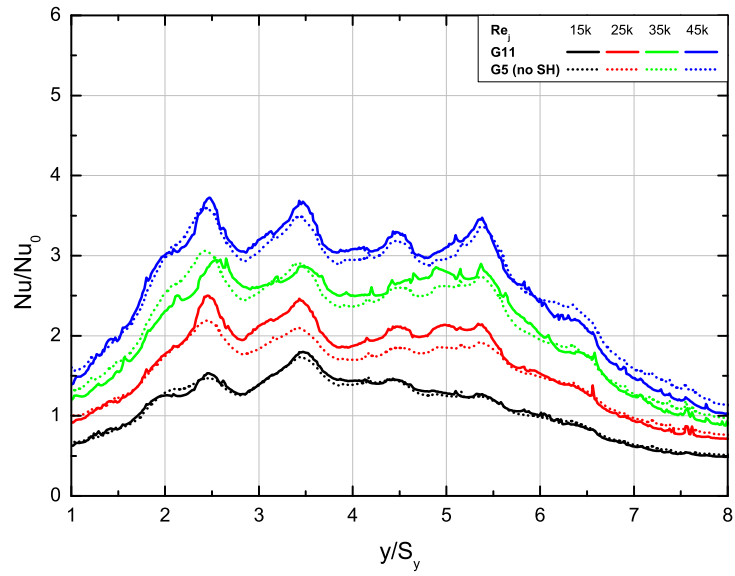


Figure 5.35: Effect of the SH extraction in radial direction: **G5** vs **G11**

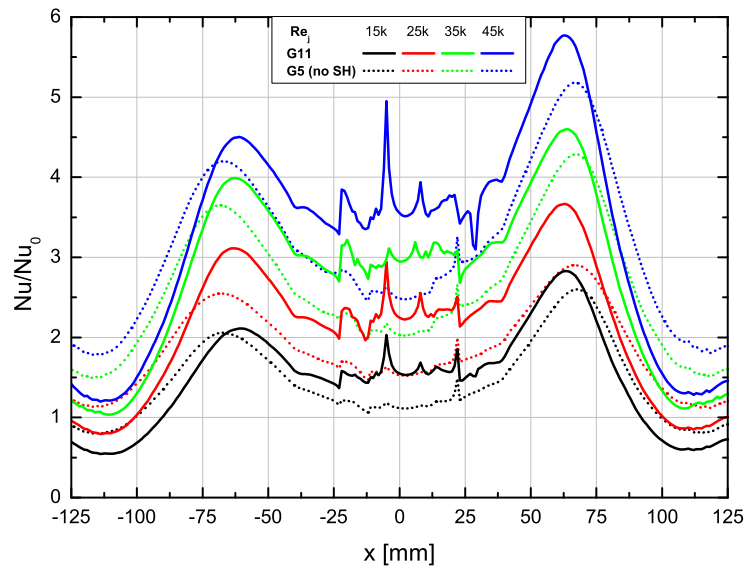


Figure 5.36: Effect of the SH extraction in tangential direction: **G5** vs **G11**

inclined side walls to the central area. On the lateral walls the **G5** and **G11** configurations experience approximately the same values in terms of Nusselt number distribution and peak intensity, while there is a very slight difference in the peak position: with the shower-head, peaks are in fact located at a lower tangential position closer to the SH extraction. This effect is due to the fact that with the shower-head extraction, impingement jets are slightly diverted in the central region.

Averaged Nusselt values confirm what has already been pointed out in the contour plots; in the radial direction, differences are practically negligible and are comparable to experimental uncertainties. In the tangential direction, at all the tested Reynolds numbers, a lower Nusselt number magnitude has been found in the central curved region (from  $x = -25$  to  $+25$  mm) without the SH coolant extraction, while slightly higher values have been found on the lateral walls, in particular near the FC extraction arrays (from  $x = -125$  to  $-75$  mm).

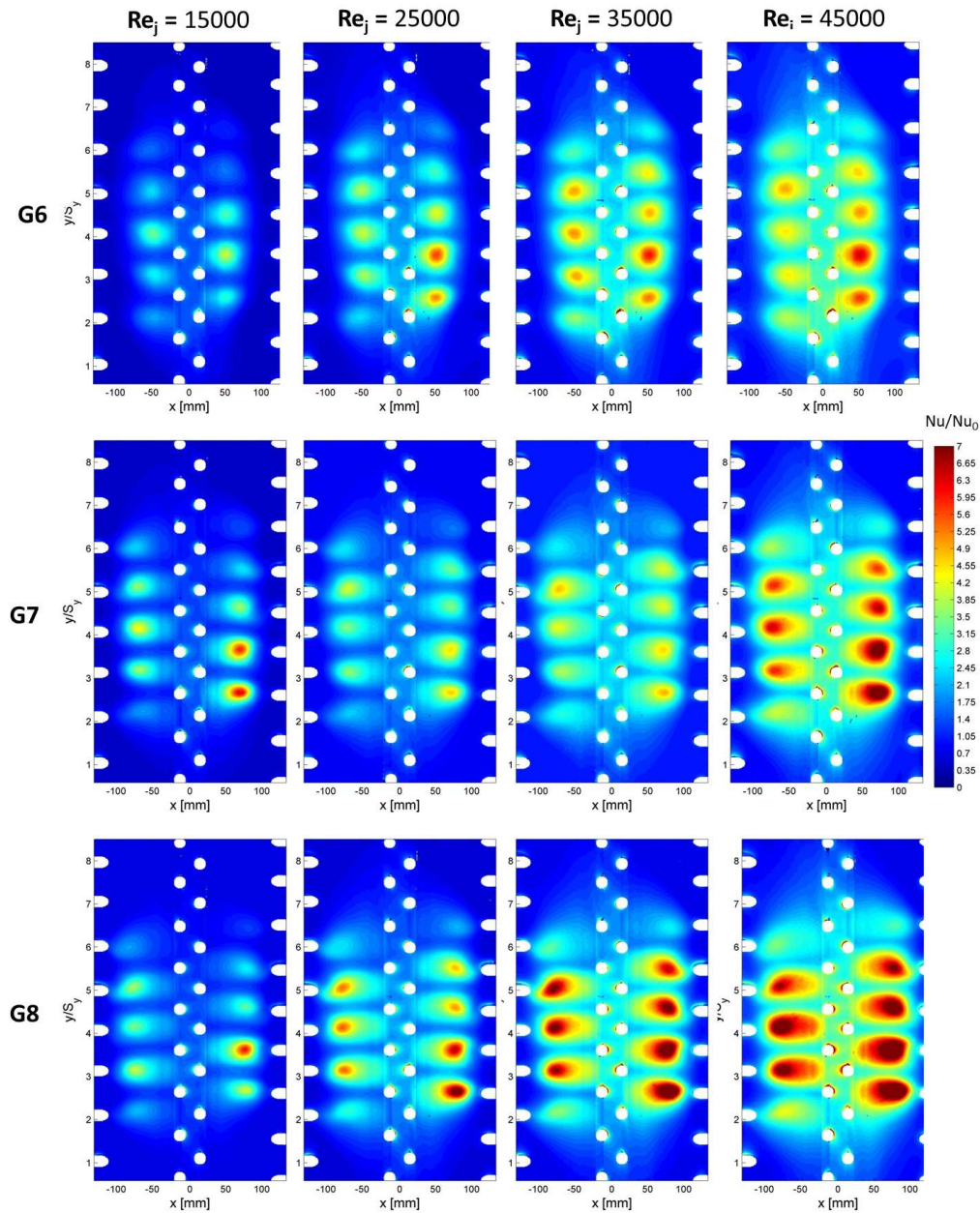
### 5.2.3 Effect of the Tangential Pitch

Figure 5.37 illustrates the comparison between **G6**, **G7** and **G8** geometries in terms of two-dimensional contours, while Figures 5.38 and 5.39 show the averaged Nusselt number in the radial and tangential direction at all tested Reynolds numbers, including also the reference geometry **G11**.

Results clearly highlight the effects of the tangential pitch, both in the Nusselt number distribution and in the intensity of its peaks. The presence of the film cooling and shower-head extraction leads to a lengthening of the jets stagnation area in the lateral regions, moving from nearly circular shapes in **G6** to oblong shapes in **G8**. This effect results in an increased portion of area exposed to heat transfer enhancement, as visible in both radial and tangential averaged values.

In the central curved region, (i.e. from  $x = -25$  to  $+25$  mm) the presence of the shower-head extraction guarantees a nearly constant Nusselt number distribution among all the tested tangential pitches.

As for the peak intensity, the Nusselt number at the stagnation point increases with decreasing jet-to-jet distances, from  $Z/d = 5.95$  of **G6** to  $Z/d$



**Figure 5.37:** ALSTOM contour plots. Effect of the tangential pitch

= 4.53 of **G8**, as found similarly by Vullierme et al. [64] and Liu and Feng [65].

For the configuration considered in the present study, both maps and



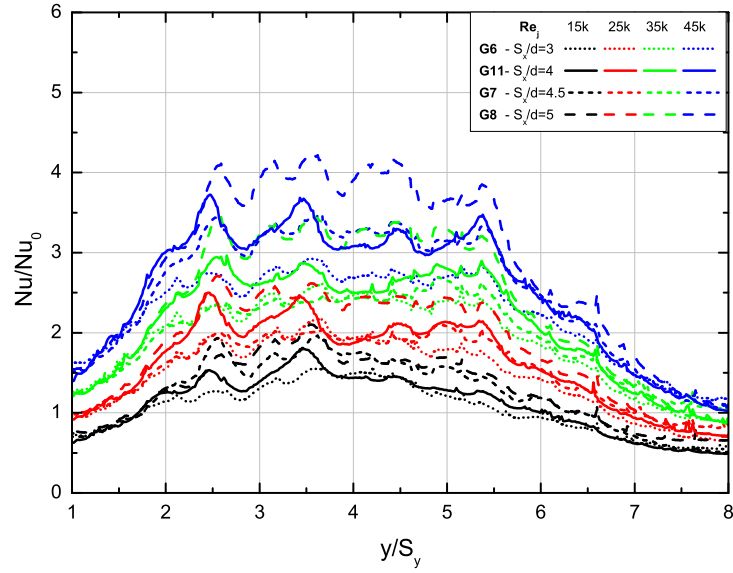


Figure 5.38: Effect of the tangential pitch in radial direction: **G6** vs **G11** vs **G7** vs **G8**

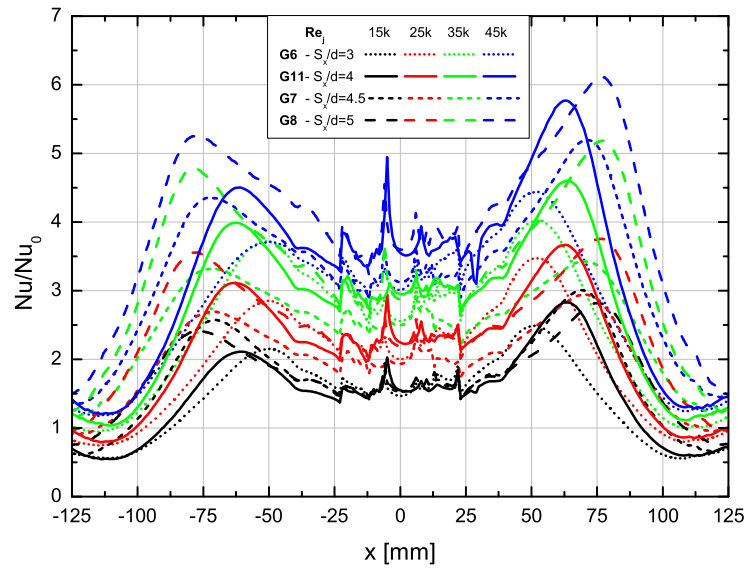
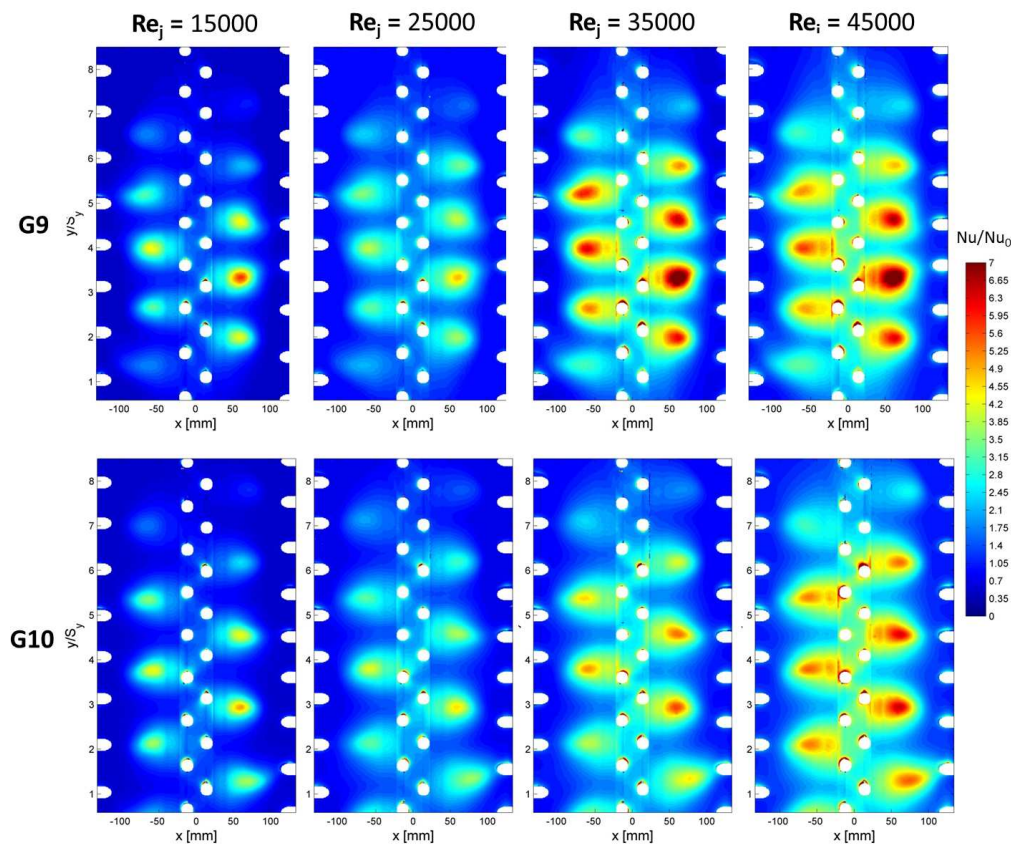


Figure 5.39: Effect of the tangential pitch in tangential direction: **G6** vs **G11** vs **G7** vs **G8**

averaged plots have shown a global Nusselt number increase with higher tangential jet-to-jet spacing.

### 5.2.4 Effect of the Radial Pitch



**Figure 5.40:** ALSTOM contour plots. Effect of the radial pitch

Figure 5.40 compares geometries **G9** and **G10** in terms of 2D contours, while Figures 5.41 and 5.42 show the averaged Nusselt number in radial and tangential direction, including also the reference geometry **G11**. The discontinuity in the tangential averaged values in correspondence of  $x = \pm 25$  mm is due to optical distortions generated along the conjunction planes, between the lateral walls and the curved central region.

An increased radial pitch entails a higher portion of tested surface being

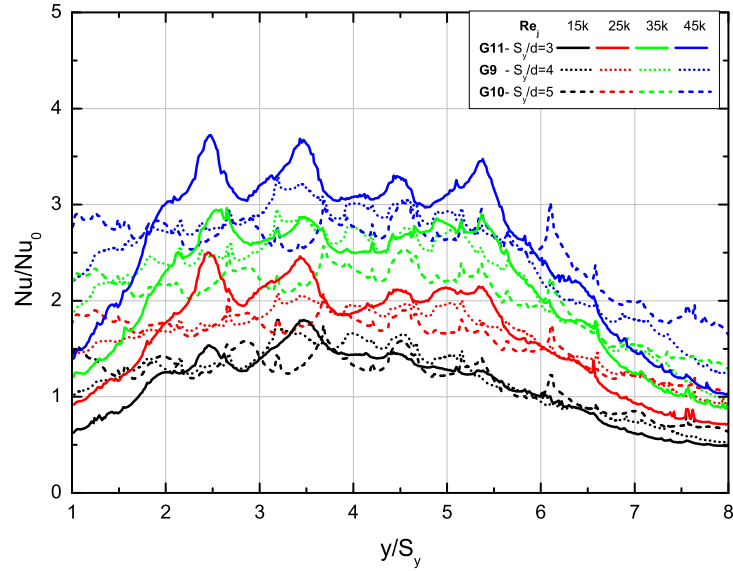


Figure 5.41: Effect of the radial pitch in radial direction: **G9** vs **G11** vs **G10**

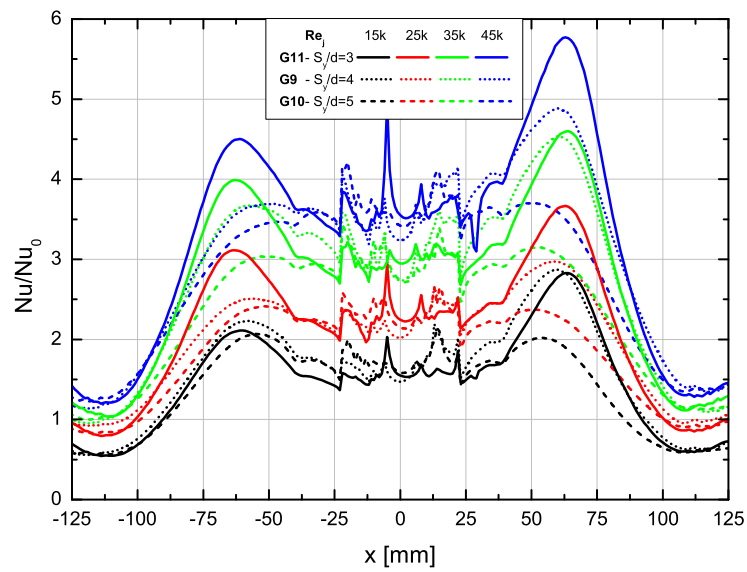


Figure 5.42: Effect of the radial pitch in tangential direction: **G9** vs **G11** vs **G10**

impacted by the impingement jets. The main result to underline is that a different radial pitch from the reference **G11** case leads to a different relative position between the impingement jets and the extraction holes. This aspect could locally affect the Nusselt number distribution, in particular for the cases in which the jets and extraction holes are aligned, as visible in **G9** and **G10** Nusselt number contours.

Looking at the averaged Nusselt values, no noticeable differences can be accounted for along the radial direction (Fig. 5.41), while in the tangential direction it can be seen that the G11 test has always given higher Nusselt number values at all the tested Reynolds numbers. Figure 5.42 shows also that the highest radial pitch represented by geometry G10 has entailed lower Nusselt numbers.

As already pointed out, this result is mainly due to the different relative position between the impingement jets and the extraction holes that affects the intensity of the Nusselt number peaks and their distribution.

### 5.2.5 Comparisons Between the Tested Geometries

Finally, a comparison between the tested geometries with a double array of circular holes and an opening angle of  $\vartheta = 100^\circ$ , in spatially averaged terms, is reported in Fig. 5.43. Due to the different hydraulic diameter between the tested impingement geometries, geometries **G1**, **G2**, **G3**, **G4** and **G12** are not considered in this comparison.

The plot shows that the most effective parameter modification to obtain an increase in the internal heat transfer, is an increase in the tangential jet-to-jet distance. In fact, the highest Nusselt values, at all tested Reynolds numbers, have been measured with geometry **G8**, with a global increase of about 20% with respect to the reference case (**G11**). Such behaviour is due to two effects that are combined together: the first one is that a reduction of the tangential pitch increases the jet-to-target surface distance and reduces the area affected by the impinging jet, hence limiting the heat transfer enhancement. The second one is that in the central curved area heat transfer enhancement is mainly driven by the shower-head extraction, hence, even if impingement jets are closer to the extraction, this area is

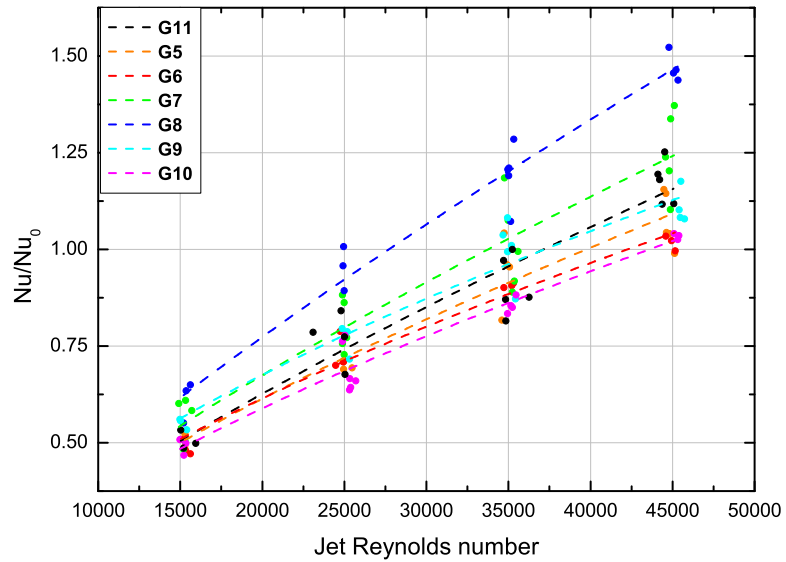


**Figure 5.43:** Comparisons between the tested geometries

only marginally affected. Geometry **G7** has given a slight Nusselt number increase of about 7 - 8%, in particular at higher Reynolds numbers. The other geometries do not affect the global Nusselt number in a positive manner.



# Chapter 6

## Optimized Geometries

Results found from the baseline geometries, together with a numerical DOE analysis carried out within the ERICKA project, have provided the guidelines for the definition of several AVIO and ALSTOM optimized geometries.

### 6.1 Heat Transfer Results on AVIO Optimized

The configuration C3 baseline has been used as a basis for an optimized geometrical investigation. This choice is based on the analysis of the DOE results using 124 CFD runs to explore changes in fin and hole geometries and their relative position, performed within the European Project ERICKA and based on the results of this research project.

No evident trends have been found except for the fact that cooling performance decreases whenever impinging cooling air hits a discharge hole and exits the leading edge cavity. To reduce this effect, according to experimental results shown on the C3 baseline, a shift of the jet holes has been proposed (named HS geometry). Moreover, to further explore possible optimisation, a shift in fin locations is proposed to be experimentally investigated (named FS geometry).

All the measurements are focused only at  $\% Cr = 40$  at three jet Reynolds numbers  $Re_j = 20000 - 30000 - 40000$ .

### 6.1.1 REF Results

Before giving details on the proposed AVIO optimized geometries, it is interesting to highlight the effect of the large fins on the heat transfer distribution. For this reason a reference "REF" test has been performed without large fins inside the cavity, as shown in Fig. 6.1, keeping the impingement jet position and the mass flow split at the extraction unvaried.

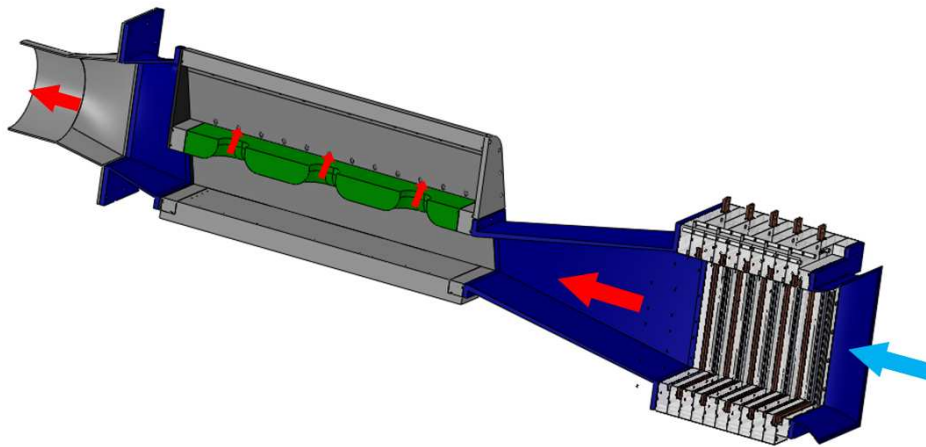


**Figure 6.1:** Geometry AVIO reference "REF" test

The left side of Fig. 6.2 illustrates the two-dimensional Nusselt number contours of the AVIO "REF" geometry at the three tested jet Reynolds numbers. Results are expressed in terms of  $Nu/Nu_0$  where  $Nu_0$  represents the averaged Nusselt value evaluated at  $Re_j = 10000$  and  $\% Cr = 10$  of the geometry C3 baseline.

Maps show a global increase in the Nusselt number directly related to the jet Reynolds number, as already found in the other geometries.

The Nusselt number distributions show three large areas with increased heat transfer coefficient that represent the stagnation regions of the jets; in particular, the first and the second jets generate almost circular stagnation regions, while the third jet located at  $y/S_y = 10$  generates a stretched stagnation region due to the spurious influence of the edge of the model.

Moreover, the distributions appear more concentrated on the suction side of the model, clearly due to the mass flow split imposed at the extraction.



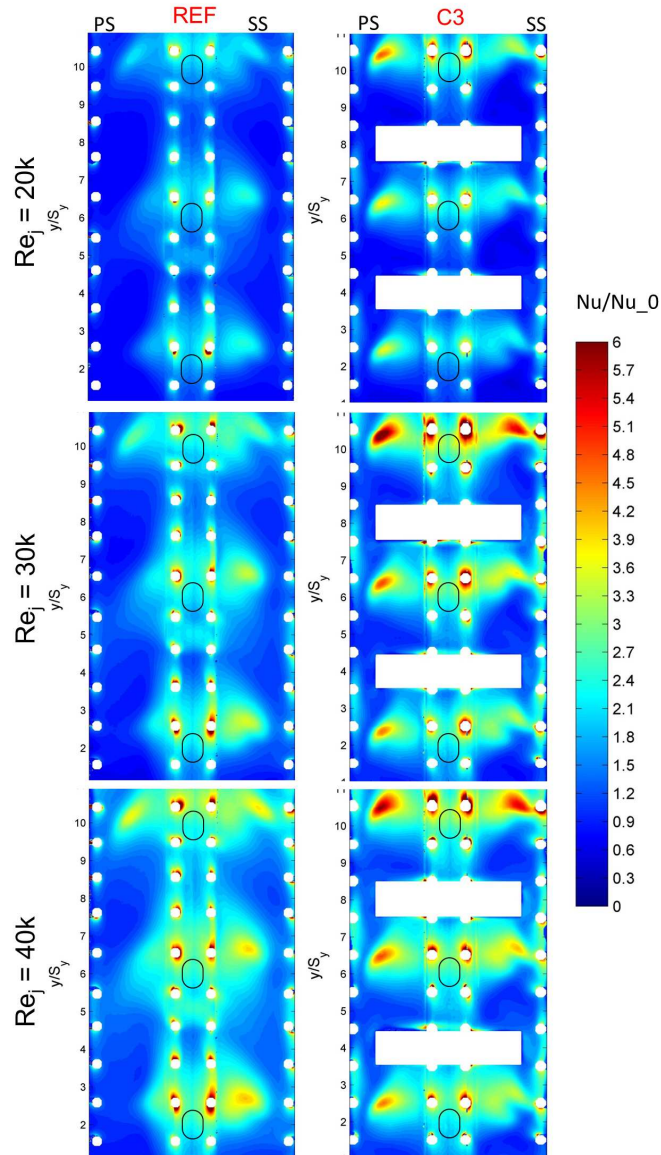


**Figure 6.2:** AVIO "REF" vs C3 maps

Even more interesting is the comparison between the C3 baseline geometry and the "REF" test which highlights the effect of the large fins. The shape of the stagnation region is strongly affected by the presence of fins, moving from an almost circular shape visible in the "REF" maps to a lengthened shape in the tangential direction with four distinct peaks. An-

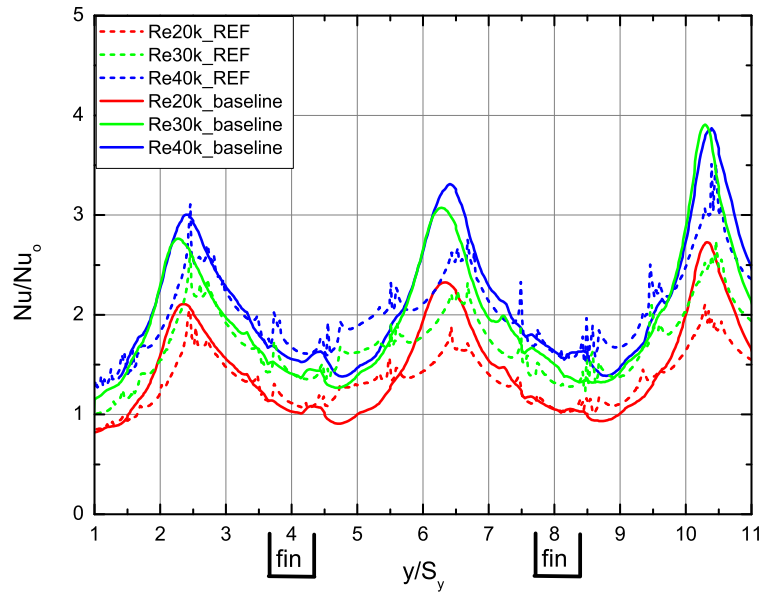


**Figure 6.3:** C3 vs "REF" test averaged values: radial direction

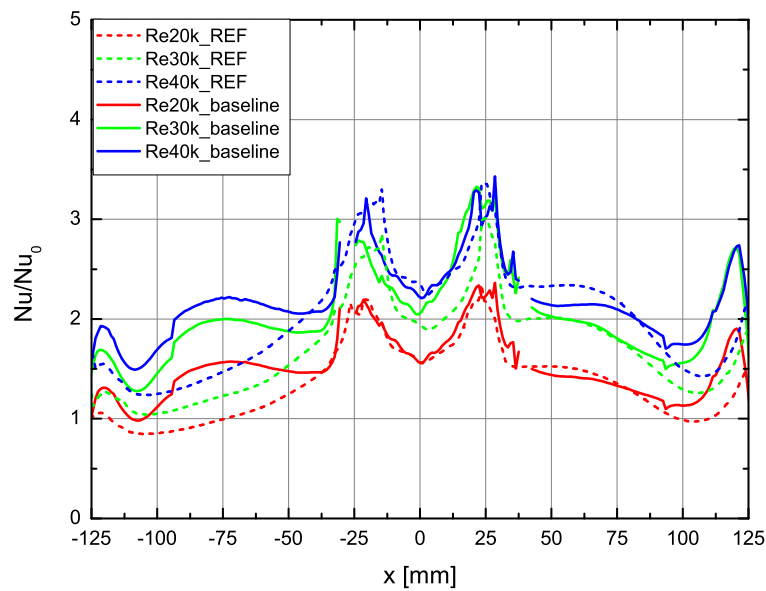


**Figure 6.4:** C3 vs "REF" test averaged values: tangential direction

other effect of the large fins is the almost symmetric distribution between suction and pressure sides, with higher peaks located on the latter, despite

the imposed asymmetrical mass flow extraction.

More details on the comparisons can be extracted by looking at the averaged Nusselt number values, in the radial and tangential direction, as illustrated in Figs 6.3 and 6.4. The radial plot shows that in presence of fins, averaged Nusselt values are higher in correspondence of the jet stagnation regions, while close to the regions where fins are located, the "REF" test has provided slightly higher Nusselt numbers. In the tangential direction, differences between the two tests are clearly visible, in particular on the pressure side of the model ( $-125 < x < -25$  mm). As already pointed out looking at the maps, the presence of the fins strongly reduces the asymmetry due to the imposed mass flow split, resulting in higher Nusselt number values compared to the "REF" case.

From the results presented, the positive effects of the presence of the fins are clearly visible, leading to a global Nusselt number enhancement.

The present study do not consider the conduction effects due to the presence of the fins, however Da Soghe et al. [66] have showed that even if the presence of the fins realizes an entrapment condition for the coolant jet, leading to an augmentation of the heat transfer coefficient peaks, their impact on the heat removed results marginal.

### 6.1.2 Hole Shift Results

The first proposed optimized geometry (HS) is characterized by a shift in the impingement jet position compared to the C3 baseline geometry, as illustrated in Fig. 6.5. The position of the large fins remains the same between the two configurations.

The impingement holes are shifted by  $1/2$  extraction hole pitch backward along the radial direction. This shift is motivated by the C3 baseline results (Fig. 5.19), where at a higher % Cr the impingement jets are not able to completely deflect the coolant flow, due to their small length-to-diameter ratio ( $l/d_h$ ).

The comparison in terms of Nusselt number distributions among the optimized HS and FS and the baseline C3 geometries is shown in Fig. 6.6.

When considering HS and C3 geometries (see maps located in the center

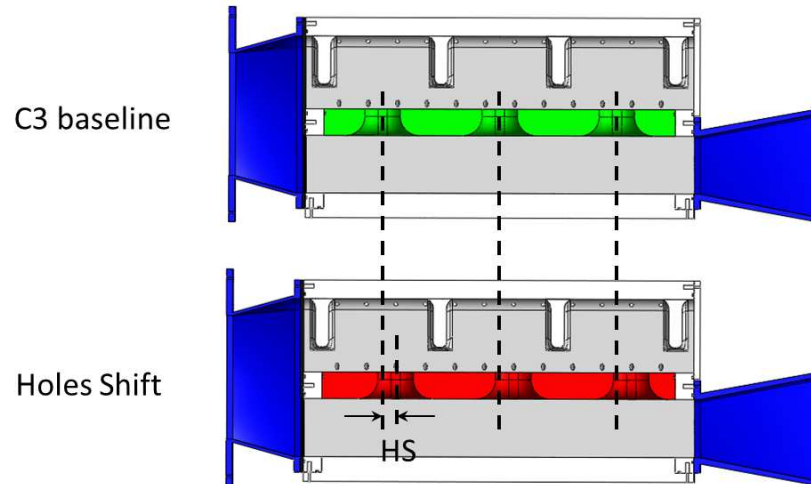


**Figure 6.5:** AVIO optimized Holes Shift geometry

and on the right respectively), it is possible to appreciate the effect of the impingement hole shift. The crossflow condition in the feeding channel leads to an offset between the center of the cold bridge holes and the jet stagnation region, as already seen in the C3 results, but in the present case the location of the stagnation region is located exactly in the center of the impingement module. This evidence affects the stagnation region shape that appears almost circular with higher values in the central curved region.

When studying the averaged Nusselt number plots reported in Figs. 6.7 and 6.8, other interesting aspects can be highlighted.

Along the radial direction (Fig. 6.7) differences between the two geometries are located far from the location of the fins, which is due to the different shape of the jet stagnation regions. In the C3 case, the coolant jet is more affected by the presence of the fins leading to a more pronounced jet spreading that results in Nusselt number peaks also on the lateral walls. The intensity of these peaks is also higher than in the central region due to a local shorter jet-to-target surface distance. Practically the same values have been found near the fins regions.

With regard to the averaged Nusselt number in the tangential direction, the HS geometry gives slightly higher values only in the curved central region

( $-40 < x < +40$  mm). Moreover, it is interesting to note that the HS geometry is rather affected by the mass flow split, therefore slightly higher Nusselt number values have been found on the suction side rather than in the pressure.

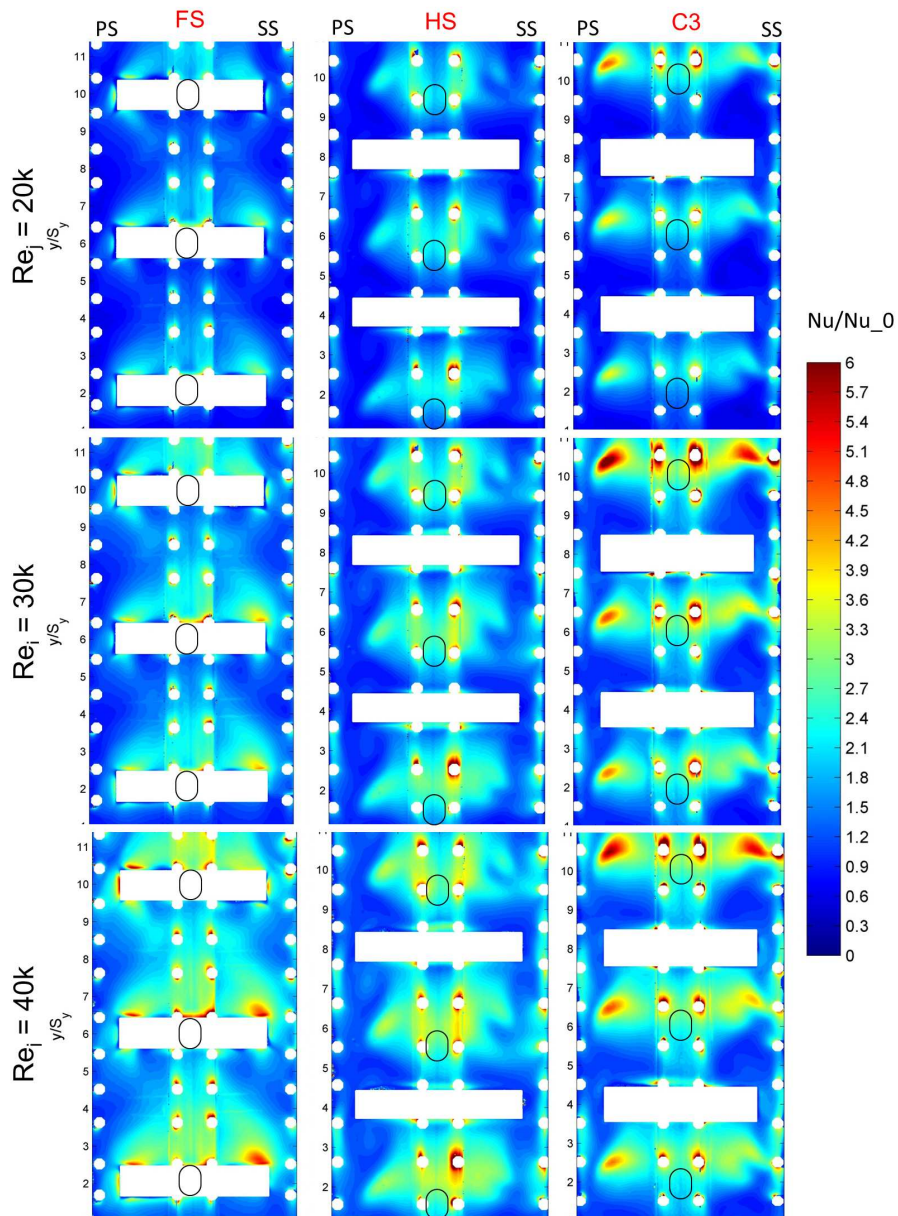


Figure 6.6: AVIO FS vs HS vs C3 maps

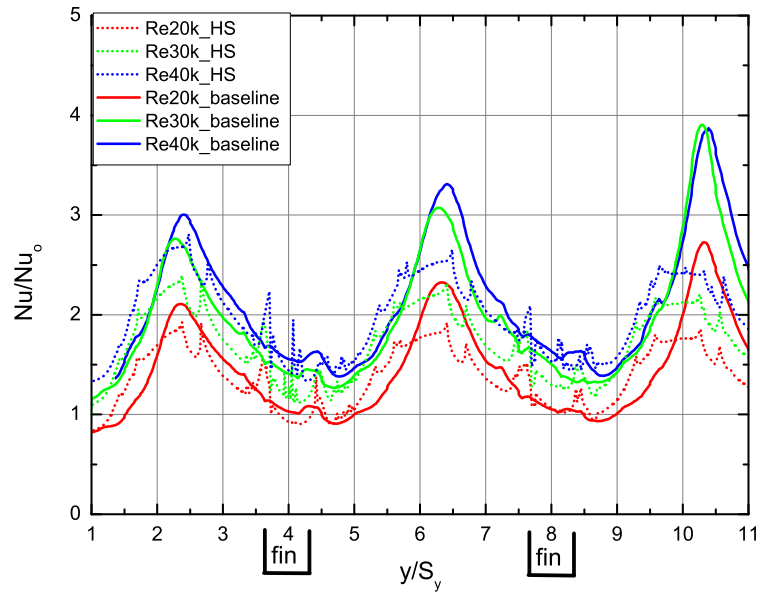


Figure 6.7: C3 vs HS averaged values: radial direction

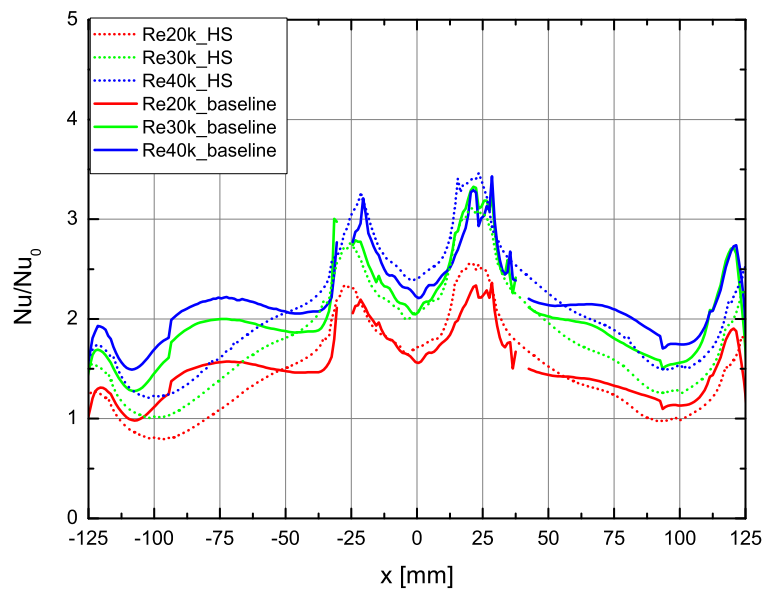
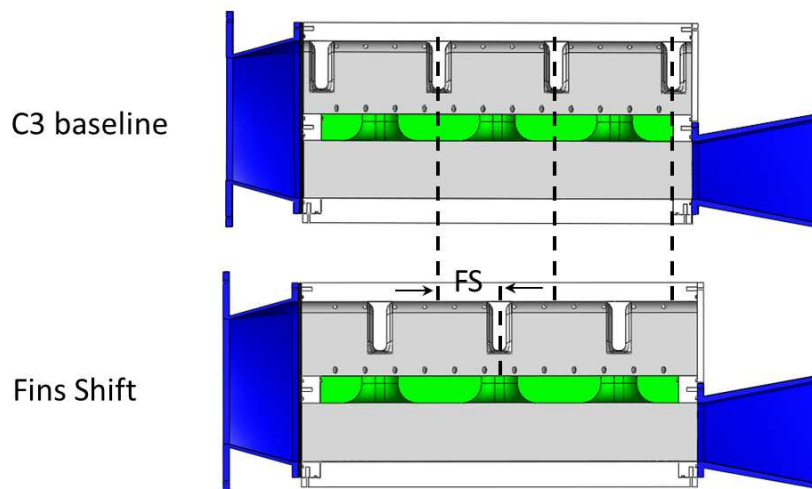


Figure 6.8: C3 vs HS averaged values: tangential direction

### 6.1.3 Fins Shift Results

The second, and last, selected AVIO optimized (FS) is characterized by a shift in the position of the large fins, compared to the C3 geometry as illustrated in Fig. 6.9. The position of the impingement jets, in this case, remains the same between the two configurations.

The large fins are now aligned with the impingement jets.



**Figure 6.9:** AVIO optimized Fins Shift geometry

On the left of Fig. 6.6 contours plots related to the FS geometry are shown. The maps do not highlight an area with concentrated Nusselt number enhancement, this means that the jet stagnation region is mainly located on the fins. However, it is interesting to note that downstream the fins there is a uniform increase in the Nusselt number, especially at higher jet Reynolds numbers. In fact, comparing the FS maps with the other configurations reported in Fig. 6.6, the Nusselt number distribution found in the FS geometry seems more uniform along the target surface, indeed, an even large area is affected by the heat transfer increase. This result might be very interesting if the objective function of the optimization process is an increased portion of area affected by the heat transfer enhancement, with quite a uniform distribution. This means a lower thermal gradient along the radial and tangential

direction of the airfoil.

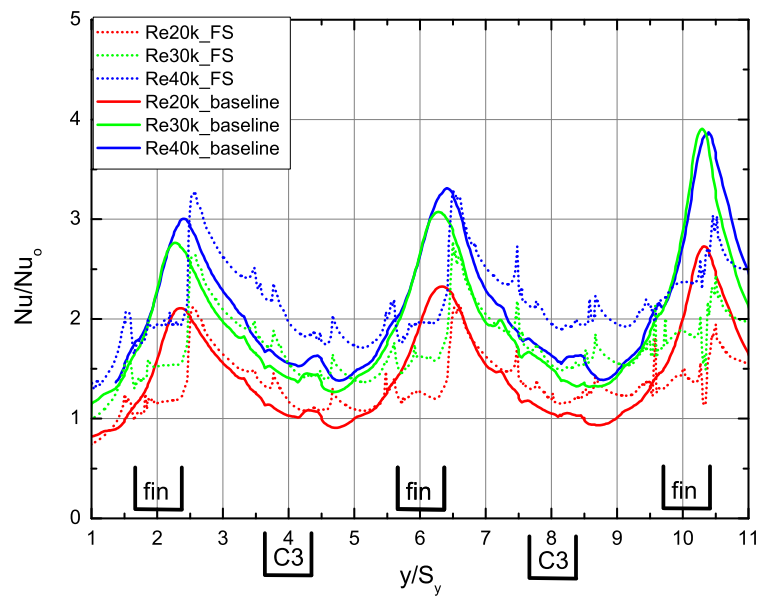


**Figure 6.10:** C3 vs FS averaged values: radial direction

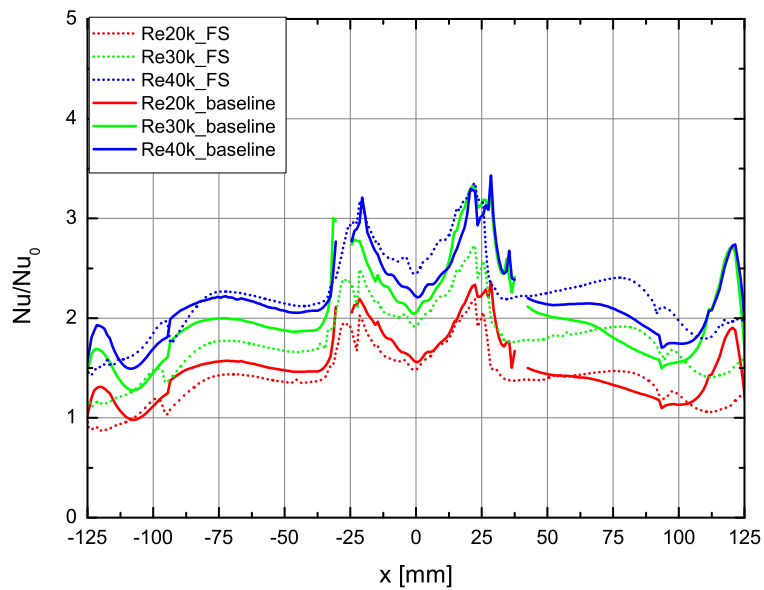


**Figure 6.11:** C3 vs FS averaged values: tangential direction



Figures 6.10 and 6.11 show the averaged Nusselt number in the radial and tangential direction respectively.

The plots in the radial direction highlight the absence of specific Nusselt number peaks in the FS configuration compared with the C3. This evidence clearly means noticeable differences in the higher values measured between the two cases. However, higher Nusselt number values have been found far from the fins, with a shift in the fins location, confirming the evidence shown in the maps.

Looking at the averaged values along the tangential direction, differences between the two geometries are small, with slightly higher Nusselt numbers found on the SS in the FS case.

Moreover, it is important to note that all the reported results do not consider the heat removed by forced convection from the fins that might be not a negligible contribution, especially in the FS case where part of the jet stagnation region is located on the fin surface.

Finally, Fig. 6.12 shows the comparison in terms of spatially averaged Nusselt numbers among all the geometries reported in the present section.

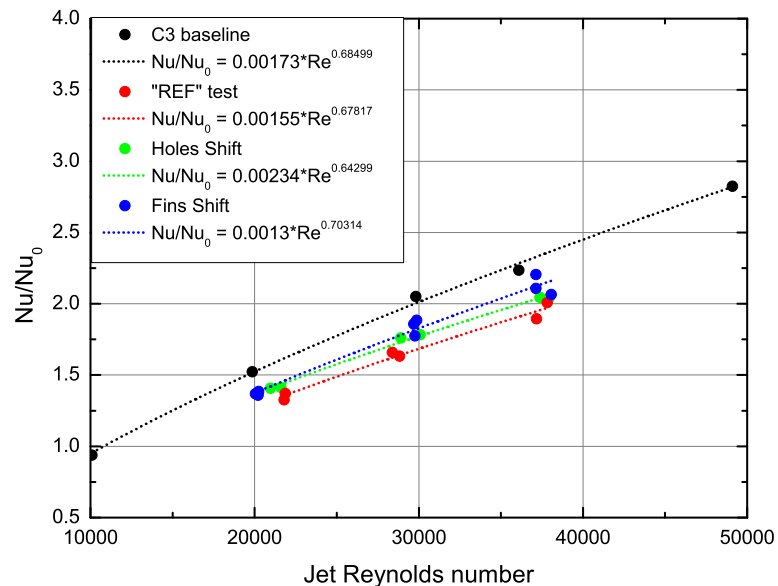


**Figure 6.12:** AVIO optimized vs C3 spatially averaged values

This graph effectively summarize all the findings reported in the present section. Higher spatially averaged Nusselt numbers have been found with the baseline C3 geometry, while lower values have been found without fins in the leading edge cavity.

A very interesting finding is that among the selected optimized geometries, the alignment of the fins with the impingement jets, represented by the FS test, has given higher values than the "REF" and HS cases.

To conclude this section, the presence of the fins inside the cavity is important to globally increase the internal heat transfer coefficient. The selected optimized geometries do not seem to be able to further increase the Nusselt number in terms of peak intensity. However, the optimized geometries, in particular aligning the fins with the impingement holes, have given a more uniform heat transfer distribution which means a higher portion of area affected by heat transfer enhancement. Thus, if the aim of the optimization process is focused on the research of the maximum heat transfer coefficient value, the C3 baseline already represents the best solution among the considered geometries. On the other hand, if the aim is focused on the achievement of an increased portion of area affected by the coolant flow, therefore avoiding the generation of "hot spots" inside the cavity, then the FS geometry has surely offered interesting suggestions. It is also important to underline that the presented results do not consider the heat removed by forced convection from the fins, so a further analysis could be very interesting taking also into account this last effect.

## 6.2 Heat Transfer Results on ALSTOM Optimized

Experimental results, together with the numerical CFD analysis carried out within the ERICKA project, highlight that the geometry G8 guarantees the maximum increase in the Nusselt number among all the considered configurations. Hence, by means of an intensive CFD campaign launched by the partners of the project, several configurations were explored varying the

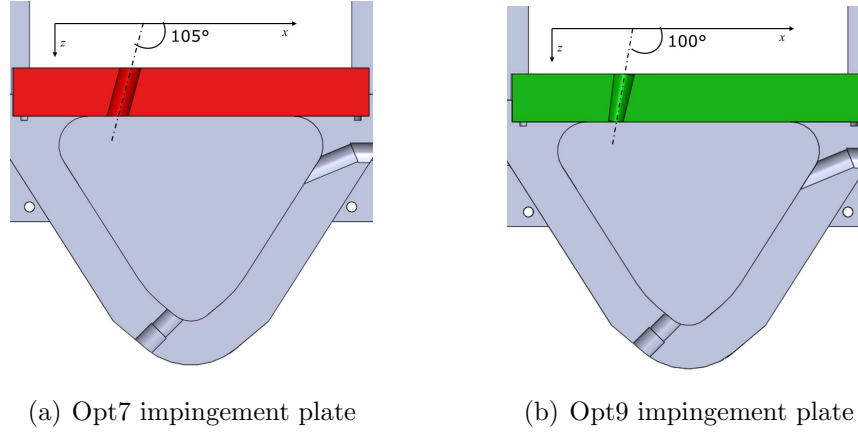


**Figure 6.13:** ALSTOM optimized geometries

impingement jet shape, jet injection angle and the relative position between jet and extraction holes. The result leads to the definition of two optimized geometries, Opt7 and Opt9, that will be explained in detail in the next sections. Both geometries Opt7 and Opt9 have been tested with the external geometry **LE 2** that is more engine representative than the narrow opening angle.

All the measurements have been performed at six jet Reynolds numbers  $Re_j = 10000 - 20000 - 30000 - 35000 - 40000 - 50000$ .

### 6.2.1 Opt7 and Opt9 Results

Geometries Opt7 and Opt9 are characterized by racetrack impingement jets with a hydraulic diameter of  $d_j = 19.45$  mm. As illustrated in Fig. 6.13 jets are inclined with respect to the  $x$  direction. In particular, geometry Opt7 has jets inclined by  $105^\circ$  with a constant cross-section area, while geometry Opt9 has jets inclined by  $10^\circ$  and a convergent cross-section area with an outlet jet diameter of  $d_{j,out} = 0.71 d_j$ .

Moreover, differently from baseline geometries, the relative position between the impingement jets and the extraction holes is inverted, so the jets are now aligned with the shower-head holes. The main geometrical characteristics of the two optimized geometries are summarized in Table 6.1.

Figure 6.14 shows the two-dimensional Nusselt number contours for the

	Geometry Opt7	Geometry Opt9
Jet inclination	105°	100°
Jet shape	<i>Racetrack</i>	<i>Racetrack</i>
Hole shape	<i>Constant cross-section</i>	<i>Convergent cross-section</i>
Jet position	<i>Aligned with SH holes</i>	<i>Aligned with SH holes</i>
Radial pitch	$y/d_j = 3.1$	$y/d_j = 3.1$
Tangential pitch	$x/d_j = 5.1$	$x/d_j = 5.1$

Table 6.1: ALSTOM Opt main characteristics

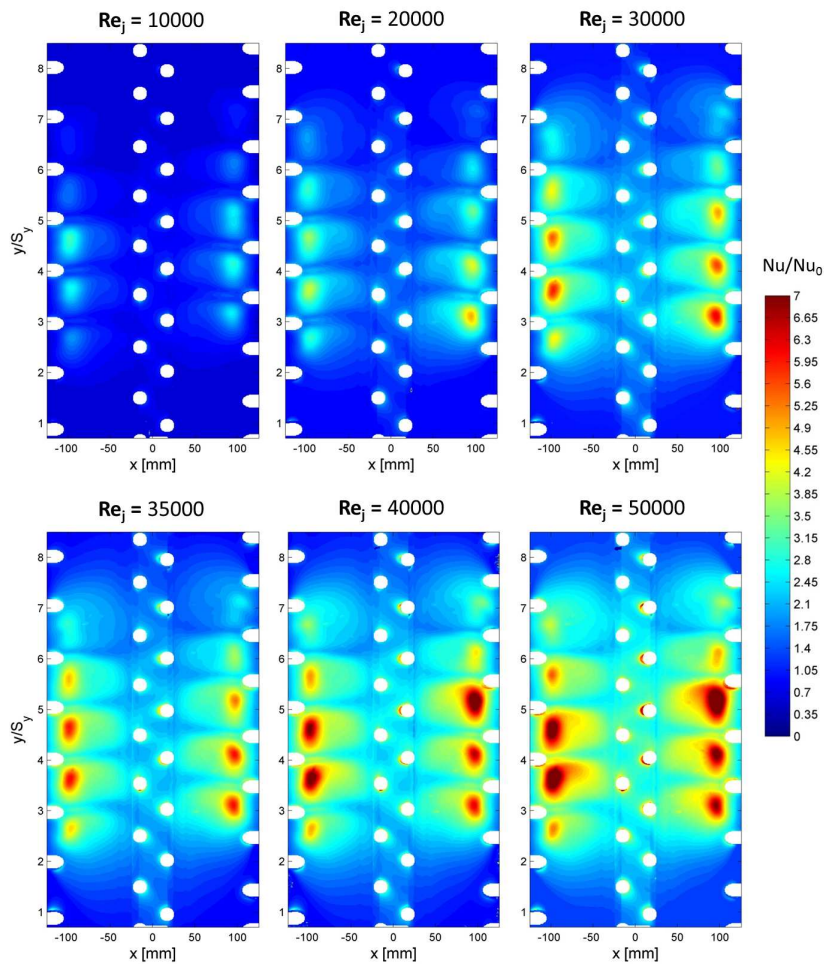


Figure 6.14: ALSTOM Opt7 contour plots

six tested jet Reynolds numbers. Results are expressed in terms of  $Nu/Nu_0$  where  $Nu_0$  is the spatially averaged Nusselt number evaluated with geometry G11. Hence, the same reference values are chosen to allow direct comparisons with the baseline geometry G8, already introduced in Tab. 4.2.

The maps confirm the strong dependence of the Nusselt number directly related to the jet Reynolds number, as already seen in the baseline geometries results.

For each contour plot it is evident that the number of Nusselt peaks is related to the number of the impingement jets and, differently from geometry G12, the 10 peaks generated by the impingement jets are well defined with a

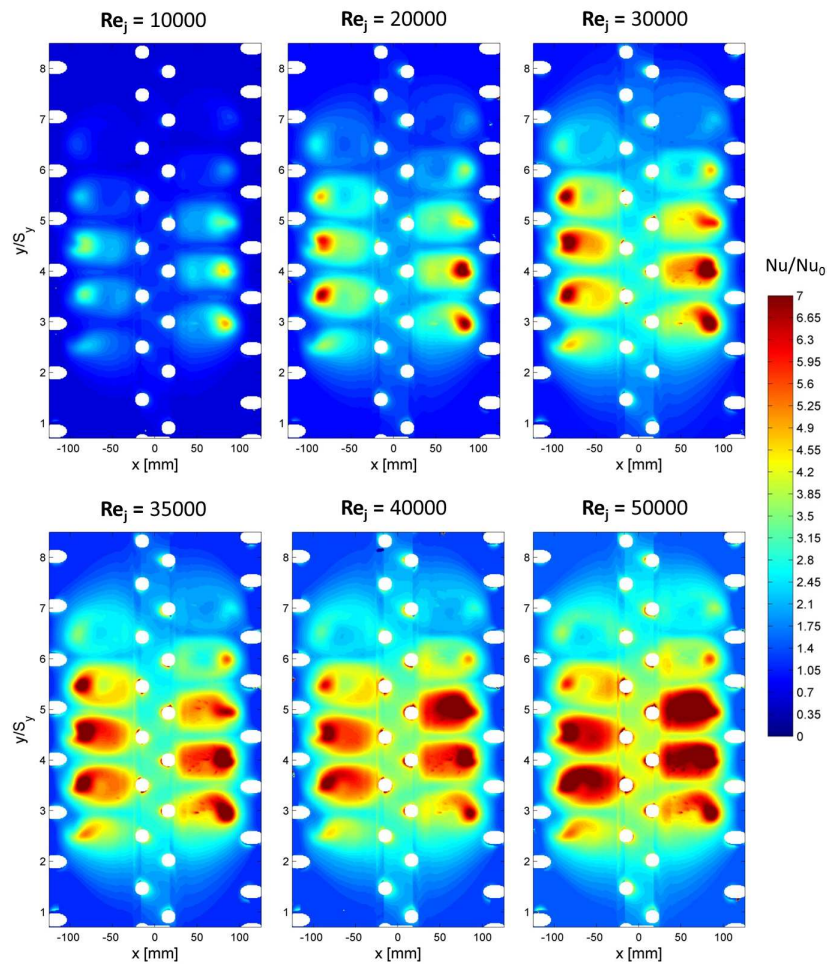


Figure 6.15: ALSTOM Opt9 contour plots

racetrack shape.

Jet stagnation regions are located very close to the film cooling extraction holes due to the inclination of impingement jets. In particular, the hole inclination combined with the inclined target surface lead to a decrease of the resulting jet-to-target surface distance  $Z/d_j = 3.3$ , with a related increase in the Nusselt number in the stagnation region with respect to the values measured at geometry G8.

Even if the jet stagnation region is very close to the film cooling extraction holes, a relevant heat transfer increase has been also found along the lateral walls and in the central curved region, due to the extraction from the shower-head holes together with the positive pressure gradient generated by the inclined side walls.

As regards the geometry Opt9 results, Fig. 6.15 shows the two-dimensional Nusselt number contours for all the tested jet Reynolds numbers.

The convergent shape of the impingement holes leads to a sharp increase in the Nusselt number in the stagnation region, due to the higher momentum of the jets. Very interesting to note is the shape of the jet stagnation region. Contrary to what was seen in the two-dimensional contours of Opt7, in this case each jet generates a different stagnation region shape. In particular, some areas assume an annular ring shape, as can be seen in the detailed view shown in Fig. 6.16.

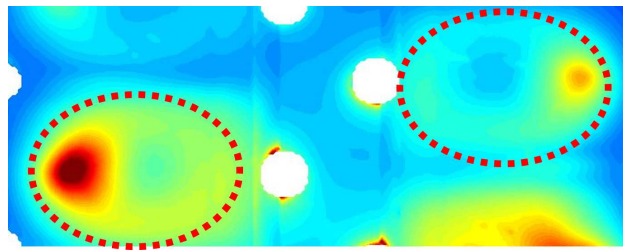


**Figure 6.16:** ALSTOM Opt9 detailed view

The peak near the FC extraction holes indicates the jet stagnation point, then a separation seems to occur with a reattachment near the shower-head extraction holes, resulting in an enlargement of the area scoured by the impinging cooling flow.

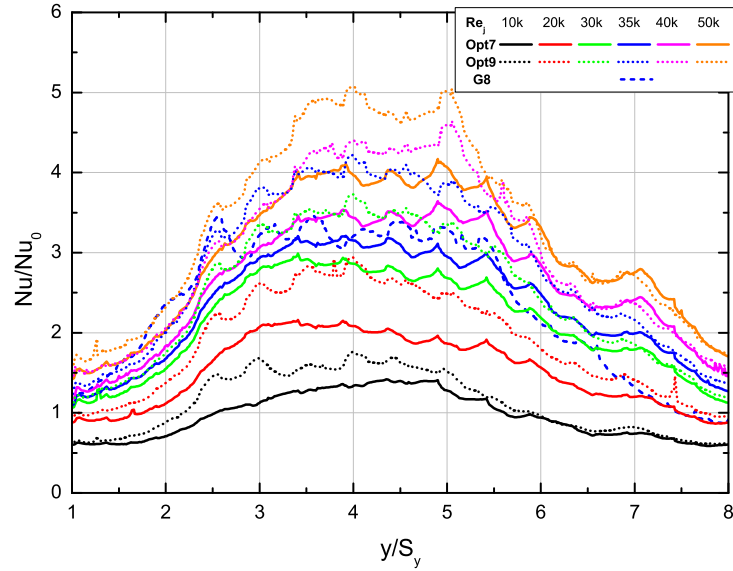


Figure 6.17: Averaged Nusselt number for Opt7 and Opt9: radial direction

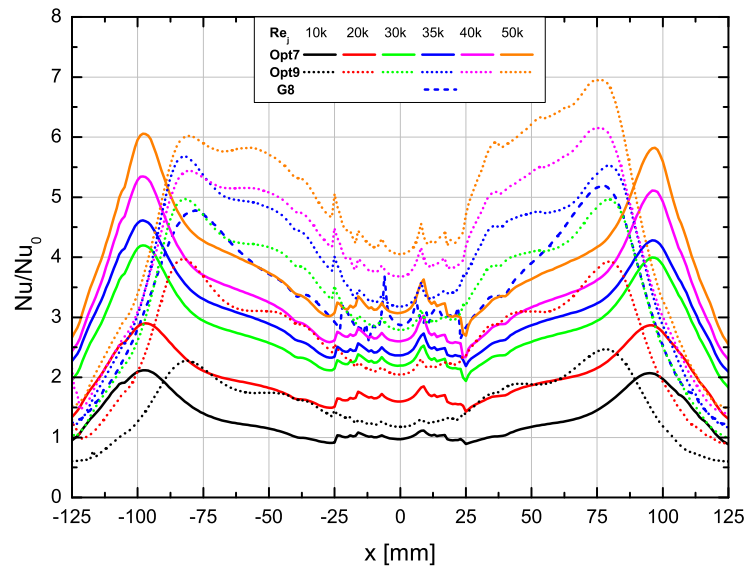


Figure 6.18: Averaged Nusselt number for Opt7 and Opt9: tangential direction

The plots reported in Figs. 6.17 and 6.18 are very useful to compare between geometries Opt7 and Opt9. Moreover, the baseline geometry G8 at  $Re_j =$

35k is given as a reference.

Along the radial direction, geometry Opt9 has given higher Nusselt number for all the tested Reynolds numbers with a global increase of about 20 - 30% with respect to geometry Opt7.

The averaged Nusselt number trends in the tangential direction highlight well the differences between the two geometries in terms of maximum Nusselt number and its distribution.

The first evidence of this is the peak location, very close to the film cooling extraction arrays for geometry Opt7; more centred along the lateral walls are peaks found with geometry Opt9, with overall higher Nusselt number values. Another interesting aspect is the variation of the Nusselt number along the lateral walls. In fact, as already seen in the two-dimensional contours, Opt9 guarantees quite a uniform Nusselt number increase on the lateral sides, with a less marked variation between  $x = 75$  and 25 mm compared to the trend found with geometry Opt7 that is characterized by a sharp decrease from the stagnation region to the shower-head extraction. Last, but not least, geometry Opt9 is the only geometry among all the tested ones, that has led

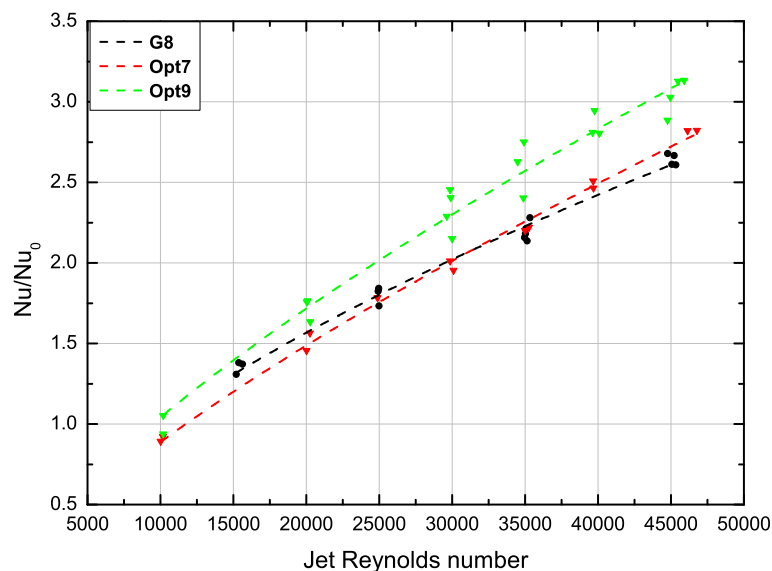


**Figure 6.19:** Spatially averaged Nusselt number for Opt7, Opt9 and G8



to a substantial Nusselt number increase also in the central curved region, with an increase of about 25 - 30% for all the tested jet Reynolds numbers.

Finally, to summarize all the discussed results, the spatially averaged Nusselt numbers are shown in Fig. 6.19.

The optimized geometry Opt7 does not improve the overall heat transfer coefficient compared with the baseline geometry G8, with small differences that can be accounted for by the measurement uncertainty. On the contrary, as already pointed out in the previous plots, geometry Opt9 generates a constant increase at all the tested jet Reynolds numbers.

To conclude this section, the present experiments have undoubtedly shown that the selected optimized geometry Opt9 represents a highly potential solution for the internal leading edge cooling because it allows to increase the internal heat transfer coefficient while keeping the coolant mass flow rate constant. However, the reported results on geometry Opt9 need to be considered together with the manufacturing constraints, that could be more challenging compared to the baseline geometries, and on the different pressure ratio required to feed the leading edge cavity keeping the coolant mass flow rate constant.



# Conclusions

An intensive experimental study has been conducted to better understand and highlight the effects of complex fluid-dynamic interactions inside a leading edge cavity of typical gas turbine airfoils on the internal heat transfer distribution. The study was carried out in the framework of the European Research project ERICKA, working together with the industrial partners AVIO and ALSTOM Switzerland that have provided the geometries and test conditions, reported in this research paper.

The study has been carried out on a dedicated test rig designed to house different scaled up leading edge models characterized by different internal impingement geometries, coolant extractions from shower-head and film cooling holes and different flow arrangements. The experiments have been performed using a transient technique with narrow band Thermo-chromic Liquid Crystals that allows to obtain a detailed two-dimensional distribution of the heat transfer coefficient on the tested surface. Even though several already published works on the internal heat transfer in leading edges can be found, the present study can be considered unique and innovative because it gives very interesting details not reported in the open literature, in complex flow arrangements that reproduce the actual inlet and outlet feeding conditions inside real airfoils leading edge cooling schemes rather well.

In addition to the experimental results reported in this thesis, the present research has allowed to further develop new experimental devices such as the mesh heater, that was designed and manufactured in-house, and to improve the post-processing procedure dealing with transient heat conduction problems within cylindrical domains.

The experimental results expressed in terms of Nusselt number distribu-

tion inside the leading edge cavity provided by the baseline geometries have set the guidelines for the definition of several optimized geometries that were tested in the last period of the activity.

All the experiments have shown a strong dependence on the Nusselt number with the jet Reynolds number in terms of peak intensity and its distribution. Other interesting results need to be analyzed considering the different tested geometries separately.

As far as the AVIO geometries are concerned, three different leading edge cooling schemes have been tested. Geometry B2, composed of an internal impingement sheet with four arrays of circular holes, has shown an offset between the center of the jet hole and the location of the Nusselt number peaks. This finding is accounted for by the potential core impinging on the target surface, due to the low jet-to-target surface distance of  $Z/d_j = 1.57$  with additional effects due to the curvature of the target surface.

As Geometry B2, geometry B3 has an impingement sheet with four arrays of circular impingement holes, but located in an asymmetric arrangement along the tangential direction. Moreover, tests have been performed imposing a different mass flow extraction between the arrays of extraction holes, and in different crossflow conditions in the feeding channel. Results clearly have shown that the Nusselt number distribution is not influenced by the mass flow split and different flow arrangements but is dependent only on the jet Reynolds number variation. On the contrary, the impingement hole discharge coefficient is strongly influenced by different feeding conditions, with higher values found at a lower crossflow percentage, that is representative of the tip of the blade.

Finally, geometry C3 is composed of an impingement plate with three large racetrack holes and large fins inside the leading edge cavity. Moreover, similarly to geometry B3, a different mass flow extraction has been imposed between the pressure and suction side and different crossflow conditions in the feeding channel. Results show that for each impingement module delimited by two consequent fins, the heat transfer coefficient peaks are located in four lobes. The number of such lobes is found to be related both to the

---

pressure gradient generated by the wedge-shaped leading edge and to the presence of the shower-head extraction holes. Nusselt number trends confirm what Metzger and Bunker [9] and Taslim et al. [36] already pointed out: they show the relevant impact of the  $Re_j$  on the heat transfer. The experiments also highlight that the asymmetric mass flow extraction and variable crossflow conditions slightly influence the Nusselt number.

With regard to the ALSTOM results, different external and internal geometries have been tested in order to highlight the influence of different leading edge opening angles, shape and number of impingement jets and their pitches along the radial and circumferential directions on the heat transfer distribution.

The effects of the leading edge opening angle is different when varying the internal impingement geometries: the Nusselt number found with the single row of circular holes is strongly affected by the leading edge opening angle. As for the internal geometries with a double row of holes (circular and race-track), a different angle  $\vartheta$  has a predominately local influence on the Nusselt number, thus leading to local distortions and a shift of the jet stagnation region, while the global results remain quite similar.

The presence of the shower-head extraction leads only to local differences in the Nusselt number distributions, in particular a lower Nusselt number magnitude was found in the central curved region without the shower-head coolant extraction, while slightly higher values were found on the lateral walls, in particular near the film cooling extraction arrays.

A variation of the tangential pitch strongly influences the Nusselt number distribution and peak intensity, in particular results have shown a global Nusselt number increase with higher tangential jet-to-jet spacing. This increase was found on the lateral regions where an increase of the tangential pitch means a reduction of the jet-to-target surface distance from  $Z/d_j = 5.95$  of **G6** to  $Z/d_j = 4.53$  of **G8**, while in the central curved region the presence of the shower-head extraction guarantees a nearly constant Nusselt number distribution among all the tested tangential pitches.

Finally, the effect of an increased radial pitch entails a higher portion of

tested surface being impacted by the impingement jets. This aspect could locally effect the Nusselt number distribution, in particular for the cases in which the jets and extraction holes are aligned. In averaged terms, the higher radial pitch tested has given the lower Nusselt number values.

The experimental results found the baseline geometries were used within the ERICKA project to validate numerical procedures, aimed at selecting several optimized configurations both for AVIO and ALSTOM. These selected optimized geometries have been manufactured and tested in the last period of the present research project.

As regards AVIO optimized geometries, they are based on the C3 baseline configuration, changing the relative position between impingement jets and large fins.

The selected optimized geometries do not seem to be able to further increase the Nusselt number in terms of peak intensity. However, if the main aim is to achieve an increased portion of area interested by the coolant flow with uniform heat transfer values, the geometry FS has produced very interesting results.

As for ALSTOM, two optimized geometries have been tested characterized by racetrack inclined nozzles, one with a constant cross-section area, named Opt7 and the other with a convergent profile, named Opt9.

Results from geometry Opt9 have shown that the selected optimized geometry Opt9 represents a very attractive solution for the internal leading edge cooling because it provides an increase of about 20 - 30% with respect to the baseline considered geometries at all the tested jet Reynolds numbers, thus it strongly improves the internal heat transfer removal keeping the coolant mass flow rate constant. However, results on geometry Opt9 need to be considered together with the manufacturing constraints, that could be more challenging compared to the baseline geometries, and on the different pressure ratio required to feed the leading edge cavity keeping the coolant mass flow rate constant.

# Appendix





# Annex A

## Dimensionless Numbers

A similarity analysis is used to ensure that the experiment accurately models the engine conditions. The main interesting dimensionless parameters used in the present work are defined as follow:

### Reynolds number

$$Re = \frac{\rho v L}{\mu}$$

where  $\rho$ ,  $v$  and  $\mu$  are the density, velocity and dynamic viscosity of the flow, respectively, and  $L$  is the reference length.

The Reynolds number compares the inertial forces to the viscous forces in the momentum equations. The flow has a distinct boundary layer near the wall and the value of the Reynolds number indicates different flow regimes, such as laminar or turbulent flow: a laminar flow occurs at low Reynolds numbers, where viscous forces are dominant, and is characterized by smooth, constant fluid motion; a turbulent flow occurs at high Reynolds numbers and is dominated by inertial forces, which tend to produce chaotic eddies, vortices and other flow instabilities.

### Prandtl number

$$Pr = \frac{\nu}{\alpha} = \frac{c_p \mu}{k}$$

where  $\nu = \mu/\rho$ , is the kinematic viscosity and  $\alpha = k/(\rho c_p)$ , is the thermal diffusivity.

Differently to the Reynolds number, the Prandtl number contains no such length scale in its definition and is dependent only on the fluid and the fluid state. It is a measure of the ratio of the thickness of the flow boundary layer compared to the thermal boundary layer. For air, the Prandtl number is in the order of unity and therefore both boundary layers have a similar thickness. For other fluids, like waters, the Prandtl number can be as high as 14, and therefore the thermal boundary layer is much thinner than the flow boundary layer. On the other hand, the Prandtl number for a liquid metal is very small (0.02 - 0.07) and therefore the thermal boundary layer is much larger than the flow boundary layer.

### Rotation number

$$Ro = \frac{\omega L}{v}$$

where  $\omega$  is the angular velocity,  $v$  the flow velocity and  $L$  the reference length.

The Rotation number measures the relative importance or the rotational effects (Coriolis forces) compared to the through-flow in the cooling channel.

### Grashof number

$$Gr = \frac{g\beta(T_w - T_f)L^3}{\nu^2}$$

where  $g$  is the gravitational acceleration and  $\beta$  in this case represents the volumetric thermal expansion coefficient.

The Grashof number approximates the ratio of the buoyancy to viscous force acting on a fluid. It frequently arises in the study of situations involving natural convection.

## Eckert number

$$Ec = \frac{v^2}{c_p \Delta T} = \frac{\textit{Kinetic energy}}{\textit{Enthalpy}}$$

The Eckert number is the ratio between the kinetic energy and the enthalpy. It is dimensionless quantity useful in determining the relative importance in a heat transfer situation of the kinetic energy of a flow.

## Rayleigh number

$$Ra = \frac{g\beta}{\nu\alpha} (T_w - T_f) L^3 = Gr \cdot Pr$$

The Rayleigh number is associated with the buoyancy driven flow (free convection or natural convection). When the Rayleigh number is below the critical value for that fluid, heat transfer is primarily in the form of conduction; when it exceeds the critical value, heat transfer is primarily in the form of convection.

It can be defined also as the product of the Grashof number and the Prandtl number. Hence, the Rayleigh number itself may also be viewed as the ratio of buoyancy and viscosity forces times the ratio of momentum and thermal diffusivity.



# Bibliography

- [1] E. M. Greitzer, Z. S. Spakovszky, and I. A. Waitz. *Thermodynamics and Propulsion*. Massachusetts Institute of Technology, 2009.
- [2] J. C Han, S. Dutta, and S. V. Ekkad. *Gas Turbine Heat Transfer and Cooling Technology*. Taylor & Francis, first edition, 2000.
- [3] B. Lakshminarayana. *Fluid Dynamics and Heat Transfer of Turbomachinery*. John Wiley & Sons, Inc., 1996.
- [4] Rolls-Royce plc. *The Jet engine*. fifth edition, 1996.
- [5] J. C. Han and M. Huh. Recent studies in turbine blade internal cooling. *Journal of Heat Transfer Research*, 41:803–828, 2010.
- [6] S. Gupta, A. Chaube, and P. Verma. Review on heat transfer augmentation techniques: Application in gas turbine blade internal cooling. *Journal of Engineering Science and Technology Review*, 5:57–52, 2012.
- [7] R. R. Sellers, F. O. Soechting, F. W. Huber, and T. A. Auxier. Cooled blades for a gas turbine engine - patent 5720431. *United State Patent*, 1998.
- [8] Hyung Hee Cho, Kyung Min Kim, and Jiwoon Song. Application of impingement jet cooling systems blade internal cooling. *In: Cooling Systems: Energy, Engineering and Applications*, pages 37–67, 2011.
- [9] D.E. Metzger and R.S. Bunker. Local heat transfer in internally cooled turbine airfoil leading edge regions: Part ii - impingement cooling with film coolant extraction. *J. Turbomach*, 112:459–466, 1990.

- 
- [10] M. E. Taslim, Y. Pan, and S. D. Spring. An experimental study of impingement on roughened airfoil leading-edge walls with film holes. *J. Turbomach*, 123:766–773, 2001.
- [11] Lesley M. Wright, C. Neil Jordan, and Daniel C. Crites. Impingement heat transfer on a cylindrical, concave surface with varying jet geometries. *ASME Paper*, (GT2012-68818), 2012.
- [12] Lesley M. Wright, Evan L. Martin, and Daniel C. Crites. Impingement heat transfer enhancement on a cylindrical, leading edge model with varying jet temperatures. *ASME Paper*, (GT2012-68817), 2012.
- [13] Lesley M. Wright, Evan L. Martin, and Daniel C. Crites. Computational investigation of jet impingement on turbine blade leading edge cooling with engine-like temperatures. *ASME Paper*, (GT2012-68811), 2012.
- [14] J. H. Wagner, B. V. Johnson, and F. C. Kopper. Heat transfer in rotating serpentine passages with smooth walls. *ASME J. Turbomach*, 113:321–330, 1991.
- [15] J. H. Wagner, B. V. Johnson, R. A. Graziani, and F. C. Yeh. Heat transfer in rotating serpentine passages with trips normal to the flow. *ASME J. Turbomach*, 114:847–857, 1992.
- [16] J. H. Wagner, B. V. Johnson, G. D. Steuber, and F. C. Yeh. Heat transfer in rotating serpentine passages with trips skewed to the flow. *ASME J. Turbomach*, 116:113–123, 1994.
- [17] F. Maiuolo, A. Andreini, R. Da Soghe, B. Facchini, L. Tarchi, and D. Coutandin. Experimental and numerical analysis of multiple impingement jet arrays for an active clearance control system. *J. Turbomach*, (paper in production, Transaction of ASME paper GT2012-68791), 2012.
- [18] H. Cohen, G.F.C. Rodgersa, and H.I.H Saravanamuttoo. *Gas Turbine Theory*. John Wiley and Sons Inc., New York, NY, 1996.

- 
- [19] S. Spring and B. Weigand. Internal cooling in turbomachinery. In *Jet Impingement Heat Transfer*, Lecture Series 2010-05. von Karman Institute for Fluid Dynamics, 2010.
- [20] D.E. Metzger, T. Yamashita, and C.W. Jenkins. Impingement cooling of concave surfaces with lines of circular air jets. *Journal of Engineering for Power*, 93:149–155, 1969.
- [21] D.E. Metzger, D.I. Takeuchi, and P.A. Kuenstler. Effectiveness and heat transfer with full-coverage film cooling. *ASME Journal of Engineering for Power*, 95:180–184, 1973.
- [22] D.M. Kercher and W. Tabakoff. Heat transfer by a square array of round air jets impinging perpendicular to flat surface including the effect of spent air. *ASME Journal of Engineering for Power*, 92:73–82, 1970.
- [23] H. Martin. Heat and mass transfer between impinging gas jets and solid surfaces. *Advances in Heat Transfer*, 13:1–60, 1977.
- [24] L. Florschuetz, C. Truman, and D. Metzger. Streamwise flow and heat transfer distributions for jet array impingement with crossflow. *ASME Journal of Heat Transfer*, 103:337–342, 1981.
- [25] L. Florschuetz, D. Metzger, C.C. Su, Y. Isoda, and H.H. Tseng. Heat transfer characteristics for jet arrays impingement with initial crossflow. *ASME Journal of Heat Transfer*, 106:34–41, 1984.
- [26] A. Behbahani and R. Goldstein. Local heat transfer to staggered arrays of impinging circular air jets. *ASME Journal of Engineering for Power*, 105:354–360, 1983.
- [27] R.E. Chupp, H.E. Helms, P.W. McFadden, and T.R. Brown. Evaluation of internal heat transfer coefficients for impingement cooled turbine blades. *Journal of Aircraft*, 6:203–208, 1969.
- [28] D.E. Metzger, T. Yamashita, and C.W. Jenkins. Impingement cooling of concave surfaces with lines of circular air jets. *Journal of Engineering for Power*, 91:149–158, 1969.

- 
- [29] D.E. Metzger, R.T. Baltzer, and C.W. Jenkins. Impingement cooling performance in gas turbine airfoils including effects of leading edge sharpness. *Journal of Engineering for Power*, 94:219–225, 1972.
- [30] P. Hrycak. Heat transfer from a row of impinging jets to concave cylindrical surfaces. *International Journal of Heat Mass Transfer*, 24:407–419, 1981.
- [31] D.E. Metzger and R.S. Bunker. Local heat transfer in internally cooled turbine airfoil leading edge regions: Part i - impingement cooling without film coolant extraction. *J. Turbomach*, 112:451–458, 1990.
- [32] D. H. Lee, Y. S. Chung, and S. Y. Won. The effect of concave surface curvature on heat transfer from a fully developed round impinging jet. *International Journal of Heat and Mass Transfer*, 42:2489–2497, 1999.
- [33] M. Fenot, E. Dorignac, and J. J. Vullierme. An experimental study on hot round jets impinging on a concave surface. *International Journal of Heat and Fluid Flow*, 29:945–956, 2008.
- [34] M.E. Taslim, K. Bakhtari, and H. Liu. Experimental and numerical investigation of impingement on a rib-roughened leading-edge wall. *ASME Paper*, (GT2003-38118), 2003.
- [35] M.E. Taslim and D. Bethka. Experimental and numerical impingement heat transfer in an airfoil leading-edge cooling channel with crossflow. *ASME Paper*, (GT2007-28212), 2007.
- [36] K. Elebiary and M.E. Taslim. Experimental/numerical crossover jet impingement in an airfoil leading-edge cooling channel. *ASME Paper*, (GT2011-46004), 2011.
- [37] F. Maiuolo, L. Andrei, C. Carcasci, R. Da Soghe, B. Facchini, L. Tarchi, and S. Zecchi. Heat transfer measurements in a leading edge geometry with racetrack holes and film cooling extraction. *J. Turbomach*, (paper in production, Transaction of ASME paper GT2012-69581), 2012.



- 
- [38] F. Maiuolo, B. Facchini, L. Tarchi, and N. Ohlendorf. Experimental investigation on the heat transfer in a turbine airfoil leading edge region: Effects of the wedge angle and jet impingement geometries. *10th European Turbomachinery Conference*, (ETC130-2013), 2013.
- [39] F. Maiuolo, B. Facchini, L. Tarchi, and N. Ohlendorf. Experimental investigation on the heat transfer of a leading edge cooling system: Effects of jet-to-jet spacing and showerhead extraction. *ASME paper*, (GT2013-94759), 2013.
- [40] J. von Wolfersdorf and B. Weigand. Internal cooling in turbomachinery. In *Turbine Blade Internal Cooling-Selected Experimental Approaches*, Lecture Series 2010-05. von Karman Institute for Fluid Dynamics, 2010.
- [41] B. Facchini, F. Maiuolo, L. Tarchi, and D. Coutandin. Combined effect of slot injection, effusion array and dilution hole on the heat transfer coefficient of a real combustor liner - part 1 experimental analysis. *ASME Turbo Expo*, (GT2010-22936), 2010.
- [42] F. Maiuolo, B. Facchini, L. Tarchi, and D. Coutandin. Experimental investigation on the effects of a large recirculating area on the performance of an effusion cooled combustor liner. *Journal of Engineering for Gas Turbines and Power*, 134:041505–1–9, 2012.
- [43] L. Bonanni. Investigation on a trailing edge cooling system. *PhD Thesis*, 2011.
- [44] G. Caciolli, A. Andreini, B. Facchini, L. Tarchi, D. Coutandin, A. Peschiulli, and S. Taddei. Density ratio effects on the cooling performances of a combustor liner cooled by a combined slot/ effusion system. *ASME Turbo Expo*, (GT2012-68263), 2012.
- [45] P. T. Ireland, Z. Wang, and T. V. Jones. Liquid crystal heat transfer measurements. In *Measurements Techniques*, Lecture Series 1993-05. von Karman Institute for Fluid Dynamics, 1993.

- 
- [46] P. T. Ireland and T. V. Jones. Liquid crystal measurements of heat transfer and surface shear stress. *Measurement Science Technology*, 11: 969–986, 2000.
- [47] P. T. Ireland, D. Gillespie, and Z. Wang. Advances in heat transfer measurements using liquid crystals. *Proc. Turbulent Heat Transfer Conf., San Diego, Eng. Foundation, New York*, 1996.
- [48] P. T. Ireland, D. Gillespie, A. J. Neely, and A. J. Robertson. Turbulent heat transfer measurements using liquid crystals. *International Journal of Heat and Fluid Flow*, 20:355–367, 1999.
- [49] F. P. Incropera, D. P. DeWitt, L. T. Bergman, and A. S. Lavine. *Fundamentals of Heat and Mass Transfer*. Wiley & Sons, 2006.
- [50] R. S. Bunker. Lattice (vortex) cooling effectiveness part 1: Stationary channel experiments. *ASME Turbo Expo*, (GT2004-54157), 2004.
- [51] B. Facchini, L. Innocenti, and L. Tarchi. Pedestal and endwall contribution in heat transfer in thin wedge shaped trailing edge. *ASME Paper*, (GT2004-53152), 2004.
- [52] B. Facchini and L. Tarchi. Investigation of innovative trailing edge cooling configurations with enlarged pedestals and square or semicircular ribs. part 1 - experimental results. *ASME Turbo Expo*, (GT2008-51047), 2008.
- [53] D. L. Schultz and T. V. Jones. Heat transfer measurements in short duration hypersonic facilities. *NATO Advisor Group Aeronautical RD AGARDograph*, (165), 1973.
- [54] D. L. Buttsworth and T. V. Jones. Radial conduction effects in transient heat transfer experiments. *Aeronautical Journal*, 101:209–212, 1997.
- [55] G. Wagner, M. Kotulla, P. Ott, B. Weigand, and J. von Wolfersdorf. The transient liquid crystal technique influence of surface curvature and finite wall thickness. *ASME J. Turbomach*, 127:176–182, 2005.

- 
- [56] D.R.H. Gillespie, P.T Ireland, and Z. Wang. "heating element". *British Patent Application PCT/GB96/2017*, 1995.
- [57] J. A. Stasiak and T.A. Kowalewski. Thermochromic liquid crystals applied for heat transfer research. *OPTO-ELECTRONICS REVIEW*, 10: 1–10, 2002.
- [58] C. Camci. Liquid crystal thermography. In *Temperature Measurements*, Lecture Series 1996-07. von Karman Institute for Fluid Dynamics, 1995.
- [59] Ian Sage. Thermochromic liquid crystals. *Liquid Crystals*, 38:1551–1561, 2011.
- [60] T. L. Chan, S. Ashforth-Frost, and K. Jambunathan. Calibrating for viewing angle effect during heat transfer measurements on a curved surface. *International Journal of Heat and Mass Transfer*, 44:2209–2223, 2001.
- [61] S. J. Kline and F. A. McClintock. Describing uncertainties in single sample experiments. *Mechanical Engineering*, 75:3–8, Jan 1953.
- [62] M. Gritsch, A. Schulz, and S. Wittig. Effect of crossflows on the discharge coefficient of film cooling holes with varying angles of inclination and orientation. *ASME J. Turbomach*, 123:781–787, 2001.
- [63] F. Maiuolo, R. Da Soghe, B. Facchini, M. Miccio, and L. Tarchi. Discharge coefficient characterization of jet array impingement holes for an active clearance control system. *9th European Turbomachinery Conference*, (ETC252-2011), 2011.
- [64] P. Brevet, C. Dejeu, E. Dorignac, M. Jolly, and J.J. Vullierme. Heat transfer to a row of impinging jets in consideration of optimization. *International Journal of Heat and Mass Transfer*, 45:4191 – 4200, 2002.
- [65] Z. Liu and Z. Feng. Numerical simulation on the effect of jet nozzle position on impingement cooling of gas turbine blade leading edge. *International Journal of Heat and Mass Transfer*, 54:4949–4959, 2011.

- [66] L. Andrei, A. Andreini, R. Da Soghe, B. Facchini, and S. Zecchi. Numerical analysis of heat transfer in a leading edge geometry with racetrack holes and film cooling extraction. *ASME Turbo Expo*, (GT2013-94673), 2013.